Effect of Nappe Non-aeration on Caisson Sliding Force During Tsunami Breakwater Overtopping

Sanduni Disanayaka Mudiyanselage

Technische Universiteit Delft

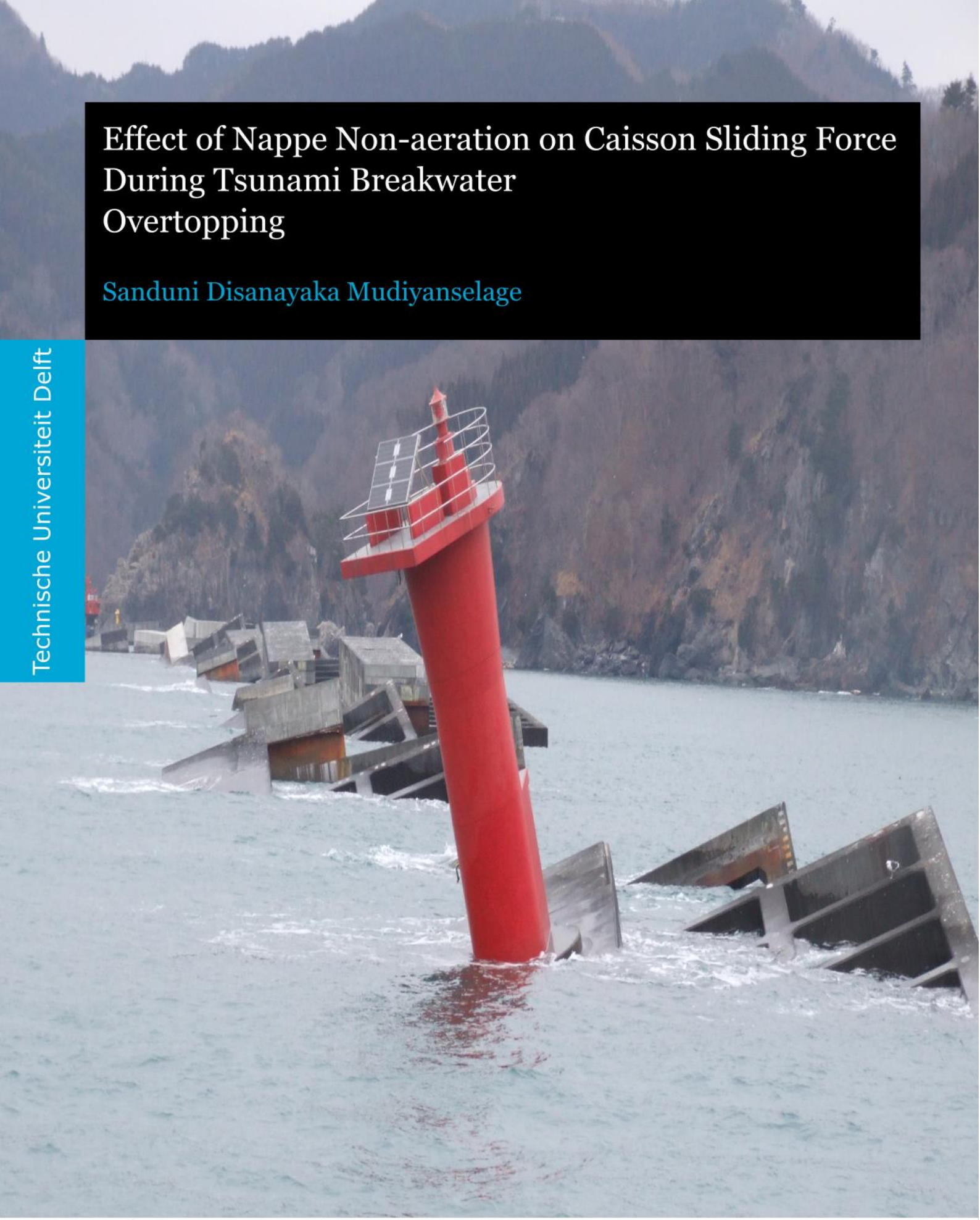

TU Delft

Challenge the future

ERASMUS +: ERASMUS MUNDUS MOBILITY PROGRAMME

Master of Science in

COASTAL AND MARINE ENGINEERING AND MANAGEMENT

CoMEM

EFFECT OF NAPPE NON-AERATION ON CAISSON SLIDING FORCE DURING TSUNAMI BREAKWATER OVERTOPPING

Delft University of Technology

11th July 2017

Sanduni Disanayaka Mudiyanselage

The Erasmus+: Erasmus Mundus MSc in Coastal and Marine Engineering and Management is an integrated programme including mobility organized by five European partner institutions, coordinated by Norwegian University of Science and Technology (NTNU).

The joint study programme of 120 ECTS credits (two years full-time) has been obtained at two or three of the five CoMEM partner institutions:

- Norges Teknisk- Naturvitenskapelige Universitet (NTNU) Trondheim, Norway
- Technische Universiteit (TU) Delft, The Netherlands
- Universitat Politècnica de Catalunya (UPC). BarcelonaTech. Barcelona, Spain
- University of Southampton, Southampton, Great Britain
- City, University London, London, Great Britain

During the first three semesters of the programme, students study at two or three different universities depending on their track of study. In the fourth and final semester an MSc project and thesis has to be completed. The two-year CoMEM programme leads to a multiple set of officially recognized MSc diploma certificates. These will be issued by the universities that have been attended by the student. The transcripts issued with the MSc Diploma Certificate of each university include grades/marks and credits for each subject.

Information regarding the CoMEM programme can be obtained from the programme coordinator:

Øivind A. Arntsen, Dr.ing.
Associate professor in Marine Civil Engineering
Department of Civil and Transport Engineering
NTNU Norway
Telephone: +4773594625 Cell: +4792650455 Fax: + 4773597021
Email: oivind.arntsen@ntnu.no

CoMEM URL: https://www.ntnu.edu/studies/mscomem

CoMEM Master Thesis

This thesis was completed by:

Sanduni Disanayaka Mudiyanselage

Under supervision of:

Prof.dr.ir. W.S.J. Uijttewaal
Associate Prof.dr.ir. J.D. Bricker
Assistant Prof.dr.ir. G.H. Keetels

As a requirement to attend the degree of
Erasmus+: Erasmus Mundus Master in Coastal and Marine Engineering and Management (CoMEM)

Taught at the following educational institutions:

Norges Teknisk- Naturvitenskapelige Universitet (NTNU)
Trondheim, Norway

Technische Universiteit (TU) Delft
Delft, The Netherlands

University of Southampton,
Southampton, Great Britain

At which the student has studied from August 2015 to July 2017.

Effect of Nappe Non-aeration on Caisson Sliding Force during Tsunami Breakwater Overtopping

By

Sanduni Disanayaka Mudiyanselage

Correspondence with the author may be directed to:
sanduni_30@hotmail.com

“විද්‍යාව ආලෝකයයි”

“Wisdom Enlightens”

Summary

The sliding force was a contributing factor to the displacement of caissons from the Kamaishi composite breakwater during the Great East Japan tsunami 2011 (Arikawa et al., 2012). The pressure reduction on the landward wall of the caisson due to non-aeration of the overflowing jet gives rise to an additional horizontal force which increases the sliding force. The estimation of this additional horizontal force and the proper understanding of the physical processes which cause it are imperative in establishing stability of a caisson breakwater during tsunami overtopping.

Tsunami is associated with accelerating flows with massive heads that results in detached overflow nappes. In this research, a simplified tsunami was modelled in the laboratory as a steady breakwater overflow and the respective pressure drop behind the overflow nappe is derived. The nappe trajectories are derived theoretically based on general projectile motion for both the aerated and non-aerated scenarios. This ballistic model is validated using measurements of the physical model. For the aerated nappe, the theoretical results and measurements are in agreement. For the non-aerated nappe, the ballistic model provides comparatively high deviations from the measured nappe. A sensitivity analysis of pressure reduction indicates the deviations can be attributed to the derived pressure drops.

In addition, the governing physical processes related to caisson breakwater overflowing are investigated. The flow conditions below the overflow nappe are hydrostatic, which is implied by a time-averaged stationary water level below the nappe. The dynamic pressure arising from the stagnation pressure at the jet impingement on the flume bed is estimated and is compared with the pressure drop behind the nappe. The results suggest the above-mentioned dynamic pressure is negligible with respect to the pressure drop. Thus, it is concluded that the governing mechanism responsible for the pressure reduction is the air entrainment process during jet impingement. The air entrainment rate from the cavity behind the nappe is compared against the impinging velocity of the overflow jet. The results suggest that air entrainment rate increases with increasing jet impingement velocity, establishing the fact that higher inertia forces leads to rapid air entrainment.

The ratio of additional horizontal force due to non-aeration to the total horizontal force is found to be between 0.15 and 0.3. However, some eccentricities are evident with extreme tail water depths and flow rates. Scaled-up forces are obtained using Froude scaling criteria. Reynolds numbers suggest that the flow is fully turbulent at both the lab and field scales, while Weber numbers show that surface tension effects might be more pronounced in the lab than in the field.

As surface tension effects may affect the direct scaling up of model tests to field scale, the utility of numerical model simulations is apparent. In OpenFOAM, the k-epsilon turbulence model with the InterFoam solver is used for this purpose. Prior to investigating the validity of OpenFOAM to simulate the caisson overflowing scenario,

the model is validated for open channel flow. The results indicate that OpenFOAM correctly simulates the open channel flow with respect to the logarithmic profile and the free-surface slope. Furthermore, simulation of the flow atop the caisson very closely matches that of the physical laboratory model test. The model results for nappe behaviour follows existing trends found in literature. The simulated overflow nappe is a clinging nappe rather than a detached one due to the inability of the 2D model to allow air into the void behind the nappe.

The significance of the present study has various aspects. The ballistic model enables the derivation of the nappe's trajectories during steady overflow of a caisson breakwater. As a result, an explicit relationship between kinematics (ballistics) and dynamics (forces) can be developed. The estimation of the additional horizontal force due to non-aeration effects pave the way to improve design guidelines for the stability of caisson breakwaters during tsunami overtopping.

Table of Contents

Summary i
List of Figures v
List of Tables vii
Acknowledgment viii
Nomenclature ix
1 Introduction 1
1.1 Background 1
1.2 Problem statement and motivation 3
1.3 Research goal 6
1.4 Research questions 6
1.5 Report Outline 7
2 Literature review 8
2.1 Additional horizontal force due to nappe non-aeration 9
2.1.1 Derivation of nappe trajectories using a ballistic model 10
2.1.2 Hydrostatic forces from theory 15
2.1.3 Determination of additional horizontal force (ΔF) 17
2.1.4 Air entrainment and jet impingement 19
2.2 CFD simulation using OpenFOAM 19
3 Governing physical processes during caisson overtopping 21
3.1 Physical model 22
3.1.1 Objective 22
3.1.2 Selection of the geometric scale 22
3.1.3 Experimental procedure 24
3.1.4 Determination of the flow rate 26
3.1.5 Behaviour of caisson as a broad-crested weir 27
3.1.6 Measurement of pressure during the laboratory experiment 28
3.2 Behaviour of overflow nappe 31
3.2.1 Validation of the ballistic model against the physical model results 32
3.3 Recirculation and air entrainment 35
3.3.1 Flow separation and recirculation 35
3.3.2 Air entrainment during the caisson overflowing 38

4 Determination of relevant forces and scaling up 41
4.1 Determination of additional horizontal force (ΔF) 42
4.2 Application of physical model results to the field scale 44
4.2.1 Direct scaling up 44
4.2.2 Limitations related to scaling up 44
5 CFD modelling using OpenFOAM 46
5.1 Validation of InterFoam model for open channel flow 47
5.1.1 Checking for logarithmic profile 47
5.1.2 Determination of free surface slope 49
5.2 Simulation of caisson overflowing experiment using OpenFOAM 51
5.2.1 Model set-up 51
5.2.2 Description of the model runs 53
5.2.3 Results and analysis 53
6 Conclusions 57
7 Recommendations 61
References 62
APPENDIX 64
A Dimensions of caisson used in the physical model 64
B Determination of parameters related to scaling 65
C Calculation of flow rates 65
D Influence of 'Coanda' effect 66
E Description of the pressure sensors used 67
F Calibration of pressure sensors 69
G Non-hydrostatic calculation of ΔP 72
H Determination of the air entrainment rate 74
I Input structure of InterFoam 75
I.1 Constant directory 75
I.2 System directory 76
I.3 'Time' directories 76
J Analysis of pressure results and calculation for $\rho_{effective}$ 77

List of Figures

Figure 1.1 : Kamaishi breakwater 1
Figure 1.2 : Caisson displacement of Kamaishi breakwater 2
Figure1.3: Comparison of horizontal force(drag) 3
Figure 1.4 : Pressure differences associated with the caisson breakwater overflow 5
Figure 2.1 : Types of nappe (Abdalla & Shamaa, 2016) 9
Figure 2.2 : Derivation of aerated nappe profile using the principle of projectile 10
Figure 2.3 : Deviation of non-aerated nappe's trajectory due to pressure gradient 12
Figure 2.4 : Nappe parameters during a non-aerated nappe 12
Figure 2.5 : Nappe trajectory comparison 14
Figure 2.6 : Flow parameters during overflowing of a caisson with an aerated nappe 14
Figure 2.7 Parameters affecting hydrostatic horizontal force 15
Figure 2.8 Parameters used to determine the lift force and the overturning moment. 16
Figure 2.9 Variation of pressure during aerated nappe scenario 17
Figure 2.10 Variation of pressure during non-aerated nappe scenario 18
Figure 3.1 : Dimensions of Kamaishi breakwater 23
Figure 3.2 : Schematic diagram of the flume including the boundaries 25
Figure 3.3 : Schematic diagram of the laboratory experiment 25
Figure 3.4 Experimental conditions with time 25
Figure 3.5 : Transition of flow regime from sub-critical to super-critical 27
Figure 3.6 Positioning of three pressure sensors 28
Figure 3.7 : Pressure sensors used in the experimental set-up 28
Figure 3.8 Pressure variation along the vertical surface of the caisson 29
Figure 3.9 : Pressure sensor readings during aerated and non-aerated conditions 30
Figure 3.10 : Comparison of overflow nappe trajectory and the water level 31
Figure 3.11 : Nappe behaviour with increasing time 31
Figure 3.12 : Derived trajectory of the nappe 33
Figure 3.13 : Derived trajectory of the nappe using a 33% reduced ΔP value 34
Figure 3.14 : Flow separation due to widening and deepening of flow 35
Figure 3.15 Detailed flow features of the backward facing step flow 35
Figure 3.16 : Conditions governing the recirculation under the nappe 36
Figure 3.17 : Recirculation driven by the adverse pressure gradient 36
Figure 3.18 : Air entrainment process from the overflow jet impinging 38

Figure 3.19 : Mechanisms that give implications on the air entrainment process..... 39
Figure 3.20 : Pressure time series of the bottom pressure sensor..... 40
Figure 4.1: Additional horizontal force variation with pressure drop..... 43
Figure 5.1 : Model domain for open channel flow..... 47
Figure 5.2 : Vertical profiles of horizontal velocities..... 48
Figure 5.3 : Model domain used in OpenFOAM simulation of the physical model..... 53
Figure 5.4 : Visual comparison of the free-surface over the caisson..... 54
Figure 5.5 : Area behind the nappe which is always filled with air during the laboratory experiment..... 55
Figure 5.6: OpenFOAM simulation nappe behavior..... 55
Figure 6.1 : Additional horizontal force (ΔF) variation with pressure drop (ΔP)..... 59
Figure E.1 : Differential pressure sensor..... 68
Figure E.2 : Underlying principle of the pressure sensor based on resistivity..... 68
Figure F.1 : Schematic diagram of the calibration set-up of the pressure sensor..... 69
Figure H.1 : Pressure time series of the bottom pressure sensor..... 74

List of Tables

Table 3.1 Comparison of parameters for Kamaishi overtopping and physical model... 23
Table 3.2 : Measurements of the experimental runs performed 26
Table 3.3: Parameters affecting the dynamic pressure gradient and wall friction 38
Table 3.4 : Comparison of air entrainment rate and the jet impinging velocity..... 40
Table 4.1 Additional horizontal forces (ΔF) in the physical model 42
Table 4.2: Scaled-up parameters for field scale 44
Table 4.3 : Comparison of Weber number for the physical model of Test 45
Table 5.1 : Results of roughness lengths and viscous sub-layer thicknesses 49
Table 5.2 : Comparison of analytical and model results for free-surface slope..... 51
Table 5.3: Comparison of experiment results 54
Table A.1 : Dimensions associated with the laboratory experiment 64

Acknowledgment

The present report is the result of my final thesis for Erasmus masters program of Coastal and Marine Engineering and Management (CoMEM). I am forever grateful for the opportunity I got through the CoMEM program to study in three leading universities in the world which undoubtedly helped me to acquire plethora of knowledge in the field of Coastal Engineering. Therefore, I thank the EU and the CoMEM board for giving me this wonderful opportunity.

This thesis would not be successful without the continuous support of my supervisory committee. I would like to thank Wim Uijttewaal for chairing my committee and always encouraging me to broaden my perspective on the thesis topic. Your valuable comments during the progress meetings helped me to shape my thesis in an effective manner. Also thank you Wim for sparing your time to share your expertise. I am highly grateful to my daily supervisor, Jeremy Bricker for giving me the opportunity to take part in this research and for your continuous guidance throughout. Thank you Jeremy, for all your kind assistance and I learnt a lot from the discussions we had every other week. Thanks for all your time, patience and most of all for keeping the positive mind set which kept me going. Further, I thank Geert Keetels for being part of my supervisory committee and for your valuable inputs on various aspects of my thesis.

I would like to thank my better half, Hithaishi without whom I would not be where I am today. Thank you for your unconditional love during these two amazing years and you have always been my pillar of strength. We believe that both of us are so lucky to have spent two most fruitful and memorable years together as CoMEM students for which we are forever grateful to the EU.

I also would like to thank my dear parents, my sister and brother for loving me so much. Your constant support has been my strength during this time period and thank you so very much. Finally, I am thankful to all my CoMEM friends for all the fond memories and friendships that I will adore for the years to come.

Sanduni Jayawardana

Delft, July 2017

Nomenclature

Symbol	Units	Description
a	m/s^2	Acceleration (in addition to gravity) on a water particle in nappe
B_C	m	Width of the caisson(=0.195m)
C_f	-	Wall skin friction coefficient
d	m	Total flow depth below the nappe
d_{b}	m	Flow depth at the brink of caisson top
d_{c}	m	Critical flow depth at the top of the caisson
d_{hw}	m	Flow depth at upstream of the caisson
d_{lw}	m	Flow depth at downstream of the caisson
d_{nappe}	m	Thickness of the overflow nappe
d_{o}	m	Overflow depth
d_{vertical}	m	Vertical thickness of the nappe
d'	m	Additional water depth behind the nappe w.r.t. tail water depth
F_{hydro}	N	Hydrostatic horizontal force
F_{tot}	N	Total horizontal force
g	m/s^2	Gravitational acceleration
h	m	Water depth
H	m	Total head at upstream
H_{C}	m	Height of the caisson
L_{C}	m	Length of the caisson (=0.153m)
L_{d}	m	Length of the drop measured from caisson vertical surface
P	Pa	Pressure
P_{atm}	Pa	Atmospheric pressure
$P_{\mathrm{sub-atm}}$	Pa	Sub-atmospheric pressure
Q	m^3/s	Steady flow rate
t	s	Time
u	m/s	Horizontal velocity of a water particle
U	m/s	Flow speed
U_*	m/s	Shear velocity
V	V	Voltage
v	m/s	Vertical velocity of a water particle
V_{bot}	m/s	Jet impinging velocity at the bottom
V_{imp}	m/s	Jet impinging velocity into the pool of water
w'	m	Height of the downstream weir
z	mm	Vertical distance
z_0	mm	Roughness length
α	-	Air-water phase fraction

δ	mm	Viscous sub-layer thickness
η	m	Water surface elevation
η_0	Ns/m^2	Dynamic viscosity
θ	^{0}	Angle of nappe with the horizontal
ϑ	m^2/s	Kinematic viscosity
κ	-	Kappa constant
λ	-	Constant depending on the overflow conditions
ν	m^2/s	Kinematic viscosity of water
ρ	kg/m^3	Density of water
ρ_{eff}	kg/m^3	Effective density of water with the air bubbles
σ	mN/m	Surface tension of water
τ_{b}	Pa	Bed shear stress
τ_{wall}	Pa	Friction of the flume bed wall or caisson wall
Δd	m	Water level difference between the upstream and downstream
ΔF	N	Additional horizontal force due to the pressure drop behind nappe
ΔP	Pa	Nappe sub-pressure
ΔP_{dyn}	Pa	Dynamic pressure gradient

1 Introduction

1.1 Background

The Great East Japan tsunami disaster (2011) is one of the most devastating natural disasters in Japanese history in recent times. Being a well-prepared country to encounter tsunamis, the catastrophic extent of the damage that Japan underwent due to this tsunami is still of great magnitude. This encourages the need for more research and studies into the various aspects that would directly and indirectly lead to the establishment of more robust and reliable mitigation schemes.

In this scenario, this study focuses on one of the offshore breakwaters that has been built in Kamaishi Bay, Iwate Prefecture, Japan and has partially failed in 2011. The Kamaishi breakwater located in Sanriku ria coast, is the deepest and largest breakwater in the world (Tanimoto & Takahashi, 1994). It is comprised of a pair of breakwaters of lengths 990m and 670m which are linked by a 300m submerged opening of 63m depth (20m of water depth on top of 43m rubble mound and caissons) as shown in Figure 1.1(Tanimoto & Takahashi, 1994). As the threat of a tsunami is ever present in Japan, the purpose of this offshore breakwater was to mitigate the impacts of a tsunami event(Bricker, 2013). In fact, many studies suggest that the Kamaishi breakwater has contributed significantly into the attenuation of tsunami wave height into the bay during the 2011 Japan tsunami (Pringle et al., (2011) ; Tomita et al., (2012)).

Figure 1.1 : Kamaishi breakwater which consists of two separate breakwaters of lengths 990m and 670m (Suppasri et al., 2013)

The Kamaishi breakwater had been overtopped during the Great East Japan tsunami 2011. Due to the tsunami, many caissons were displaced from the rubble mound towards the landward direction and the caissons that were still left on the rubble mound were not vertical anymore (Arikawa et al., 2012). This is depicted in Figure 1.2. This observation indicates that the partial failure of the caisson breakwater is due to the incident tsunami wave.

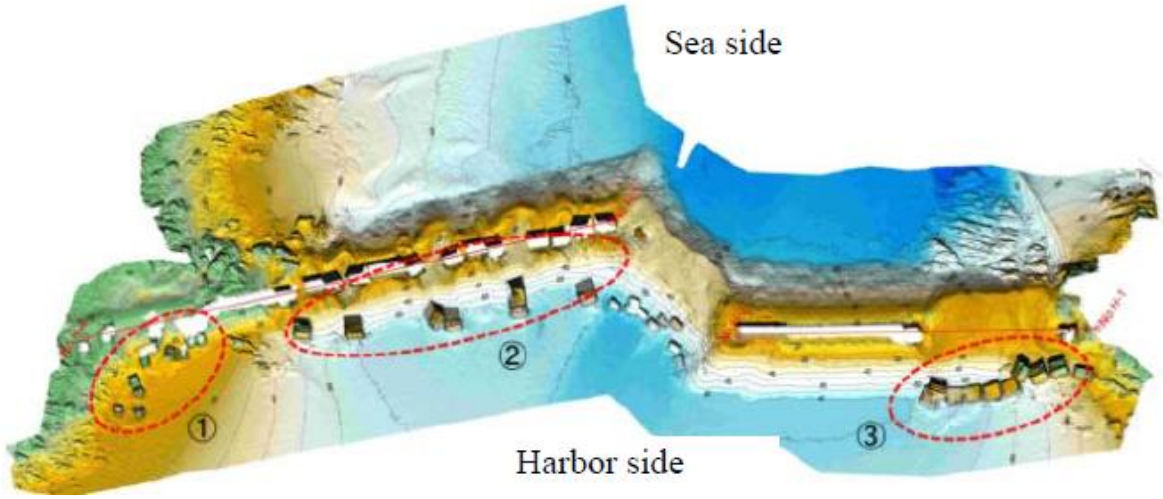

Figure 1.2 : Caisson displacement of Kamaishi breakwater towards harbour side during Japan tsunami 2011(Multibeam SONAR Tomita et al , 2012)

During the tsunami overtopping, the behaviour of the overtopping jet provides important implications on the possible failure modes of the caisson breakwater. For instance, the strong pulling of the overflow jet away from the harbour end of the caisson makes the air to be entrained from the cavity bounded by the jet and the caisson wall. This leads to a non-aerated nappe where the lost air is not replaced from outside. Consequently, the non-aeration of the overflow jet leads to a substantial reduction in pressure within cavity. This might have acted as a contributing factor for the sliding of the caissons and ultimately caused the displacement of them as illustrated in Figure 1.2.

1.2 Problem statement and motivation

During the Great East Japan tsunami (2011), the partial failure of the Kamaishi breakwater can be attributed to several direct and indirect reasons. The sliding force was found to be a contributing factor to the displacement of caissons from the Kamaishi composite breakwater during the Great East Japan tsunami 2011 (Arikawa et al., 2012). The sliding force is the net horizontal force between the destabilizing forces and stabilizing forces. The stabilizing forces (friction between caisson and rubble mound underneath) are not affected by the non-aeration of the overflow nappe.

One important force that has contributed to the failure of Kamaishi breakwater is the horizontal force (destabilizing) acted on the caisson. Comparison of the several OpenFOAM simulation results with the hydrostatic calculations are depicted in Figure 1.3. (Bricker, 2013). The hydrostatic horizontal force is calculated based on the differential static water levels across the caisson.

The total horizontal force is the sum of a hydrostatic component and an additional horizontal force component.

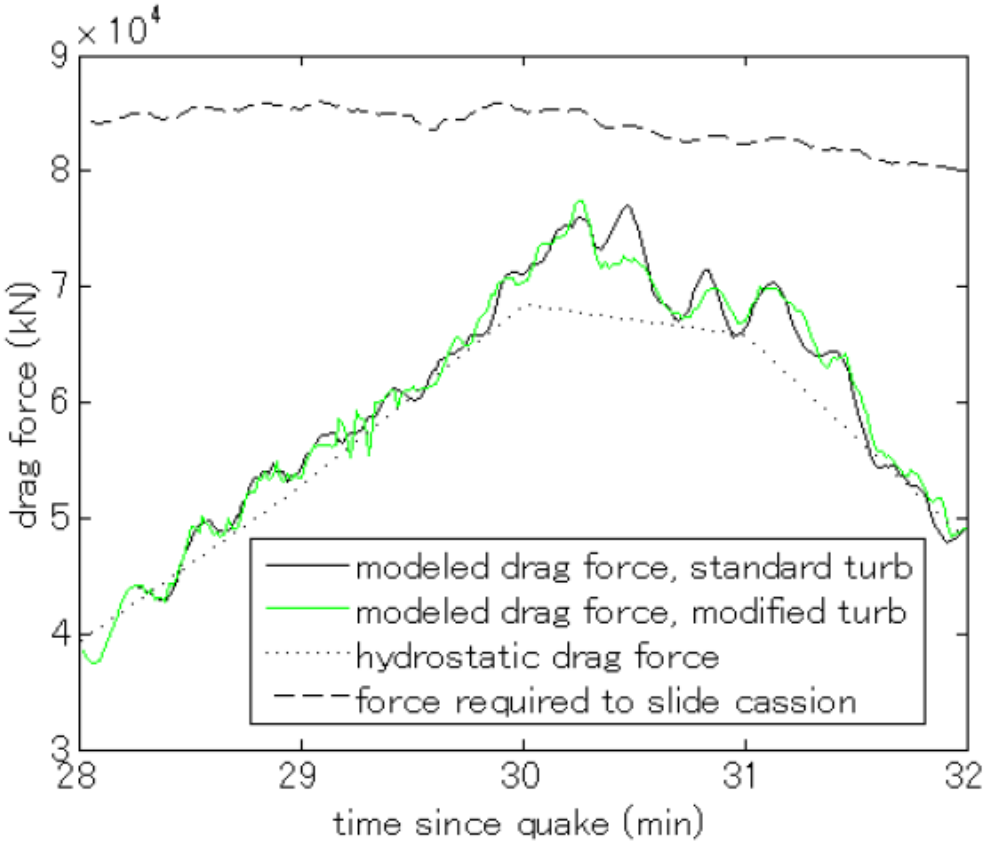

Figure 1.3 : Comparison of horizontal force(drag) during Kamaishi breakwater overtopping (Bricker, 2013)

In Figure 1.3, the solid lines represent the total horizontal force on the caisson during overtopping, which were modelled in OpenFOAM. The dotted black line represents the hydrostatic force.

From Figure 1.3, it can be observed that there is a significant difference between the total horizontal force and the hydrostatic components.

The difference between the above-mentioned forces is due to the additional horizontal force by the induced suction from the non-aeration of the overflow nappe. In a tsunami, the development of suction pressure and non-aeration of overtopping jet occurs as a result of the nappe's transition from a 'clinging' nappe to a 'drowned' nappe as the surcharge and the tail water depth increases with time. These terms ('clinging' and 'drowned' nappes) will be explained later in Chapter 2.

The difference between the total horizontal (F_{tot}) force and the hydrostatic component (F_{hydro}) relative to the latter force can be found from equation 1.1.

$$Relative\ Difference = \frac{F_{tot} - F_{hydro}}{F_{hydro}} \tag{1.1}$$

The hydrostatic horizontal force is the force applied based on the water level difference on either side of the caisson breakwater. The maximum relative difference is found to be 19.1% based on Figure 1.3. Therefore, it can be seen that the difference between the actually applied total horizontal force and the hydrostatic horizontal force is of significant order of magnitude. Hence, it is imperative to investigate and estimate the influence of the additional horizontal force.

It can be hypothized that the additional horizontal force is a result of the pressure drop behind the overflow nappe. The pressure drop occurs due to the air entrainment of the overflow nappe. However, due to the dynamic nature of a breakwater overtopping scenario, the estimation of this additional horizontal force is not straightforward. Hence, the estimation of the influence of suction pressure behind nappe can be performed by studying the deviation of the nappe trajectory. This deviation can then be related to the extra force component on the caisson breakwater. This can be further explained using Figure 1.4 below.

For a composite breakwater, mainly the caisson is affected by the additional horizontal force generated by overflowing. Thus, the extra force component is investigated in relation to its impact on the caisson as shown in Figure 1.4.

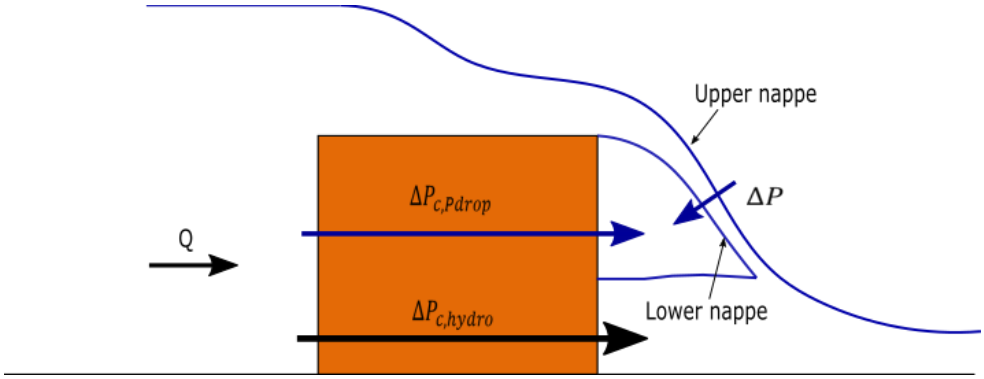

Figure 1.4 : Pressure differences associated with the caisson breakwater overflow scenario ($\Delta P_{C,Pdrop}$ and ΔP occur as a result of non-aeration of the nappe. $\Delta P_{C,hydro}$ occurs as a result of the water level difference across the caisson)

Where,

$\Delta P_{C,hydro}$: Pressure difference across the caisson due to the differential water levels on either side of the caisson

$\Delta P_{C,Pdrop}$: Pressure difference across the caisson due to the non-aeration of the nappe ($<\Delta P_{C,hydro}$)

ΔP : Pressure difference across the nappe due to the non-aeration of the nappe

The upper nappe is at the atmospheric pressure while the lower nappe is at a sub-atmospheric pressure. This difference leads to ΔP. Due to the effect of ΔP on the nappe, the trajectory of the nappe deviates towards the caisson. This deviation of nappe trajectory can be estimated theoretically. As the pressure at upstream end of the caisson is greater than the atmospheric pressure, $\Delta P_{C,Pdrop}$ is much larger than ΔP. Thus, it can be inferred that the additional horizontal force acting on the caisson is of higher degree of magnitude than that on the nappe's trajectory. Likewise, the deviation of nappe's trajectory can be linked to the additional horizontal force exerted on the caisson.

The additional horizontal force (ΔF) is a destabilizing force which increases the sliding force acting on a caisson breakwater during tsunami overtopping. As a result, the stability of the caisson breakwater is adversely affected.

1.3 Research goal

The research goal of the present thesis consists of a primary goal and two secondary goals.

The primary objective is to establish how the stability of a caisson breakwater during a tsunami overtopping is set up, specifically concentrating on the sliding force exerted on the caisson. This includes the determination of the additional horizontal force component generated due to the non-aeration behind the nappe. In this context, the determination of the additional horizontal force is done by linking it to the overflow nappe's trajectory.

As one of the secondary objectives, this thesis aims to improve the understanding on the governing physical processes during a caisson overflowing including the air entrainment and the pressure drop behind the overflow nappe as they play vital roles in the establishment of the additional horizontal force.

The other secondary objective is to evaluate the validity of a commonly-used RANS model (OpenFOAM) for a tsunami breakwater overflow scenario.

1.4 Research questions

In order to achieve the research goals, research questions to be answered can be formulated under the following aspects.

A. What is the relative magnitude of the additional horizontal force (ΔF) when compared to the total horizontal force? Is the magnitude significant enough to impose considerable impact on the stability of the breakwater?

B. What is the extent of applicability of the small-scale physical model results (eg : forces, flow characteristics) to the reality?

C. What is the validity of the ballistic model (theoretical) in deriving the overflow nappe's trajectory for aerated and non-aerated cases? What conclusive remarks can be made on the physical processes involved?

D. How to estimate the additional horizontal force on the caisson breakwater when the nappe's trajectory is established during a tsunami?

E. What conclusions can be drawn regarding simulation of the physical model results of a breakwater overtopping using OpenFOAM including all the physical processes involved?

F. What is the role of the nappe's behaviour during a tsunami overtopping? What are the relevant factors that need to be considered when comparing it with the nappe behaviour of the physical model?

1.5 Report Outline

The report outline is formulated under seven chapters.

I. **Literature review (Chapter 2)**
In this chapter, mainly the nappe characteristics including the governing physical processes during a caisson overflowing are investigated. The theory is developed in a comprehensive manner starting from nappe trajectory to the determination of the additional horizontal force. Further, the relevant literature related to OpenFOAM simulation of the Kamaishi breakwater overtopping are discussed.

II. **Governing physical processes during caisson overflowing (Chapter 3)**
The physical model of steady overflowing of a caisson breakwater is discussed. The ballistic model used to derive the nappe trajectories is validated using the measured coordinates of the nappe's trajectory. In addition, analytical solutions are developed on the mechanisms such as pressure drop, air entrainment effects, recirculation and water level increase below the nappe.

III. **Determination of relevant forces and scaling up (Chapter 4)**
The magnitude of the relevant forces are estimated. The applicability of physical model results in the field scale is analysed. Further, the effect of other external parameters on the additional horizontal force are also analysed.

IV. **CFD modelling with OpenFOAM (Chapter 5)**
(a)Validation of CFD model: Prior to investigating the validity of OpenFOAM in comparison to the physical model, as an initial step, the CFD model is validated using an open channel flow under two different criteria (Section 5.1).

(b)Simulation of the physical model results: The physical model is simulated using InterFoam k-epsilon model to evaluate whether it correctly captures the non-aeration effects and air-water interface formation during a caisson breakwater overflowing. (Section 5.2).

V. **Conclusions and recommendations (Chapter 6 & 7)**
The conclusions drawn are summarized. Based on the work done, the recommended research areas for future work are discussed.

2 Literature review

The present chapter is divided into two sections and each of the section presents relevant literature to contextualize the thesis work. The first section (2.1) gives an overview on the theoretical basis on the determination of the additional horizontal force due to non-aeration during a caisson overflowing scenario. An inclusive theoretical formulation on the overflow nappe characteristics, nappe trajectory derivation, pressure drop behind the nappe and the determination of the additional horizontal force is presented in this section. The second section (2.2) presents the relevant literature related to the OpenFOAM simulations of breakwater overtopping nappe. It includes the challenges encountered in simulating the air-water interface of the nappe in OpenFOAM.

2.1 Additional horizontal force due to nappe non-aeration

The sliding force acting on the breakwater due to the overflow nappe behaviour invites more research into numerous aspects related to the nappe flow profile. These aspects include the pressure reduction below the nappe, nappe trajectory deviation due to nappe sub-pressure, aeration and non-aeration effects. A number of past research studies in relation to falling jets over broad-crested weirs can be associated for this purpose.

These studies can be sub-categorised into two segments, namely a fully aerated jet and a non-aerated jet. In general, the free fall over broad-crested weirs are restricted to cases where both the lower nappe surface and upper nappe surface are subjected to atmospheric pressure (equivalent to aerated nappe situation).

Abdalla & Shamaa (2016) classifies the nappe types into four different categories based on ventilation into the space below the nappe as depicted in Figure 2.1.

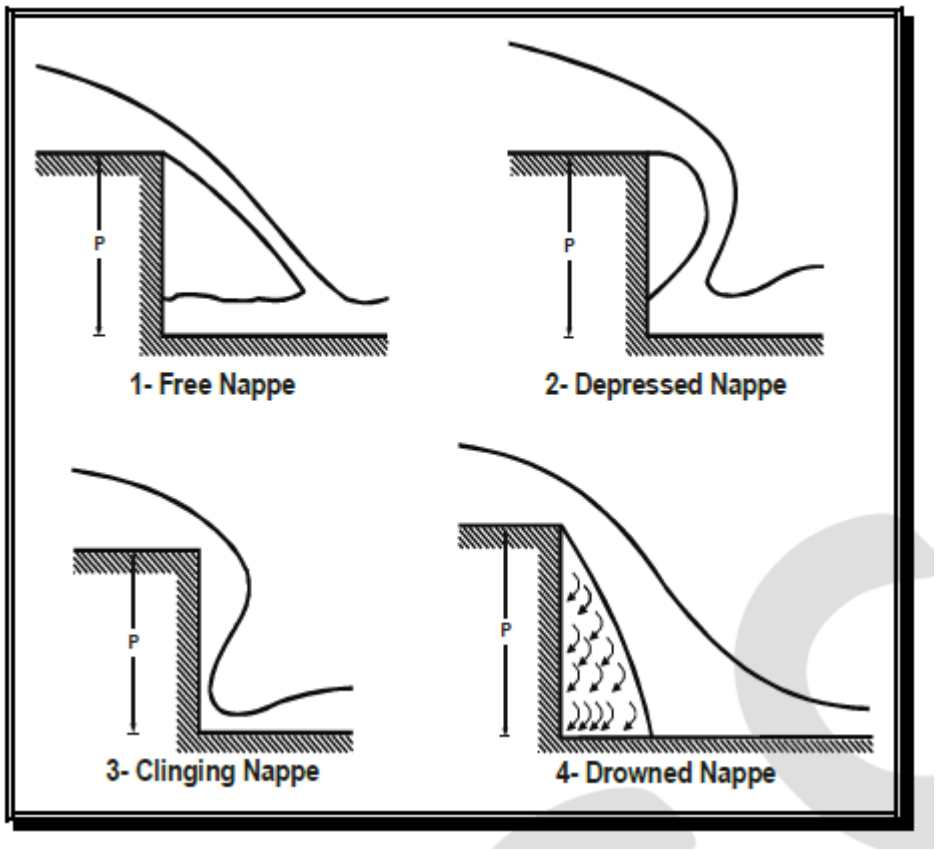

Figure 2.1 : Types of nappe (Abdalla & Shamaa, 2016)

According to Abdalla & Shamaa (2016), each type of nappe can be described as shown below:

Free nappe: Full ventilation is present below the nappe which leads to the situation where both the lower and upper nappe are in atmospheric pressure. This can be introduced as 'aerated nappe' situation.

Depressed nappe: Only partial ventilation is possible during this case. A sub-atmospheric pressure is developed below the nappe which attempts to drag the lower part of the nappe towards the step.

Clinging nappe: This type of nappe occurs when there is no air left below the water. This can be due to the high entrainment of air by the nappe itself. The final result is that the nappe clings to the wall of the step as shown in Figure 2.1.

Drowned nappe: This type of nappe can be observed when there is very high heads with no ventilation. As it can be seen from Figure 2.1, the full space below the lower nappe surface is filled with eddying mass of water.

With regards to the Kamaishi breakwater overtopping scenario, the 'pulling away' from the caisson could be due to the transition of nappe from 'clinging nappe' to 'drowned nappe'.

In the present thesis, the attention is mainly focussed on the free nappe (aerated) and depressed nappe (non-aerated). The suction on the caisson due to non-aeration of the nappe will be treated as an indicator of the additional horizontal force component acting on a caisson breakwater during an overtopping scenario.

2.1.1 Derivation of nappe trajectories using a ballistic model

Based on the theory of projectile motion the nappe trajectories are developed in this section taking the pressure difference across the overflow nappe into account.

2.1.1.1 Trajectory of aerated nappe

The overflowing nappe is considered aerated, when both the upper and lower nappe surfaces are subjected to the atmospheric pressure.

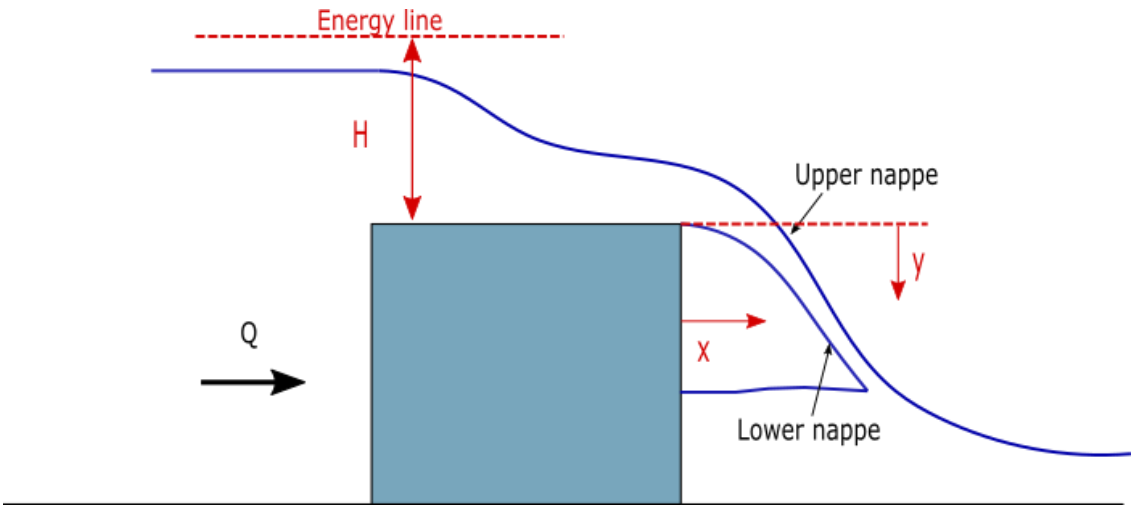

Figure 2.2 : Derivation of aerated nappe profile using the principle of projectile (x and y are measured from the vertical and horizontal planes indicated. H is the total head above the crest)

For the derivation of the nappe (aerated) equations, the following assumptions are used.

- The only force acting on the nappe is gravity.
- The horizontal velocity component of the flow is constant till the point where the nappe impinges into the pool of water.

Firstly, consider a water particle of water in the lower surface of the nappe. (Both x and y distances are measured as depicted in Figure 2.2.

For the motion in horizontal direction (during time t),

$$x = ut \tag{2.1}$$

For the motion in vertical direction (during time t),

$$y = -vt + \frac{1}{2} g\, t^2 \tag{2.2}$$

As the vertical velocity at the brink of caisson(v) is zero, equation (2.2) becomes,

$$y = \frac{1}{2} g\, t^2 \tag{2.3}$$

By removing t and dividing by total head above crest (H) gives,

$$\frac{y}{H} = A(\frac{x}{H})^2 \tag{2.4}$$

In equation 2.4, $A = gH/2u$. Since the horizontal component is constant, the vertical thickness of the nappe ($d_{vertical}$) can be assumed constant (Chow, 1959). By adding a term $d_{vertical}/H$ to equation (2.4) above, the general equation for the upper nappe envelope is given by,

$$\frac{y}{H} = A(\frac{x}{H})^2 + \frac{d_{vertical}}{H} \tag{2.5}$$

The equations derived for lower nappe envelope and upper nappe envelope (equations 2.4 and 2.5) are quadratic, hence it can be established that the nappe surfaces are theoretically parabolic.

2.1.1.2 Trajectory of non-aerated nappe

During a tsunami overtopping of a caisson breakwater, an insufficient aeration below the nappe is anticipated. This non-aeration of the overflowing nappes are evident in cases of overflowing spillways and measuring weirs(Chow, 1959). According to Chow, (1959), this results in many undesirable effects such as (I) increase in pressure difference on the spillway and (II) change in the shape of the nappe.

The deviation of nappe's trajectory occurs due to the suction induced by the sub-atmospheric pressure behind the nappe as depicted in Figure 2.3.

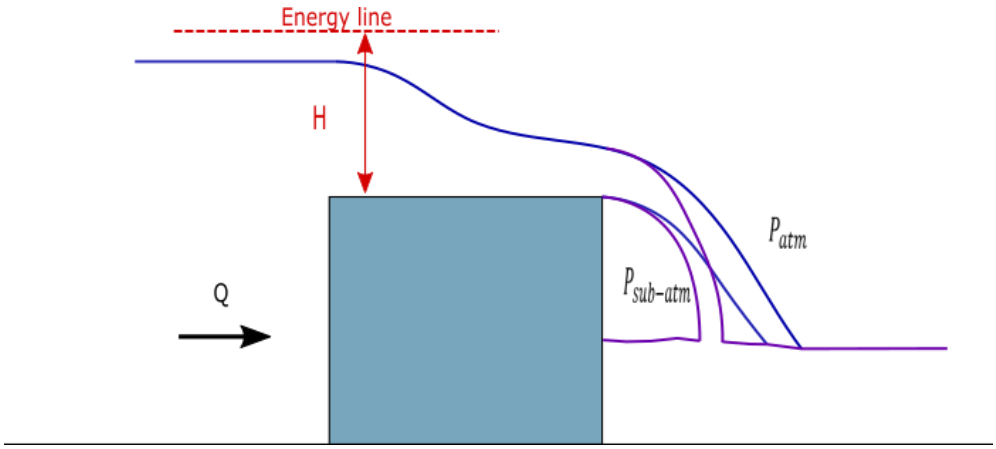

Figure 2.3 : Deviation of non-aerated nappe's trajectory due to pressure gradient (The blue nappe is the aerated nappe whereas the purple nappe is the non-aerated nappe)

This deviation is a result of the pressure difference across the nappe (ΔP). Unlike in the aerated nappe case (where only gravity is applied), an additional acceleration (a) due to ΔP is applied on the nappe.

The additional acceleration acts perpendicular to the mid path of nappe trajectory as shown in Figure 2.4 below. Due to the insignificant difference in curvature, it can be assumed that a is acting perpendicular to the lower nappe envelope. For simplicity purposes, a water particle moving along the lower nappe is considered in projectile equations (At the brink of caisson, the vertical velocity is zero for the lower nappe)

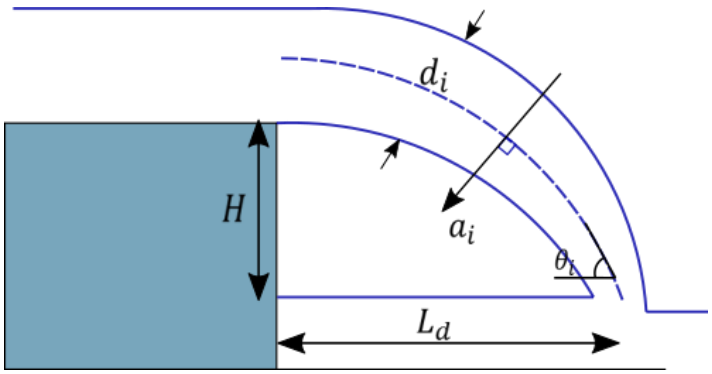

Figure 2.4 : Nappe parameters and additional acceleration during a non-aerated nappe

In Figure 2.4, θ_i is angle of nappe with respect to the horizontal axis. It assumed there is only a horizontal velocity and a zero vertical velocity at the brink of the caisson top.

The additional acceleration due to the pressure difference across the nappe (a_i) can be derived as in equation (2.6).

$$a_i = \frac{\Delta P}{\rho d_i} \tag{2.6}$$

Where, ΔP is the pressure drop behind the nappe and d_i is the thickness of the nappe.

According to Chanson (1994), the vertical acceleration of a non-aerated nappe at the brink of the step can be written as a function of the nappe sub-pressure (ΔP). Chanson, (1994) provides the relationship for acceleration due to pressure gradient across the nappe as given in equation 2.6 which verifies the derived value of a_i.

Additionally, the nappe thickness gradually reduces along the projectile path from the top of the caisson to the impingement point to maintain continuity. This is due to the increasing vertical velocity along the trajectory and as a result, the thickness of the nappe is reduced to maintain a constant flow rate. This variation of nappe thickness (d_i) is also taken into account in deriving the nappe's trajectory (See equation 2.11). Since the nappe thickness (d_i) changes along the nappe path, the acceleration (a_i) also changes accordingly.

For the motion in horizontal direction (during time Δt),

$$\Delta x_i = u_{i-1}\Delta t - \frac{1}{2}(a_{i-1}\sin\theta_{i-1})\,\Delta t^2 \tag{2.7}$$

$${u_i}^2 = {u_{i-1}}^2 - 2(a_{i-1}\sin\theta_{i-1})\Delta x_i \tag{2.8}$$

For the motion in vertical direction (during time Δt),

$$\Delta y_i = -v_{i-1}\Delta t + \frac{1}{2}\{g + a_{i-1}\cos\theta_{i-1}\}\,\Delta t^2 \tag{2.9}$$

$${v_i}^2 = {v_{i-1}}^2 + 2\{a_{i-1}\cos\theta_{i-1} + g\}\Delta y_i \tag{2.10}$$

The nappe thickness (d_i) is determined as,

$$d_i = \frac{Q}{B_C * \sqrt{{u_{i-1}}^2 + {v_{i-1}}^2}} \tag{2.11}$$

The angle of projectile with respect to the horizontal (θ_i) is calculated from,

$$\theta_i = \tan^{-1}\frac{\Delta y_i}{\Delta x_i} \tag{2.12}$$

From top point to the lowest point along the projectile, θ_i varies gradually. The value of θ is calculated for each time step and applied to equations 2.7, 2.8, 2.9, 2.10 and 2.11.

2.1.1.3 Comparison of theoretical nappe trajectories

For specific values of $Q, \Delta P, u_1, d_1$ and θ the trajectories for aerated and non-aerated nappes can be derived as shown in Figure 2.5. In each case, the lower nappe envelope is considered in Figure 2.5. The method of explicit time stepping can be used to derive projectile path of the non-aerated nappe. Explicit time stepping method calculates the respective parameters using the known parameters of the previous time step.

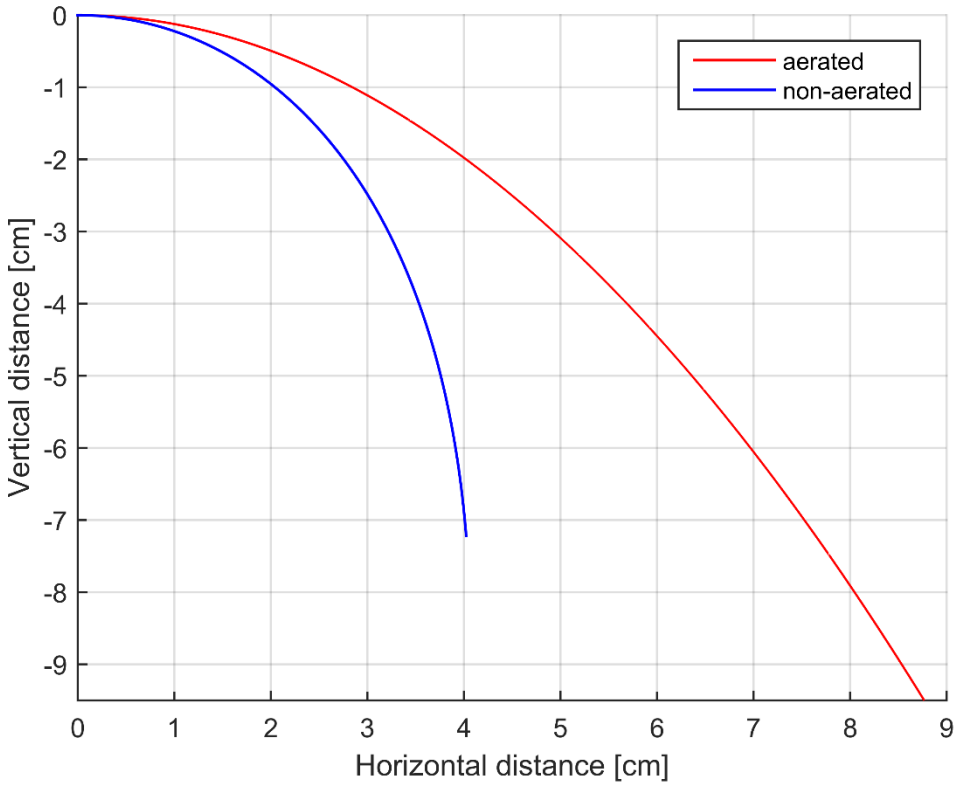

Figure 2.5 : Nappe trajectory comparison (The red line represents the trajectory for aerated nappe and the blue line represents the trajectory for non-aerated nappe. The non-aerated nappe falls a lesser vertical distance than that for the aerated nappe due to non-aeration the water level rising)

Chanson (1994) has incorporated several experimental and theoretical data to analyse the aerated nappe trajectory. Additionally, Chanson (1994) presents a number of analytically derived equations for several geometric parameters associated with the nappe trajectory of aerated nappes.

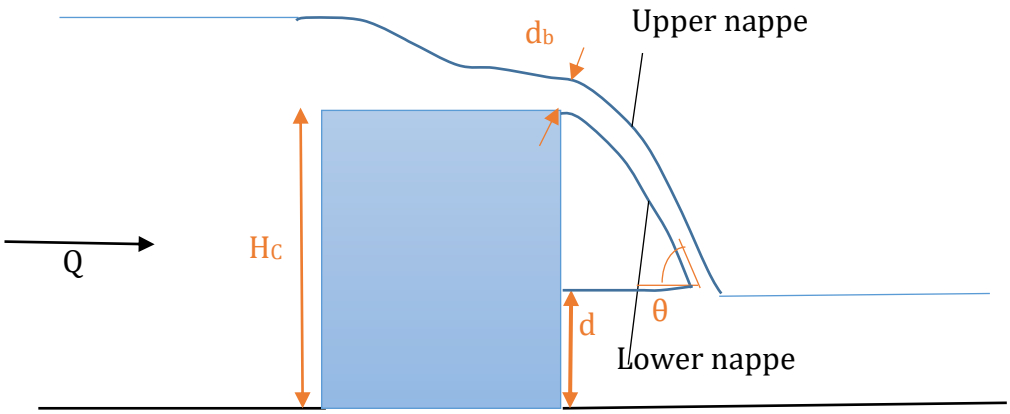

Figure 2.6 : Flow parameters during overflowing of a caisson with an aerated nappe

The nappe's angle with respect to the horizontal channel bottom (θ) is given by,

$$\tan\theta = \sqrt{2} * \sqrt{\frac{d_b}{d_c}} * \sqrt{\frac{H_C - d + \frac{d_b}{2}}{d_c}} \quad (2.13)$$

Where d_c is the critical flow depth on top of the caisson. In Hong, Huang, & Wan (2010), the drop characteristics including the drop length during an overflow situation are also derived using regression techniques and semi-theoretical approaches. Furthermore, Abdalla & Shamaa (2016) presents an analytically-derived equation for the drop length (L_d) as follows;

$$L_d = 2.12 * \sqrt{d_c(H_C + 0.33d_c)} \quad (2.14)$$

2.1.2 Hydrostatic forces from theory

During a steady overflow of a caisson breakwater, the pressure distribution at the upstream side only dependent upon the upstream water level whereas that at the downstream side, an additional component due to the non-aeration of nappe is present. Since this study ultimately focuses on the forces (mainly sliding force) applied on the caisson due to the overtopping, it is essential to have an understanding on the hydrostatic forces that are exerted on the caisson during an overtopping scenario. So as an initial step, theory can be developed to determine several relevant force parameters including horizontal force, vertical force, overturning moment. The hydrostatic forces are calculated based on the static water levels during the steady state. These theoretical equations are developed in sections 2.1.2.1, 2.1.2.2, and 2.1.2.3 below.

2.1.2.1 Horizontal force

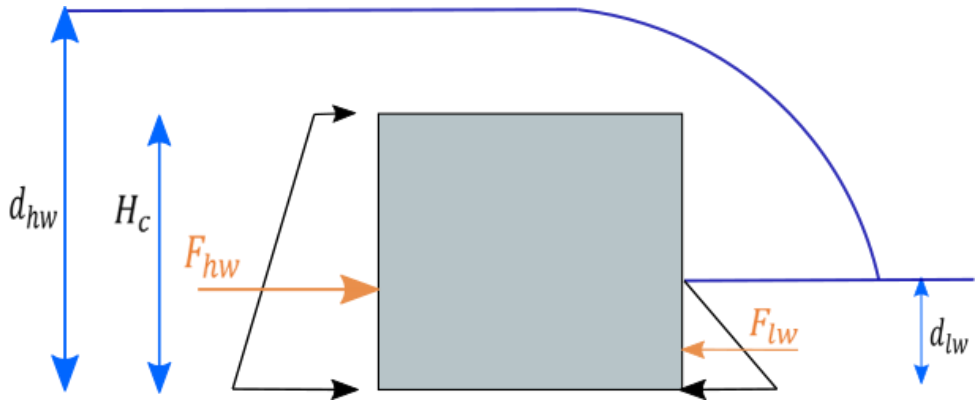

Figure 2.7 Parameters affecting hydrostatic horizontal force (F_{hw} and F_{lw} are the horizontal forces applied due to the static water levels in upstream and downstream sides respectively)

Where B_C is the caisson width, H_c is the caisson height,d_{hw} is the upstream water level and d_{lw} is the downstream water level.

The hydrostatic horizontal force ($F_{horizontal}$) is the net force due to $F_{hw}$and F_{lw} that are depicted in Figure 2.7. The forces can be formulated as shown in equations 2.15 to 2.18.

$$F_x = \int_0^{H_C \text{ or } h} \rho g(H_C - z)B_C dz \quad (2.15)$$

$$F_{hw} = \rho g B_C \left(d_{hw} H_C - \frac{{H_C}^2}{2}\right) \quad (2.16)$$

$$F_{lw} = \rho g B_C \frac{{d_{lw}}^2}{2} \quad (2.17)$$

$$F_{horizontal} = F_{hw} - F_{lw} \quad (2.18)$$

2.1.2.2 Vertical force

Similarly, the static water levels are used to calculate both $F_{vertical}$ and M_{hydro}

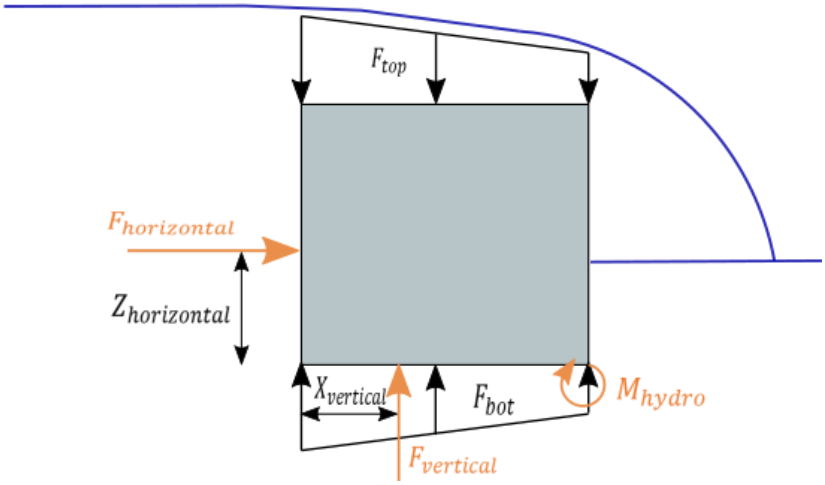

Figure 2.8 Parameters used to determine the lift force and the overturning moment ($z_{horizontal}$ and $x_{vertical}$ are the distances to point of actions of $F_{horizontal}$ and $F_{vertical}$ respectively)

Both $F_{vertical}$ and M_{hydro} are derived using the forces shown in Figure 2.8. F_{bot} arises from the pore water pressure of the porous foundation underneath, and it is assumed to be varied linearly according to Goda assumption. F_{top} is a function of flow speed on top of the caisson and it can be reduced by a rapid flow on top of the caisson. $F_{vertical}$ is the resultant force due to F_{bot} and F_{top} as shown in equation 2.19.

$$F_{vertical} = F_{top} - F_{bot} \quad (2.19)$$

2.1.2.3 Overturning moment

The moment due to hydrostatic forces (M_{hydro}) is given by,

$$M_{hydro} = F_{horizontal} \cdot z_{horizontal} + F_{vertical} \cdot (L_c - x_{vertical}) \quad (2.20)$$

2.1.3 Determination of additional horizontal force (ΔF)

2.1.3.1 The maximum additional horizontal force (ΔF_{max})

The additional horizontal force (ΔF) occurs in addition to the hydrostatic horizontal force($F_{horizontal}$) introduced in section 2.1.2.1. An estimate for the maximum additional horizontal force acting on the caisson during overflowing can be obtained using the conservation of horizontal momentum of the overflow nappe.

The total horizontal momentum is lost during the 'clinging' nappe when the nappe is attached to the caisson surface as shown in Figure 2.1. When considering the loss of horizontal momentum per unit time, a relationship for the maximum horizontal additional force (ΔF_{max}) can be developed as in equation 2.21.

$$\Delta F_{max} = \lambda \rho Q U \tag{2.21}$$

Where λ is a constant that depends on the overflow conditions, Q is the steady flow rate and U is the horizontal velocity at the brink of the caisson top. ΔF_{max} provides an estimate of the expected order of magnitude for the additional horizontal force (ΔF) due to non-aeration of the overflow nappe.

2.1.3.2 Additional horizontal force (ΔF) from theory

The additional horizontal force (ΔF) is a function of the nappe sub-pressure (ΔP). In order to estimate the additional horizontal force due to the pressure drop (ΔF), the pressure variation during both the aerated nappe and the non-aerated nappe need to be considered. The forces are determined by integrating the pressure over the surface area of the caisson.

For Figure 2.9 and Figure 2.10, it should be noted that the resultant force on the caisson is applied towards opposite direction to the hydrostatic pressure application on the caisson. Further, since the force acting on the upstream end of caisson is the same for both cases (Figure 2.9 and Figure 2.10), it is neglected.

Aerated nappe scenario

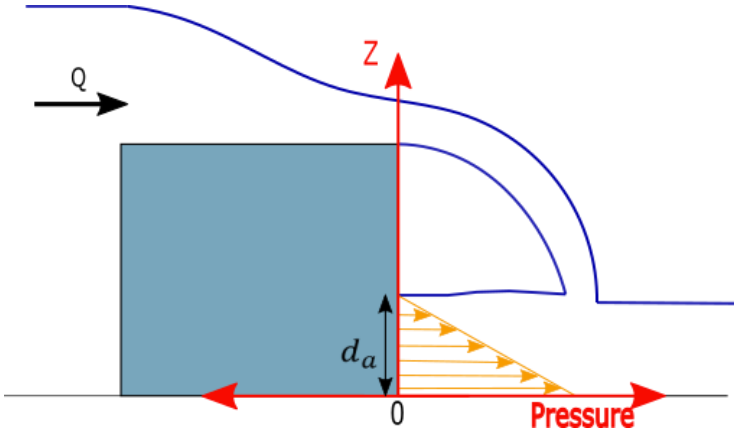

Figure 2.9 Variation of pressure during aerated nappe scenario (the resultant force on the caisson is applied towards opposite direction to the hydrostatic pressure application on the caisson)

The pressure variation acting on the caisson vertical surface is shown in Figure 2.9. The horizontal force acting on the caisson vertical surface is given by,

$$F_{aerated} = -\int_{0}^{d_a} \rho g(z - d_a) B_C dz \tag{2.22}$$

Non-aerated nappe scenario

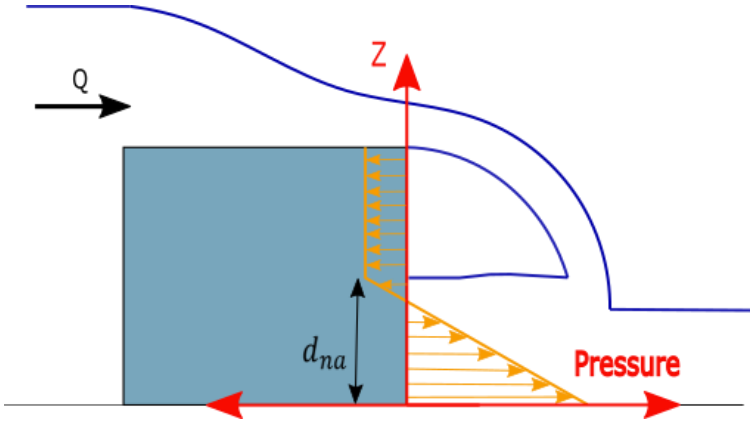

Figure 2.10 Variation of pressure during non-aerated nappe scenario (the resultant force on the caisson is applied towards opposite direction to the hydrostatic pressure application on the caisson)

The pressure variation acting on the caisson vertical surface is shown in Figure 2.10. The horizontal force acting on the caisson vertical surface is given by,

$$F_{non-aerated} = -\int_{0}^{d_{na}} \{[\rho_{eff} g(z - d_{na})] - \Delta P\} B_C dz + \int_{d_{na}}^{H_C} \Delta P B_C dz \tag{2.23}$$

Where ρ_{eff} is the effective density of water (including the air bubbles) as explained in section 3.1.6. The additional horizontal force (ΔF) arises as a result of ΔP. Therefore, ΔF can be determined from equation 2.24.

$$\Delta F = F_{non-aerated} - F_{aerated} \tag{2.24}$$

Based on the theoretical derivations starting from the nappe characteristics to the determination of the additional horizontal force (ΔF), it can be proposed to perform a physical experiment simulating a caisson overtopping scenario. When deciding on the criteria and parameters related to the proposed physical model, a number of factors needs to be considered. These are summarized below;

- High energy waves are associated with tsunami conditions and the overtopping of a caisson breakwater during a tsunami will result in accelerated flows with detached nappes. However, with respect to physical model, a simplification of the tsunami conditions is essential for pragmatic reasons. Therefore, a steady overflow of a caisson (without the rubble mound underneath) can be selected.
- During a tsunami, due to the very high heads and lack of ventilation a 'drowned' nappe (Figure 2.1) can be developed. Generally, for the physical models, such massive heads are not often applicable, leading to transition of nappes from 'clinging' to 'free'(aerated) and ultimately to a 'depressed'(non-aerated) nappe.

The applicability of the proposed physical model to the field scale can be measured quantitatively using Reynolds, Froude and Weber numbers. These are further discussed in section 3.1.2.1. An overall description on the extent of the applicability of the physical model based on the results of the analysis is included in Chapter 6.

2.1.4 Air entrainment and jet impingement

It is important to understand the ventilation process of the nappe as it relates to the pressure drop within the cavity bounded by the caisson wall and nappe. When the falling nappe impinges into the pool of water downstream of the breakwater, air can be entrained within the flow (Chanson, 1994). Not much literature is found on the air entrainment and jet impingement during a caisson overtopping. These aspects will be further discussed as part of the analysis of the governing physical processes evident in the caisson overflowing experiment in Chapter 3. Also, the dynamics of the air bubbles play a vital role in the air entrainment aspect in the nappe impingement area as well as the water column below the nappe. The air bubble dynamics falls outside the scope of this study and only a qualitative behaviour analysis is done based on the observations of the physical model.

2.2 CFD simulation using OpenFOAM

This study also focuses on the CFD simulation of a caisson overflowing experiment which is related to the Kamaishi breakwater overtopping by tsunami flow in Great East Japan 2011. The partial failure of Kamaishi breakwater calls for thorough research on the aspect of caisson breakwater overtopping and its subsequent effect on the failure witnessed. The turbulence relationship with the overtopping jet plays a vital role in understanding these matters in an effective manner. Bricker (2013) has done a numerical simulation of the overtopping scenario of the Japan tsunami 2011 using a 2D InterFoam model. A summary of the work done by Bricker (2013) that is related to this study can be presented as follows:

- Delft 3D was used to propagate the tsunami wave as a shallow water wave on to the Kamaishi breakwater (depth-averaged). OpenFOAM's InterFoam with Reynolds Averaged Navier-Stokes k–ε model (using 'Volume of Fluid' method) is used to simulate the overtopping of the composite breakwater (depth-resolving). The equations solved in the model are the k–ε equations and Reynolds equations. The inflow and outflow rates in the model are adjusted to obtain witnessed water levels during the tsunami.
- The standard (both air-water) OpenFOAM k-ε turbulence model shows strong pulling of overtopping jet towards the landward wall of the breakwater in contrast to the experiment. This is speculated to be due to an over-predicted momentum exchange at the air-water interface below the overtopping nappe.
- As a solution, reduction of turbulent eddy viscosity at the air-water interface was adopted (modelled as zero turbulence in the air) and used this modified

turbulence model to simulate the experimental results of the breakwater overtopping.

As a whole, Bricker et al. (2013) speculated that the standard k–ε turbulent model does not correctly reproduce the accurate overflow nappe behaviour due to too much entrainment of the air at the air-water interface. This can be due to the fact that at the interface, the shear stress and thus the turbulent viscosity is large. This can also be attributed to the fact that in the model, the kinematic eddy viscosity is continuous across the free surface, resulting in a large momentum diffusion between air and water. However, Bricker (2013) argues that the turbulent viscosity need to be attenuated at the interface in reality. This fact has been demonstrated by Nakayama, A. and Yokojima (2003) that in reality the turbulent viscosity of water tends to be very small (nearly zero) near the air-water interface, since the turbulent eddies of air do not move into the water just as the eddies in water do not mix with air.

OpenFOAM/InterFoam has been used in many researches that analyse the breakwater overtopping cases. Lara et al (2012) has used OpenFOAM/IH-FOAM to study wave interaction with a vertical breakwater under the action of oblique waves. In Lara et al (2012), the OpenFOAM overtopping model predictions of discharges are compared with theoretical overtopping calculations. Lara et al (2012) has revealed that the accuracy of the model results is dependent upon the wave incident angle as well as the specific section of the breakwater (i.e. trunk, head and middle section). For instance, for normal incident waves, the overtopping discharges are in good agreement with the theoretical values at both the ends of the breakwater but a large over-prediction is evident within the middle section.

Higuera et al (2014) has done a flume experiment related to wave interaction with a caisson breakwater as well as to measure the transmitted energy through the porous rubble mound underneath. Gauges were also placed to measure the overtopping over the breakwater. Then this flume has been reproduced in 2D using OpenFOAM and the turbulence was modelled using the modified k–ε model. Higuera et al (2014) indicates in modelling, certain discrepancies in water levels are observed particularly at the border of the caisson and it can be attributed to the enhanced splash of waves encountered by the caisson end. Furthermore, the modelled water layer on top of caisson is well in agreement with the experimental results according to Higuera et al (2014). The reproduction of water levels in overtopping breakwater in Higuera et al (2014) is similar to this particular study. Moreover, Higuera et al (2014) made several implications on the kinematic energy level (k) near the free surface of water in the numerical model. The k value is deemed to be higher around the free surface and also the turbulence distribution around both the free surface and structure has been diffused (Higuera et al., 2014).

These cases mainly highlight the importance of modelling turbulence accurately in OpenFOAM providing a great motivation in achieving accurate simulations.

3 Governing physical processes during caisson overtopping

This chapter is divided into three sections. In the first section of physical modelling, a full description of the physical model including the measurements, the factors considered in linking the physical model to the Kamaishi scenario and pressure drop determination are presented. The second section focuses on the behaviour of the overflow nappe and the validation of ballistic model theory against the results of the physical model. The third section includes an analysis on the other physical processes observed including recirculation and air entrainment.

3.1 Physical model

As explained in Chapter 2, a physical model is proposed to investigate the governing physical processes during a caisson overflowing and to determine the additional horizontal force.

In order to demonstrate the breakwater overflowing scenario, a laboratory experiment was conducted at one of the flumes in the Water Lab of CiTG. As the study is related to the Great East Japan tsunami 2011, the designed experiment is mainly connected with the actual scenario of the overtopping of Kamaishi breakwater during tsunami 2011. However, since the aim is to study the overflow jet, only the caisson box without the rubble mound underneath is used.

Furthermore, as the actual scenario is related to tsunami waves (long-waves), the experiment is a steady flow one, reproducing the several water levels witnessed during 2011 Japan tsunami event. The overflow depth (upstream water level with respect to crest level) as well as the water level difference between the upstream and downstream can be taken as measures to indicate the magnitude of the external force (Mitsui et al, 2016). In this case, by varying the inflow rate the overflow depth is changed.

3.1.1 Objective

The main objective of the experiment is to improve the understanding on the governing physical processes during a caisson overflowing. In addition, the behaviour of the overflowing jet is studied for different experimental conditions by varying the flow rate and tail water depth.

3.1.2 Selection of the geometric scale

In order to replicate the tsunami overtopping of Kamaishi breakwater, the actual dimensions of it are used. In this context, the geometric scale is selected based on the flume dimensions as well as the required overflow depth which is in line with the actual tsunami scenario in 2011. In order to accommodate the breakwater overflowing situation, the following condition is maintained.

Flume height > [Caisson height + Maximum overflow depth]

Considering the above requirement, a geometric scale of 1:150 is selected. The dimensions of the Kamaishi breakwater are depicted in Figure 3.1 below.

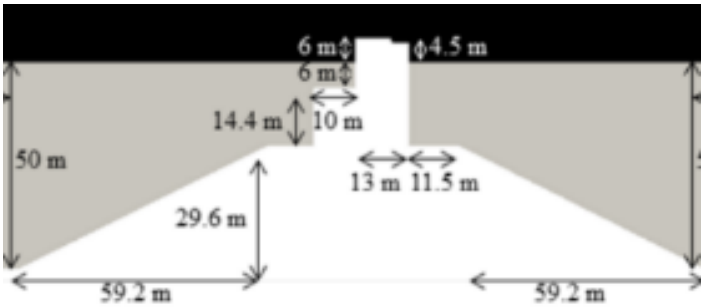

Figure 3.1 : Dimensions of Kamaishi breakwater (The caisson and rubble mound is depicted in white, while seawater and air are shown in grey and black respectively) (Bricker, 2013)

The selected dimensions for the flume experiment are summarized in Table A.1 of Appendix A.

3.1.2.1 Order of magnitude of parameters related to scaling

It is imperative to assess the disparity of flow characteristics when scaling down from the field scale to the physical model scale. The determination of the scale of Reynolds number, Froude number and Weber number for the Kamaishi breakwater overtopping and the physical model can be used to examine the effect of scaling process. Equations 3.1, 3.2 and 3.3 present the Reynolds number, Froude number and Weber number respectively.

$$Re = \frac{UL}{\nu} \tag{3.1}$$

$$Fr = \frac{U}{\sqrt{gL}} \tag{3.2}$$

$$We = \frac{\rho U^2 L^2}{\sigma} \tag{3.3}$$

Where U is the flow speed, L is the characteristic length (water depth), υ is the kinematic viscosity of water and σ is the surface tension. The kinematic viscosity and surface tension of water are taken as $10^{-6} m^2 s^{-1}$ and 72.86 mNm^{-1} respectively. Approximate values for each of the parameter can be summarized as depicted in Table 3.1

Table 3.1 Comparison of parameters for Kamaishi overtopping and physical model(The values for each parameter is determined using approximations which are summarized in Appendix B)

Parameter	Kamaishi overtopping	Physical model
Re	1.6e6	15000
Fr	0.2-1.5	0.2-1.5
We	35000	20

There is a large disparity in Reynolds numbers for the two cases. The enormous flow rate value during the tsunami overtopping of Kamaishi has led to a very high Reynolds number (high inertia force) compared to the physical model. The limit of the turbulent flow is not well-defined in flume or channel scenarios unlike in pipe flow (Hydraulics, 2000). In general, 2000 is considered as the threshold for turbulent flow (Hydraulics, 2000). In accordance with that criterion, it can be inferred that the both the cases, the flow is in *turbulent* region. Therefore, the physical model overflow scenario can be related to the Kamaishi case. In the CFD simulations, a turbulence model is used to model the flow. This will be further described in section 5.2.

The Froude number scaling is used for the scaling of the physical model. As it can be seen, for both cases the Froude numbers are in agreement. During the caisson overflowing in the physical model, the caisson is expected to behave as a perfectly operating broad-crested weir (The critical depth occurs on top of the caisson). This phenomenon can be evaluated by estimating the Froude number as described in section 3.1.5.

The Weber number evaluate the inertia forces with respect to the surface tension forces. As expected, during the tsunami overtopping the inertia forces are quite large leading a smaller Weber number. Hence, it can be inferred that the surface tension effects for field scale is negligible unlike in the scaled-down physical model where the surface tension plays a vital role in the overflow jet behaviour. The influence of surface tension effect on scaling up is discussed in section 4.2.2.

3.1.3 Experimental procedure

The experimental procedure adopted can be summarized as follows;

- The caisson box is placed inside the flume ensuring that the non-seepage of water other than overflowing and no movement or overturning of the box would occur (using clay).
- Three pressure sensors are placed along the back wall of the caisson to get pressure time series during the experiment. (See section 3.1.6 for further details)
- Then the pump is turned on and let the flow to be steady.
- With time, overflowing will start and the downstream water level will rise. (The outflow rate can be changed accordingly by adjusting the weir position at downstream).
- The water level rise in both upstream (including the overflow depth) and downstream until the steady state is reached. The variation of the water levels and the overflow jet behaviour are recorded using a video camera. (Graded vertical rulers will be located at suitable locations, so as to calibrate vertical lines on the images that will be obtained from the video camera).
- Since the trajectory of the overflow nappe need to be ascertained accurately, both vertically and horizontally graded rulers are positioned near the downstream end of the caisson.
- After the steady state is reached, artificial aeration of the space below nappe is applied.

- The final water levels at upstream and downstream and weir heights related to inflow and outflow rates are measured (Both inflow and outflow values are to be used as boundary conditions for OpenFOAM simulations).

The above procedure is repeated several times by varying the inflow rate as well as the downstream weir height (thus the downstream water level). Figure 3.2 below illustrates a schematic diagram of the flume orientation including the boundaries and position of the caisson.

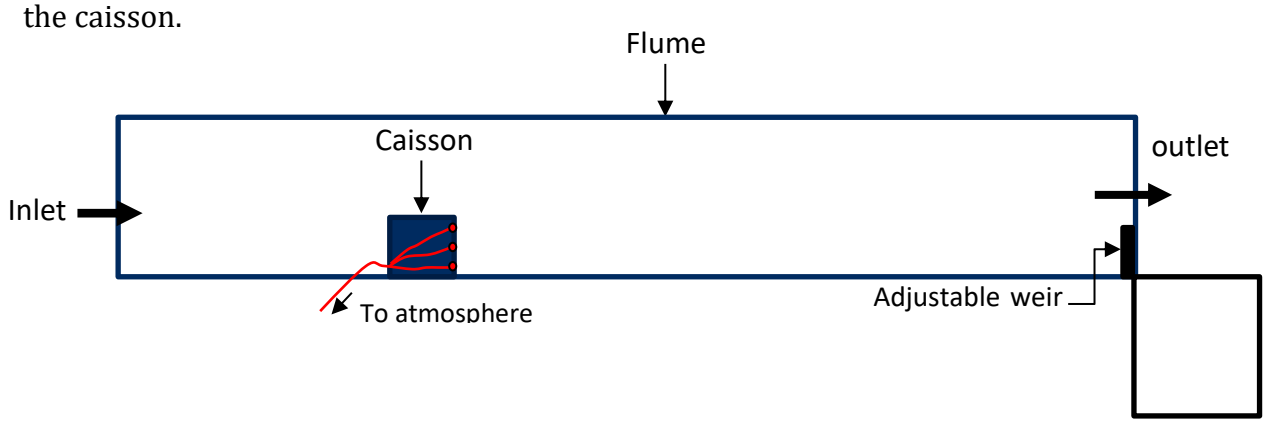

Figure 3.2 : Schematic diagram of the flume including the boundaries (The red lines indicate the locations at which pressure is measured during the experiment. The other end of the pressure sensor is exposed to atmosphere as shown)

A schematic diagram of the caisson overflowing experiment scenario including the measured parameters is shown in Figure 3.3 below.

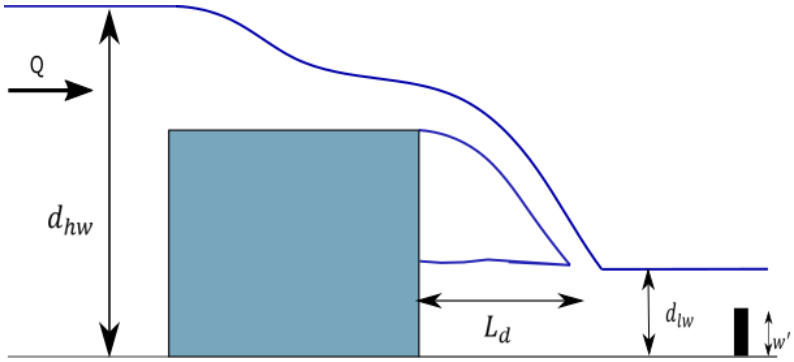

Figure 3.3 : Schematic diagram of the laboratory experiment including the measurements taken in addition to the video recording the overflowing of the caisson

The experimental conditions with respect to time can be illustrated as in Figure 3.4.

Figure 3.4 Experimental conditions with time (Each experiment can be divided into two main phases namely unsteady state and steady state as shown)

It takes some time for the flow rate to be steady as shown in Figure 3.4. Once the steady state is reached, two separation aerations of the nappe (aeration 1 and aeration 2) are applied to observe the fluctuations of the nappe trajectory behaviour.

3.1.4 Determination of the flow rate

When the lab experiments are conducted by allowing overflow of a caisson box in the water flume, different behaviours of the overflow jet are observed at different flow rates.

Once the flow becomes steady, the flow rate is calculated based on the flow over a sharp-crested weir at the downstream end of the flume as shown in Figure 3.2. The calculation of the inflow rate (Q) using the Volgens (Rehbock stuw) weir equation is included in Appendix C. The inflow rates that are used in the physical model are summarized in Table 3.2.

Table 3.2 : Measurements of the experimental runs performed

Test No	Upstream Water Level w.r.t. caisson crest (d_0) [cm]	Tail water depth [cm]	Q_{in} [litre/s]
1	5.02	9.5	2.47
2	6.63	10.87	3.90
3	6.72	9.4	4.05
4	6.50	9.05	3.84
5	3.27	7.71	1.23
6	5.37	14.43	2.82
7	8.32	2.87	5.78
8	3.27	12.59	1.22
9	6.77	9.31	4.09
10	5.00	7.99	2.50

A total of ten experimental runs were performed by varying both the inflow rate and tail water depth. In this report these experiments are referred as Test_n, where n=1,2,3…..,10.

The qualitative behaviour of overflow jet has a direct relationship with the magnitude of the inflow rate. When the inflow rate is relatively low (<1.5 litre/s), the flow over the caisson tends to follow the surface of the caisson which is due to the 'Coanda' effect. Coanda effect can be generally described as the tendency of a fluid jet to adhere to close by solid surfaces (Lalli et al., 2010). This qualitative behaviour of overflow jet is further explained in Appendix D.

In order to evaluate the nappe behaviour (section 3.2) and to be used in CFD simulation (section 5.2), Test_10 (Q=0.0025 m^3/s, tail water depth=7.99 cm) is used. The reason for selecting this particular test is that it shows the distinctive nappe behaviours in a more pronounced manner.

3.1.5 Behaviour of caisson as a broad-crested weir

During the laboratory experiment, a caisson is used to be overflowed by a gradually increasing flow until a steady state is achieved. In this scenario, the caisson acts as a broad-crested weir. For a perfectly operating broad-crested weir, the critical flow depth should occur on top of the caisson. Usually next to the upstream end of the weir crest the flow is accelerated on top of the crest and becomes super-critical at the downstream end of crest (Gonzalez & Chanson, 2007). As shown in Figure 3.5 below, the flow depth changes indicating the increase of flow speed from sub-critical to super-critical region.

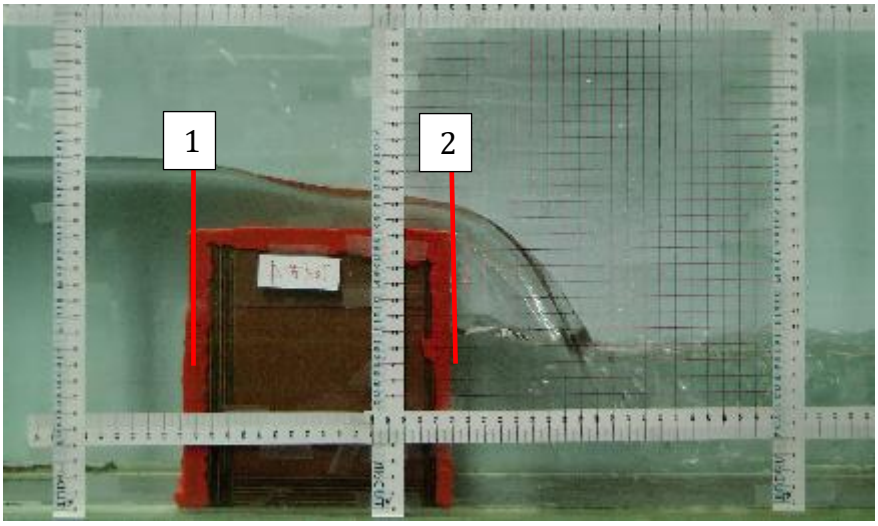

Figure 3.5 : Transition of flow regime from sub-critical to super-critical over the caisson during the laboratory experiment

To identify the flow regimes, Froude number can be accompanied as follows; (Test_10)

Position	Water depth [h] (m)	Flow speed [U] (m/s)	Froude No	Flow regime
(1)–upstream end	0.048	0.26	0.38 (<1)	Sub-critical
(2)-downstream end	0.02	0.63	1.42 (>1)	Super-critical

Therefore, it is evident that the flow regime changes from sub-critical region to super-critical region on top of the caisson. Froude number is found from equation 3.2. The critical flow depth (d_c) occurs when Fr equals to 1. The critical flow depth (d_c) of 0.0252m occurs at 4.7 cm left of the downstream end of the caisson.

The transition of flow from sub-critical region to super-critical region will be used as a validation of the OpenFOAM simulations later in Chapter 5.2.

3.1.6 Measurement of pressure during the laboratory experiment

In order to measure the pressure time series along the downstream vertical surface of the caisson, three pressure sensors were used positioned as depicted in Figure 3.6.

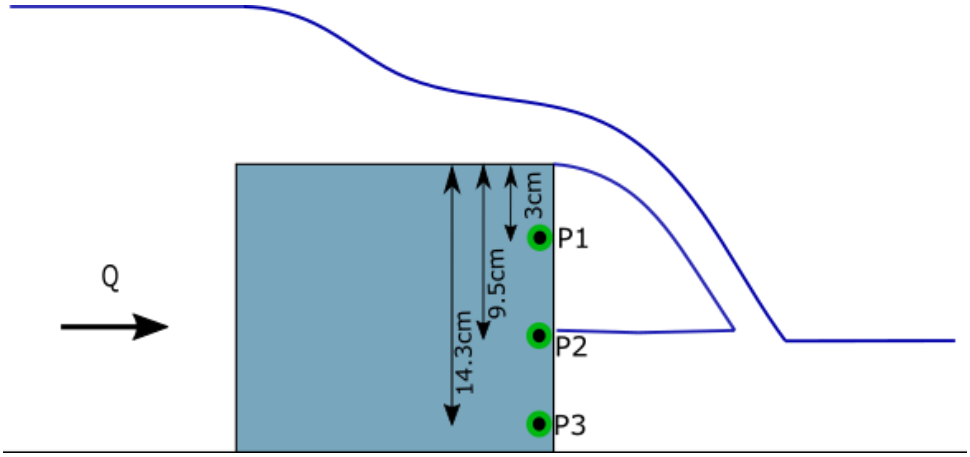

Figure 3.6 Positioning of three pressure sensors (P1=top, P2=middle, P3=bottom)

The pressure sensors used in the experiment are 'differential' pressure sensors which provide the difference of two independent pressure sources. For the experiment conducted, one end of the pressure sensors is always opened to atmosphere. So, the subsequent output pressure readings are measured relative to the atmospheric pressure. All three pressure sensors are calibrated.

A detailed description of the pressure sensor used is included in Appendix E and the calibration process and the results can be found in Appendix F.

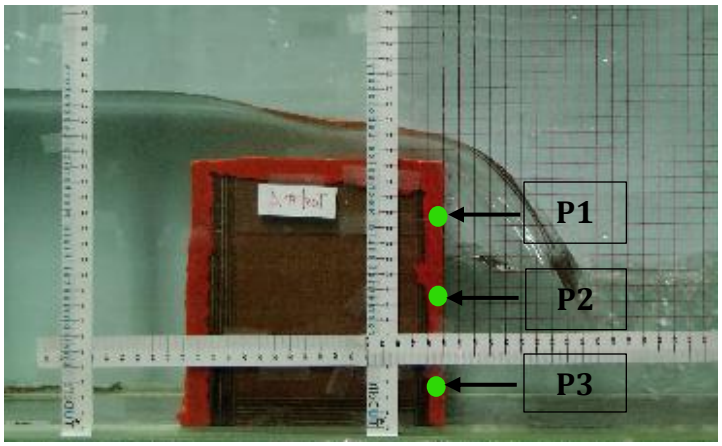

Figure 3.7 : Pressure sensors used in the experimental set-up

As it can be seen from Figure 3.7, the top pressure sensor (P1) will be measuring the pressure of air when the steady state of flow is passed. Based on the principle of the type of pressure sensor used, it is not possible to accurately read the pressure when exposed to air. Thus, the pressure readings of P1 is not used for further analysis. Both the pressure sensors below (P2 and P3) are submerged under which they operate accurately. A further analysis of the pressure results and the derivation of the effective density of water (ρ_{eff}) is included in Appendix J.

3.1.6.1 Determination of pressure reduction (ΔP) behind the nappe

In order to evaluate the effect of the air entrainment of the nappe during the caisson overflowing, the pressure reduction behind the nappe (ΔP) needs to be determined. The pressure variation for the non-aerated case can be depicted as illustrated in Figure 3.8.

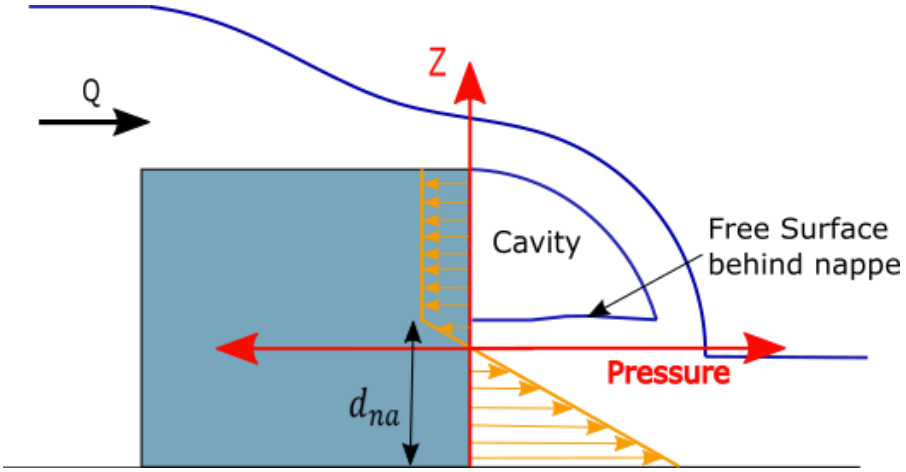

Figure 3.8 Pressure variation along the vertical surface of the caisson due to downstream conditions (The pressure below zero is sub-atmospheric pressure)

As depicted in Figure 3.8, the sub-atmospheric pressure at the free surface behind the nappe is equal to the pressure within the cavity. Since this is measured with respect to the atmospheric pressure, this is equals to ΔP. From the level of free surface, the pressure linearly increases towards the bottom of the flume based on the hydrostatic assumption.

3.1.6.2 Hydrostatic calculation for ΔP

Since the top pressure sensor (P1) did not function accurately as it was exposed to air, the ΔP value needs to be determined using the pressure measurements gathered from the bottom(P3) pressure sensor.

To depict the hydrostatic pressure values, Figure 3.9 below, which incorporates manometer readings, can be used. Assume the manometer is placed at the level of bottom pressure sensor (P3).

In Figure 3.9, position 1 represents the aerated case whereas position 2 represents non-aerated case. During the aerated case, the air above water is in atmospheric pressure while during non-aerated case, the air is of sub-atmospheric pressure ($P_{atm} - \Delta P$). The water piles up for additional depth of d_{na} for the non-aerated case as shown in Figure 3.9. Considering the pressure at the bottom pressor sensor (P3) which is at 3cm from the bottom.

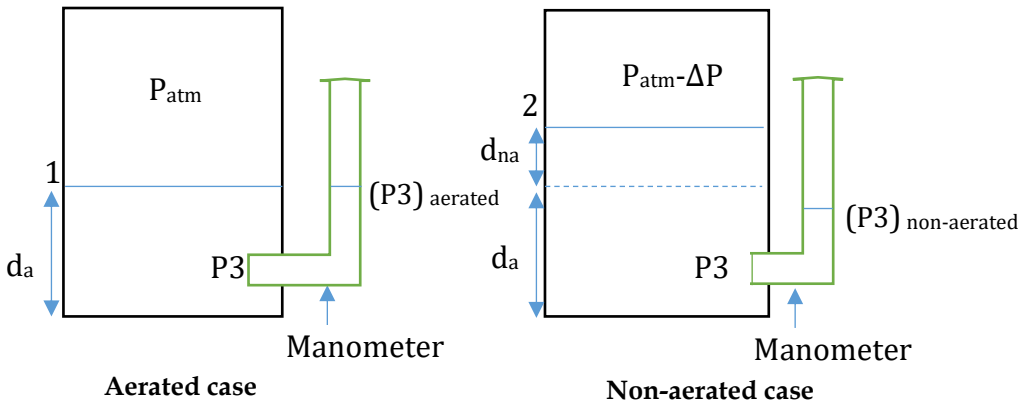

Figure 3.9 : Pressure sensor readings during aerated and non-aerated conditions

For aerated nappe,

$$\overline{d_a}\rho g + P_{atm} = \overline{(P_3)_{aerated}} + P_{atm} \tag{3.4}$$

$$\overline{(P_3)_{aerated}} = \overline{d}_a \rho g \tag{3.5}$$

For non-aerated nappe,

$$\overline{d_a}\rho g + \overline{d_{na}}\rho_{eff} g + (P_{atm} - \Delta P) = \overline{(P_3)_{non-aerated}} + P_{atm} \tag{3.6}$$

$$\overline{(P_3)_{non-aerated}} = \overline{d_a}\rho g + \overline{d_{na}}\rho_{eff} g - \Delta P \tag{3.7}$$

From equations (4.19) and (4.21),

$$\Delta P = \left(\overline{(P_3)_{aerated}} - \overline{(P_3)_{non-aerated}}\right) + \overline{d_{na}}\,\rho_{eff} g \tag{3.8}$$

The ΔP value can be calculated using equation (4.22) which is based on the hydrostatic assumption. In addition, the ΔP value can also be determined using a non-hydrostatic method and it is explained in detail in Appendix G. However, it is found that the governing conditions below the nappe are hydrostatic rather than non-hydrostatic.

3.2 Behaviour of overflow nappe

It was observed that the artificial aeration results in an increase of radius of curvature of the nappe's trajectory (nappe pulls further away from caisson) and the dropping down of water that is held up against the caisson wall. These observations are depicted in Figure 3.10 where it compares the video frames before and after the aeration.

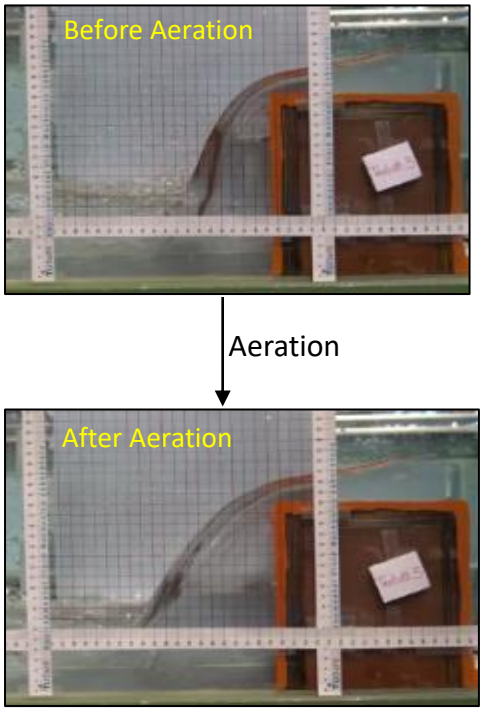

Figure 3.10 : Comparison of overflow nappe trajectory and the water level behind the nappe before and after the aeration

The behaviour of overflow nappe during the laboratory experiment is studied in detail as it provides valuable implications on the additional horizontal force acting on the caisson due to pressure reduction behind the nappe. However, the gradual development of the nappe trajectory until the steady state is achieved needs to be considered in understanding the aspects such as the pressure reduction below the nappe, air entrainment as well as their corresponding effect on the nappe trajectory. These aspects can be further explained as follows;

Figure 3.11 below indicates the overflow nappe behaviour with time during the physical model.

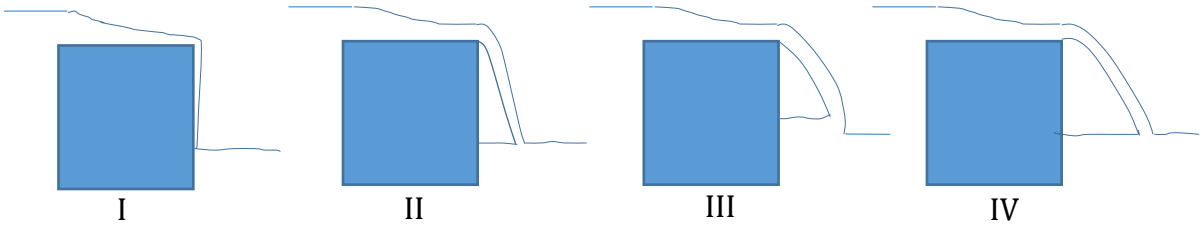

Figure 3.11 : Nappe behaviour with increasing time (I, II and III depict clinging, free and depressed nappe respectively. From III to IV, an artificial aeration is inflicted behind nappe)

No	Description
I	Still the steady state is not achieved. With the insufficient momentum of the flow due to low flow rate, the 'coanda' effect comes into play and the water flow clings to caisson face (clinging nappe)
II	When the momentum of the flow gets increased the nappe moves away from the caisson allowing an air space behind the nappe
III	When the nappe pulls further away from caisson, the air gets entrained in the nappe creating a sub-atmospheric pressure below nappe. The air entrainment causes the water to get pile up against the vertical caisson surface. This results in a water level difference between the water surface behind the nappe and downstream of nappe. Another important phenomenon that results from above conditions is that the nappe gets pulled towards the caisson due to the pressure gradient across the nappe (depressed nappe)
IV	When the aeration of the nappe is inflicted, the nappe trajectory deviates significantly further away from the caisson. And the water that has been piled up against the caisson goes down to the level of tail water depth (free nappe)

In this study, the deviation of the nappe from non-aerated case (III above) to aerated case (IV above) is studied.

The air under the overflow nappe is in sub-atmospheric pressure in part III in Figure 3.11. As depicted in Figure 3.11 above, once the overflow jet pulls further away from the caisson end and the air gets entrained, this sub-atmospheric pressure will get further reduced increasing the pressure difference between upper nappe (subjected to atmospheric pressure) and lower nappe. This reduction of pressure below the nappe with respect to atmospheric pressure will pull the overflow jet towards the caisson increasing the curvature of the jet trajectory (resulting in a reduction of the nappe's radius of curvature).

3.2.1 Validation of the ballistic model against the physical model results

The nappe trajectories for both the aerated nappe and the non-aerated nappe can be obtained using the ballistic model derived in equations 2.6 to 2.12. For the non-aerated nappe, the additional acceleration is calculated using equation 2.6 in which the corresponding pressure drop is found from equation 4.22.

From the 'explicit time stepping method' the nappe projectile for the lower nappe is obtained as shown in Figure 3.12. The Δt value used for the nappe profile development is $1e{-}7$ seconds below which the trajectories converge.

The derived trajectory of the nappe from the ballistic model (for Test_10) is depicted in Figure 3.12 and a comparison is made with the physical model measurements. The physical model coordinates are recorded to an accuracy of 2.5 mm.

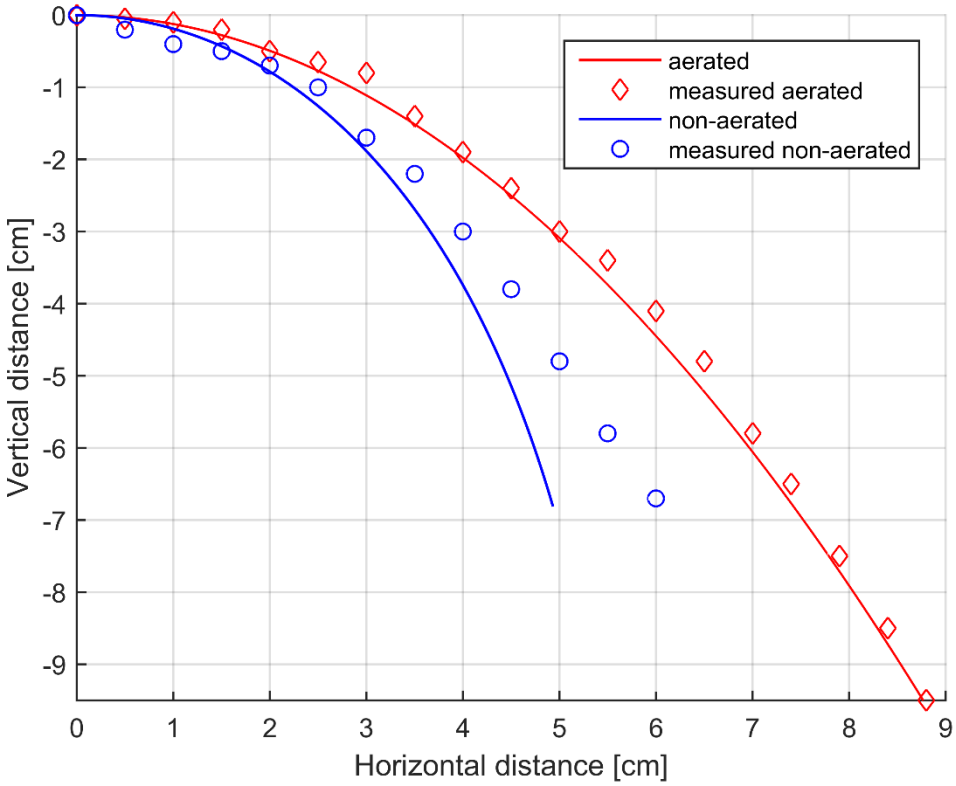

Figure 3.12 : Derived trajectory of the nappe for Test_10 (The 'red' color represents the trajectory for aerated nappe and the 'blue' color represents the trajectory for non-aerated nappe. Also the solid lines depict the results of ballistic model whereas the points of respective colors illustrate the measured coordinates from the physical model. The non-aerated nappe falls a lesser vertical distance(6.8 cm) than that for the aerated nappe(9.5 cm).In both the cases, the lower envelope of the nappe's trajectory is considered)

The root mean square error (RMSE) between the calculated and measured nappe trajectory positions are 0.19cm and 0.51cm for aerated nappe and non-aerated nappe respectively. A satisfactory fit between the theoretical and experimental nappe trajectories for the aerated case is observed. Comparatively higher error for the non-aerated nappe over the aerated nappe is found leading to a mismatch of theoretical and measured non-aerated nappe trajectory.

The pressure drop behind the nappe (ΔP) determined for non-aerated case seems to be overestimated. This also leads to increased additional acceleration (a) as per equation 2.6. A sensitivity analysis with respect to the pressure drop (ΔP) is performed and the best-fit trajectory curve for the non-aerated nappe is found by reducing the ΔP by 33%. The corresponding nappe trajectories are depicted in Figure 3.13.

.

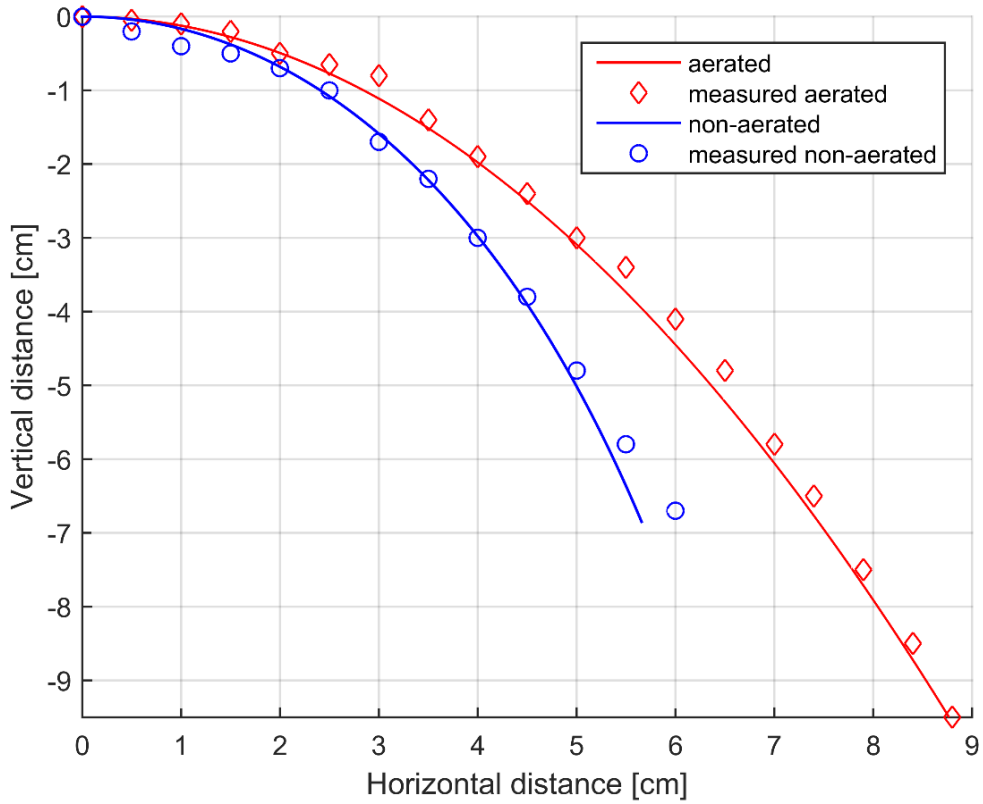

Figure 3.13 : Derived trajectory of the nappe for Test_10 using a 33% reduced ΔP value

The RMSE value for the best-fit curve (with a 33% reduction of ΔP) and the measured positions of the non-aerated nappe is 0.16cm. This value less than the RMSE of the non-aerated nappe for initially derived ΔP.

There can be number of reasons for the overestimation of ΔP. The ΔP value is determined using a hydrostatic assumption as explained in section 3.1.6.2. Even though the water level below the nappe is stationary, the ΔP might not be stationary. The ΔP value might be time-varying and it might be balanced by the air being moving into the cavity from outside which is a possibility during the experimental conditions.

In addition to the above reasons, the effect of surface tension on the nappe trajectory is investigated. According to Sarginson (2017), surface tension tends to depress the overflow nappe(make the nappe deviate towards the caisson). The effect of surface tension is higher when the radius of curvature is low (Sarginson, 2017).

In this context, the comparison of measured and theoretical non-aerated nappe is carried out. The effect of surface tension is not included in theoretical derivations. For non-aerated nappe, the radius of curvature is low and the nappe should be more depressed due to high surface tension. However, the measured non-aerated nappe is less depressed than the theoretical. From Figure 3.12 , it can be seen that the effect of the overestimated ΔP on the theoretical non-aerated nappe is more noticeable as it is more depressed than the measured. Thus, it can be interpreted that the effect of ΔP is more pronounced than that of surface tension.

3.3 Recirculation and air entrainment

In this section, the processes of recirculation and air entrainment are discussed together with the other physical processes observed during the physical model.

3.3.1 Flow separation and recirculation

The phenomenon of 'flow separation' can be expected based on certain flow conditions and obstacle geometries present in a caisson breakwater overflowing scenario. Flow separation occurs as a results of an adverse pressure gradient. Further, flow separation can be expected due to the widening or deepening of the flow (Uijttewaal, Turbulence in hydraulics CT5312: Lecture notes). This is depicted in Figure 3.14.

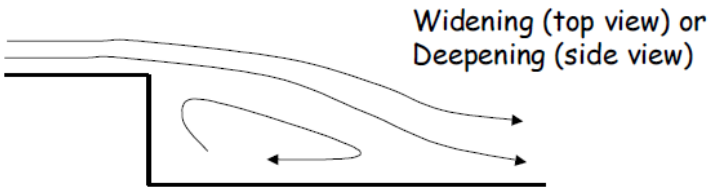

Figure 3.14 : Flow separation due to widening and deepening of flow (Turbulence in hydraulics CT5312: Lecture notes)

During the caisson overflowing scenario, the caisson acts as a backward facing step. At sharp corners such as backward facing steps, flow separation can be expected (Uijttewaal, Turbulence in hydraulics CT5312: Lecture notes). This results in a recirculation zone as shown in Figure 3.15. In addition, the formation of corner eddies and a reattachment zone can be anticipated as well.

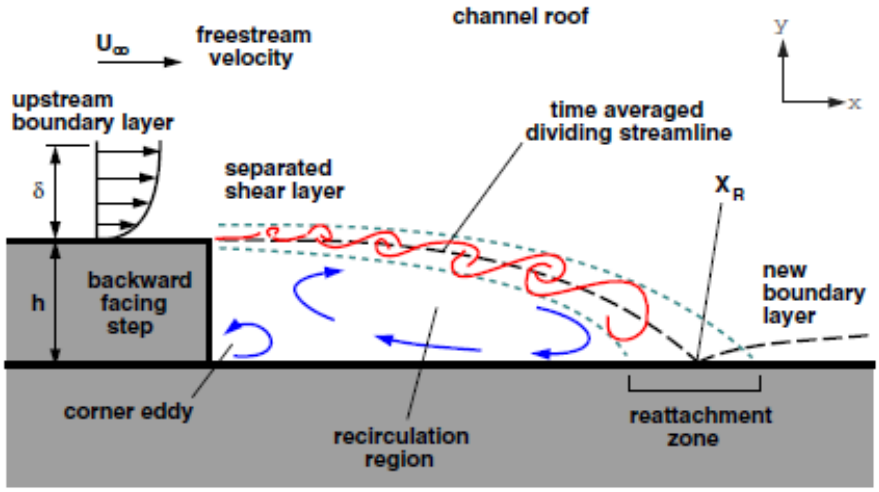

Figure 3.15 Detailed flow features of the backward facing step flow (Saleel, 2013)

An adverse pressure gradient (ΔP_{dyn}) is developed downstream of the caisson. The adverse pressure gradient (ΔP_{dyn}) drives the recirculation as shown in Figure 3.16. For simplicity, the recirculation path can be approximated to a circle or an ellipse as depicted in Figure 3.16. When a vertical line is considered, the top (X) and bottom (Y)

intersections of the recirculation path have only horizontal velocity. Also, when averaged throughout the recirculation zone, the net vertical velocity is zero. This factor emphasizes that the conditions under the nappe are not inclined towards non-hydrostatic but closer to a hydrostatic situation. This hydrostatic nature is verified by the analysis included in Appendix G. Figure 3.16 depicts the conditions governing the flow dynamics model behind the nappe.

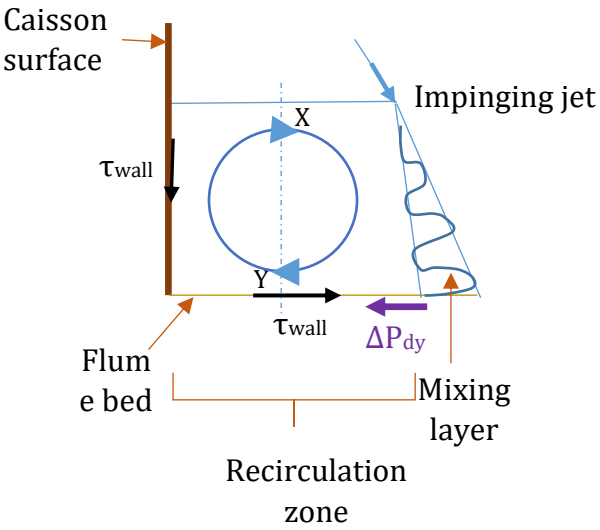

Figure 3.16 : Conditions governing the recirculation under the nappe

3.3.1.1 Mixing of overflow jet into ambient water

The mixing layer is the region from the overflow jet impinging into the pool to the point where the jet hits the bottom (See Figure 3.17). A shear stress gradient will be developed along this mixing layer. After the overflow jet impinges into the pool of water, until the bottom is reach mixing of water jet with the ambient water causes a head loss. This mixing head loss (ΔH_{mixing}) can be attributed to the mixing due to entrainment of water (of the jet) into the ambient water. This results in a reduction of velocity along the path of jet within the pool of water. Therefore, the velocity at which the jet impacts the bed is less than the impinging velocity at the pool of water line ($V_{bot} < V_{imp}$).

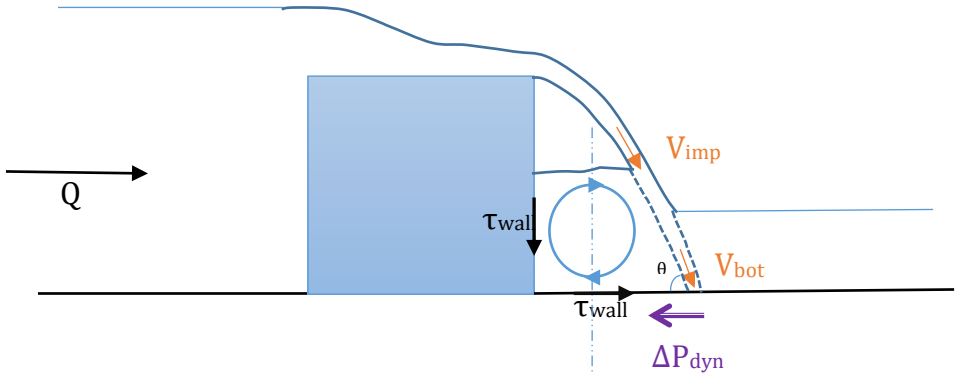

Figure 3.17 : Recirculation driven by the adverse pressure gradient (V_{imp} is the flow speed at which jet hitting the pool of water, V_{bot} is the flow speed hitting the bottom and τ_{wall} is the wall friction)

According to Fischeret al., (1979), the mean velocity distribution across a submerged jet can be represented by a function of the form shown in equation 3.9.

$$w = w_m f(\frac{x}{b_w}) \tag{3.9}$$

Where w_m is the initial velocity, x is the distance from caisson edge, b_w is the value of x at which w reduces to 0.5 w and function f is of Gaussian form. As an approximation, the velocity at the bottom (V_{bot}) can also be derived from this relationship.

3.3.1.2 Dynamic pressure gradient (ΔP_{dyn})

A stagnation pressure will be developed at the point where the jet hitting the flume bottom. The dynamic pressure (in meters) at the point where the jet hitting the flow can be given as $\frac{Vbot^2}{2g}$.

Therefore, the dynamic pressure gradient (ΔP_{dyn}) along the horizontal direction in meters is given by equation 3.10. A constant of β is used to account for the directional dissimilarity between the stagnation pressure and ΔP_{dyn} .

$$\Delta P_{dyn} = \beta \frac{\rho(V_{bot} sin\theta)^2}{2} \tag{3.10}$$

The ΔP_{dyn} drives the recirculation flow within the recirculation region as shown in Figure 3.17.

3.3.1.3 Friction due to the flume bottom and caisson surface (τ_{wall})

There can be a friction loss due to the friction of the wall. The friction of wall (τ_{wall}) can hinder the recirculation flow and it can be approximated to,

$$\tau_{wall} = \frac{1}{2}\rho C_f u^2 \tag{3.11}$$

Where, ρ is the density of water, u is the characteristic velocity in the recirculation zone and C_f is the wall skin friction coefficient. The value of u is determined using the assumption of 0.3 times the free stream velocity.

As illustrated in Figure 3.17, friction from both the flume bed and the caisson surface need to be taken into account for the recirculation flow. As both of them are smooth surfaces, a C_f value of 0.06 is applied. The balance between ΔP_{dyn} and τ_{wall} gives an indication on the speed of the recirculation happening under the overflow nappe. Therefore,

$$Recirculation\ rate\ \alpha\ (\Delta P_{dyn} - \tau_{wall})$$

However, the constant of proportionality of the ΔP_{dyn} is not known for the driving of the recirculation flow. For Test_10, the values for each term in equations 3.10 and 3.11 can be determined as summarized in Table 3.3.

Table 3.3 : Approximate values for the parameters affecting the dynamic pressure gradient and wall friction for Test_10

Parameter	Value
V_{imp}	1.49 m/s
V_{bot}	0.51 m/s
β	0.1
ΔP_{dyn}	12.1 Pa
u	0.13 m/s
C_f (smooth surface)	0.06
τ_{wall} (both flume bed and caisson surface)	0.51 Pa

For this particular test (Tset_10), the ΔP_{dyn}(in Table 3.3) is only 4% of the derived ΔP which suggests that the local pressure gradients within the recirculation zone hardly contribute to the water depth rising below the nappe. Thus, it can be inferred that the air entrainment by the overflow jet is the major mechanism that cause the pressure drop and subsequent water level rising. The process of air entrainment and quantification of the rate of air entrainment are discussed in section 3.3.2.

3.3.2 Air entrainment during the caisson overflowing

During an overflowing of the caisson in the physical model, the implications from the air entrainment process and their effect on the other mechanisms need to be addressed.

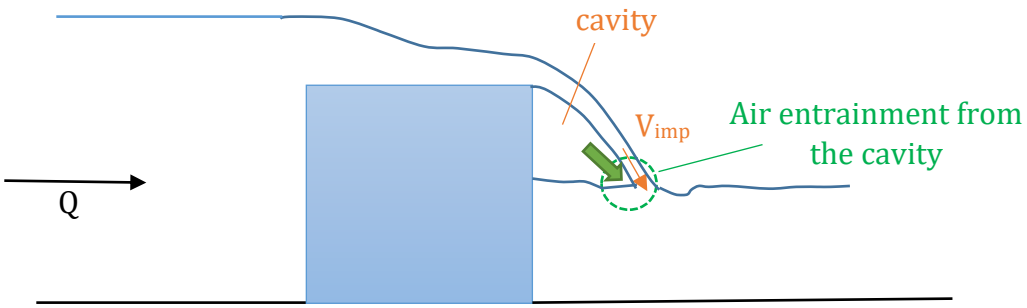

Figure 3.18 : Air entrainment process from the overflow jet impinging (Air entrainment mainly occurs in the region which is encircled)

When the overflow nappe intersects the receiving pools of water, air is entrained within the flow jet (Chanson, 1994). As the water jet impinges into the pool of water, it pushes the free water surface downwards, and due to the inertia of the jet, the air within the cavity gets entrained. This air entrainment is evident from the large number of air bubbles being circulating in the vicinity of the jet impingent position. Due to the buoyancy, these air bubbles try to pull upwards. But as the flow is directed downstream, most of these air bubbles move downstream and escape while some catch up with the recirculation below the nappe. These air bubbles that move into recirculation zone might escape back into the cavity between nappe and the caisson wall.

If the cavity between the nappe and the caisson wall is not aerated, the pressure in the cavity becomes sub-atmospheric (Chanson, 1994). Also, the free-surface below the nappe goes up to account for the lost air within the cavity as shown in Figure 3.19.

An idea regarding the air entrainment process can be gained by the oscillation of the free-surface below the nappe.

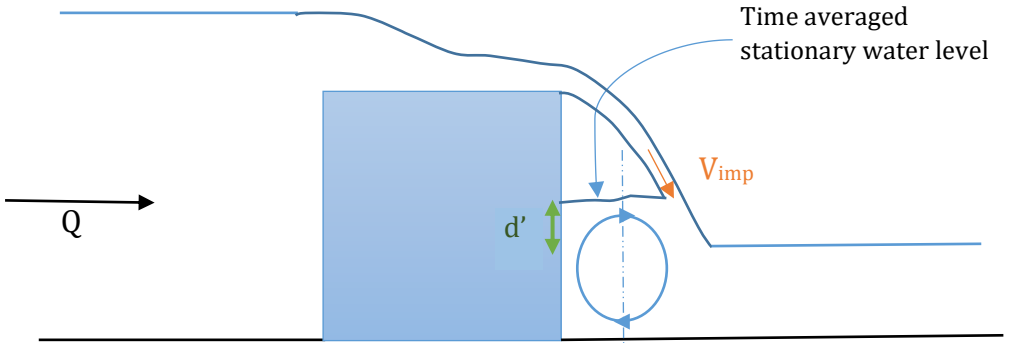

Figure 3.19 : Mechanisms that give implications on the air entrainment process

In the experiments conducted, it can be observed the free-surface reaches equilibrium when taken a time average of the free-surface oscillation. Free-surface reaching the equilibrium can be taken as an indicator that there is no further air entrainment. However, this assumption is valid only when there is no air coming in the cavity from outside. If such air addition from outside is present, the continuous air entrainment from cavity by the overflow jet will be balanced out. This would oppose the assumption of ΔP being stationary leading to the fact that the ΔP is indeed time varying as pointed out in section 3.2.1. The observation of air bubbles during the non-aerated nappe also confirms the continuous air entrainment.

3.3.2.1 Determination of the air entrainment rate

It can be hypothesized that the amount of air entrained from the cavity has a positive relationship with the velocity at which the jet impinges into the pool of water.

The air entrainment process is the contributing factor for the generation of the additional horizontal force component (ΔF) as the air entrainment is proportional to the pressure drop behind the nappe. As the amount of air entrained is proportional to the free-surface rise below the nappe (d'), by examining d' value a relationship can be developed for the additional horizontal force (ΔF) acting on the caisson.

In order to determine the air entrainment rate during the overflowing of the caisson in the physical model, the pressure time series can be used. The pressure time series of the bottom pressure sensor (P3) for Test_10 is shown in Figure 3.20.

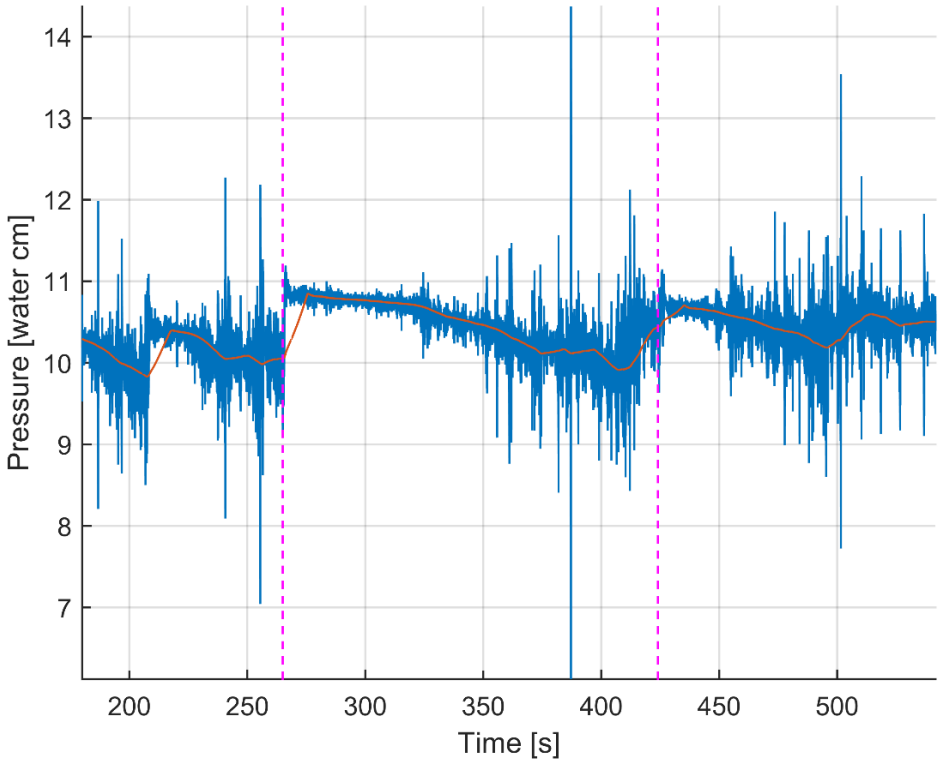

Figure 3.20 : Pressure time series of the bottom pressure sensor(P3). The red dotted vertical lines depict the two aerated points. The orange line is the 10 seconds moving average.

As shown in Figure 3.20, the moving-average of the pressure reduces approximately linearly after the aeration point (t=265s) until 365s implying a relatively constant air entrainment rate. By incorporating the water level rise under the nappe (d') during the specific time period (265s-365s), the air entrainment rate is calculated as shown in Appendix H. It is taken as the water volume that risen equals to volume air within the cavity that was entrained assuming that there is no air entrainment from outside.

In order to develop the relationship of air entrainment rate with the impinging velocity (V_{imp}),the corresponding V_{imp} is determined using the general projectile motion. The results for are summarized in Table 3.4.

Table 3.4 : Comparison of air entrainment rate and the jet impinging velocity for selected tests

Test	Q (l/s)	Tail water depth (cm)	Air entrainment rate ($m^3/m/s$)	V_{imp}(m/s)
4	3.84	9.05	9.81E-06	1.43
9	4.09	9.31	2.23E-05	1.44
3	4.05	9.4	3.12E-05	1.63
10	2.5	7.99	1.07E-05	1.49

Considering the results of Tests 4,9 and 3, it can be established the air entrainment rate increases with increasing V_{imp}. The slightly eccentric results for Test_10 can be interpreted by the comparatively low tail water depth and flow rate when compared with other tests considered.

4 Determination of relevant forces and scaling up

In this chapter, the magnitude of the relevant forces that are derived theoretically in Chapter 2 are determined. The basis of scaling up is discussed and the scaled-up forces are determined together with the other external parameters such as flow rate and water levels. In terms of forces, the applicability of physical model results in the field scale is analysed. The limitations of scaling up are identified.

4.1 Determination of additional horizontal force (ΔF)

The additional horizontal force (ΔF) due to the pressure drop behind the nappe increases the sliding force during a caisson overtopping situation. As explained in section 2.1.3.1, the maximum ΔF can be derived using equation 2.21. This provides an estimate on the expected order of magnitude for ΔF.

According to equation 2.21, the maximum additional horizontal force (ΔF_{max}) is dependent upon the flow rate (Q). Based on the flow rates that are used in the physical model the order of magnitude approximates to $40N$ (To account for the overflow conditions, the constant λ equals 2 is used).

The hydrostatic horizontal force, pressure drop (ΔP) and additional horizontal force (ΔF) are determined from equation 2.18, equation 3.8 and equation 2.24 respectively.

Table 4.1 summarizes the results obtained for the each of the experimental run.

Table 4.1 Additional horizontal forces (ΔF) in the physical model

Test number	Q [litre/s]	Upstream water level [cm]	Tail water depth [cm]	Hydrostatic force [N]	ΔP [Pa]	ΔF [N]
1	2.47	22.02	9.5	35.64	324.57	15.78
2	3.9	23.63	10.87	38.30	521.28	24.62
3	4.05	23.72	9.4	41.45	388.34	18.52
4	3.84	23.5	9.05	41.34	255.11	11.05
5	1.23	20.27	12.59	32.80	33.09	1.39
6	2.82	22.37	14.43	25.52	19.59	0.84
7	5.78	25.32	2.87	54.41	1509.78	73.64
8	1.22	20.27	12.59	23.32	38.11	1.96
9	4.09	23.77	9.31	41.78	570.87	25.40
10	2.5	22.3	7.99	39.09	317.95	14.83

In general, the ΔF accounts for 15%-30% of the total horizontal force. Some eccentricities can be observed in Test 5, 7 and 8 due to the out of order combinations of flow rates and tail water depths. For instance, in Test_7, the flow rate is maximised while keeping the tail water depth is kept to a minimum, which has resulted in an enormous ΔF value.

The pressure reduction is the main factor that causes the additional force on the caisson. Therefore, higher the ΔP value, higher the additional horizontal force exerted on the caisson, which is depicted by Figure 4.1

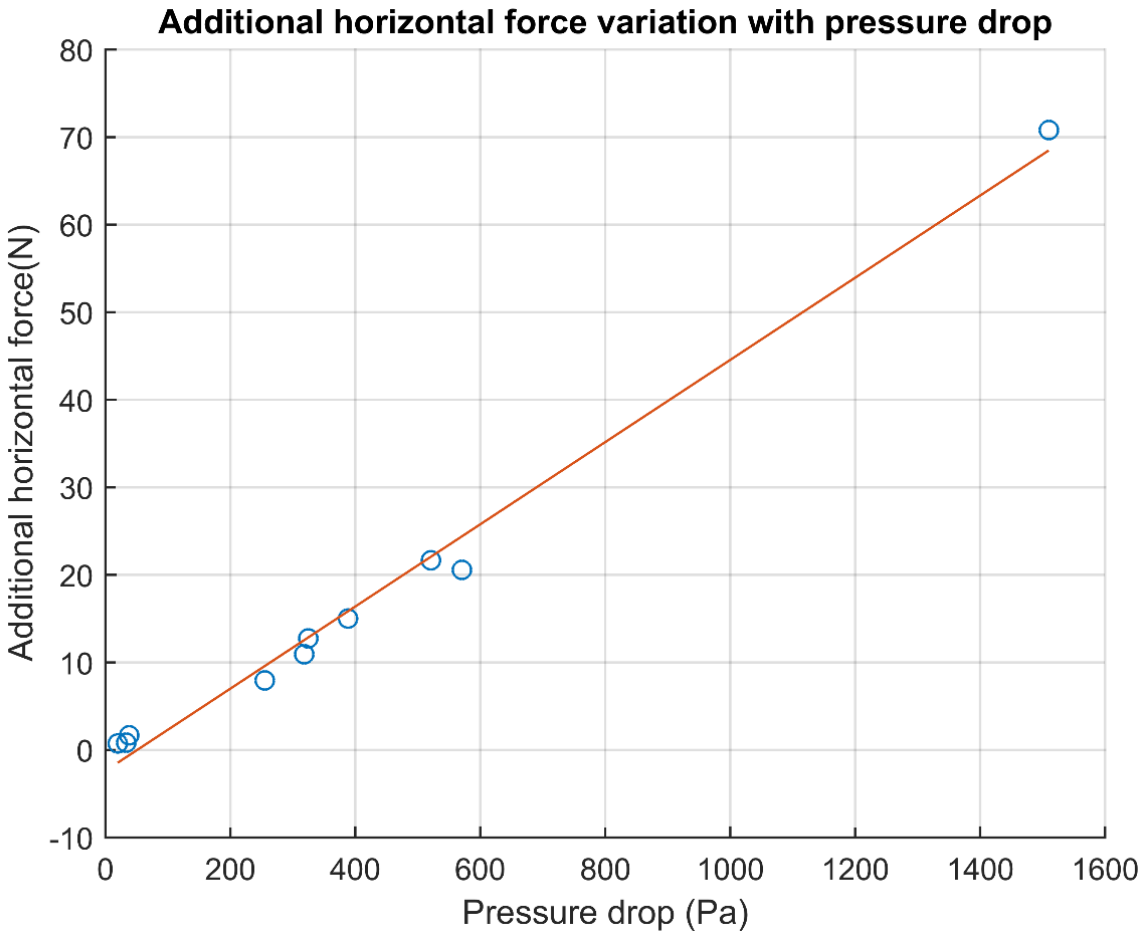

Figure 4.1: Additional horizontal force variation with pressure drop behind the nappe

In Figure 4.1, the best-fit curve is drawn between the values of pressure drop and additional horizontal force that were yielded from the physical model. As it is evident from Figure 4.1, the pressure drop behind the nappe is directly proportional to the additional horizontal force on the caisson.

4.2 Application of physical model results to the field scale

4.2.1 Direct scaling up

As the final objective of this study is to quantify the impact of this additional horizontal force in the context of a tsunami breakwater overtopping scenario, the scaling up needs to be considered. When Froude scaling is used, the pressure also scales up according to the geometric scale used. As the force is equals to pressure times the cross-sectional area, the scaled force in the field scenario is obtained by multiplying by a factor of geometric scale to the power three. The summary of scaled-up forces is presented in Table 4.2.

Table 4.2: Scaled-up parameters for field scale (The water levels, pressure values and forces are scaled up using factors of 150,150 and 150^3 respectively)

Test number	Upstream water level [m]	Tail water depth [m]	Hydrostatic force [kN]	ΔP [kPa]	ΔF [kN]
1	33.03	14.25	120293	48.69	53281
2	35.445	16.31	129267	78.19	83081
3	35.58	14.10	139890	58.25	62531
4	35.25	13.58	139518	38.27	37301
5	30.405	18.89	110691	4.96	4691
6	33.555	21.65	86118	2.94	2834
7	37.98	4.31	183626	226.47	248539
8	30.405	18.89	78712	5.72	6611
9	35.655	13.97	140993	85.63	85722
10	33.45	11.99	131945	47.69	50066

Based on Froude scaling, the relative proportion of ΔF to the total horizontal force (in field scenario) is same as in the physical model. From Table 4.2, it can be inferred that for respective flow rates and water levels, the given ΔF values can be expected.

4.2.2 Limitations related to scaling up

When scaling up a physical model to the field scale, a number of aspects need to be considered. There can be certain obvious differences present between the physical model and the field scenario. One such discrepancy would be the water level difference in the physical model and the Kamaishi case. Also, the presence of surface tension in the two cases might lead to inaccuracies as well. The effect of surface tension can be evaluated using the 'Weber' number introduced in equation 3.3.

The results for the two cases are summarized in Table 4.3.

Table 4.3 : Comparison of Weber number for the physical model of Test_10 and Kamaishi overtopping scenario (The limit for the Weber number to neglect the surface tension effects remains at 120 (Peakall & Warburton, 1996). For Weber number in physical model, average nappe thickness is used as the characteristic length)

Case	Weber number	Limit to neglect surface tension effects
Physical model	21.96	120
Kamaishi overtopping	25386	

Higher the Weber number, lower the effect of surface tension. Peakall & Warburton (1996) has estimated the critical value of Weber number above which the surface tension effects are insignificant to be 120. As it can be seen for the Kamaishi case, the surface tension can be neglected as the Weber number is way higher than the limit of 120. However, as suggested by the Weber number of 21.96, when scaling down from the actual field scenario to the physical model, the surface tension effects become dominant. Hence, this can be introduced as a limitation in scaling up the physical model results to the field scale. However, the degree of magnitude of the influence from surface tension is not analysed due to the lack of data available to compare the results with actual measurements in field scale.

The possible effect of surface tension also emphasizes the need for a numerical model as it facilitates direct scaling up.

5 CFD modelling using OpenFOAM

This chapter focuses on the validation of the OpenFOAM model using open channel flow and the simulation of physical model results using OpenFOAM. The purpose of using a numerical model such as OpenFOAM is stressed by indicating that it facilitates direct scaling up avoiding the complications witnessed in physical model scaling up. The validation of the simulation results are done under two criteria for both cases of open channel flow and physical model simulation. The limitations encountered during the simulation of physical model results including the instabilities, 3D phenomena and nappe behaviour are interpreted based on the simulation analysis.

5.1 Validation of InterFoam model for open channel flow

For any CFD simulation, it is imperative to validate the model beforehand to verify the simulation results. Therefore, in order to evaluate the validity of the OpenFOAM model, a simple open channel scenario is simulated and the results are analysed. The model is validated taking two criteria into account.

i. The horizontal velocities along vertical direction should follow a logarithmic profile.

ii. The slope of the free surface of open channel flow can be determined analytically based on the bed shear stress. This calculated value of free surface slope can be compared with the slope obtained from the model simulation results.

The simulation is run using the following model domain as shown in Figure 5.1 and the steady state results are obtained. For the simulation, smooth wall boundaries, k-epsilon turbulence model and an average grid size of 3mm are used. A constant Q of 1.43e-3 m^3/s is applied and the simulation is carried out until the water level does not vary anymore (steady state).

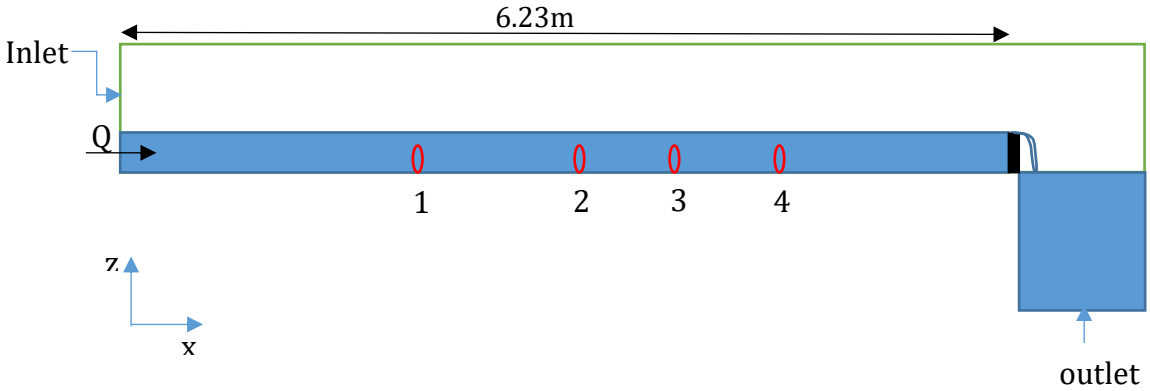

Figure 5.1 : Model domain for open channel flow (The positions 1, 2, 3 and 4 are located at distances of 2.5 m, 3.5m, 4m and 4.5m from the inlet respectively)

5.1.1 Checking for logarithmic profile

When validating the model for the logarithmic velocity profile, it is essential to consider both spatial and temporal variations. In order to account for temporal variations, the time averaged velocity values are used. The spatial variations are investigated by considering four different locations. Therefore, the vertical profile of the horizontal velocity (at steady state) is obtained at positions at 1, 2, 3 and 4 (See Figure 5.1) which are located at distances of 2.5 m, 3.5m, 4m and 4.5m from the inlet respectively.

When a turbulent boundary layer is developed, a logarithmic profile needs to be obtained for the horizontal velocities along the vertical direction. The grid size used in the OpenFOAM simulation is 3mm. The viscous sub-layer has a length scale of 'Kolgomorov' scale which is of very smaller magnitude than 3mm. Therefore, the viscous sub-layer is not resolved due to the insufficient grid resolution.

According to the 'Law of Wall' theory,

$$U_z = \frac{U_*}{\kappa} \ln \frac{z}{z_0} \tag{5.1}$$

Where U_z is the horizontal velocity (mms^{-1}), U_* is shear velocity (mms^{-1}), κ is Von-Karmen constant (=0.4), z is the vertical distance from bottom(mm) and z_0 is the roughness length(mm).

At z_0 (roughness length) is the distance from the wall boundary at which the idealized velocity given by the Law of Wall goes to zero. This z_0 is fundamentally a non-zero value as the laminar sub-layer does not follow turbulent velocity profile defined by the Law of Wall. By rearranging the equation (5.1) above gives,

$$\log z = \frac{\kappa}{U_*} U_z + \log z_0 \tag{5.2}$$

The velocities can be plotted on a semi-logarithmic scale where horizontal velocity (U_z) is on a linear axis and vertical distance from the bed (z) on a logarithmic axis. The least squares best-fit lines can be drawn as shown in Figure 5.2.

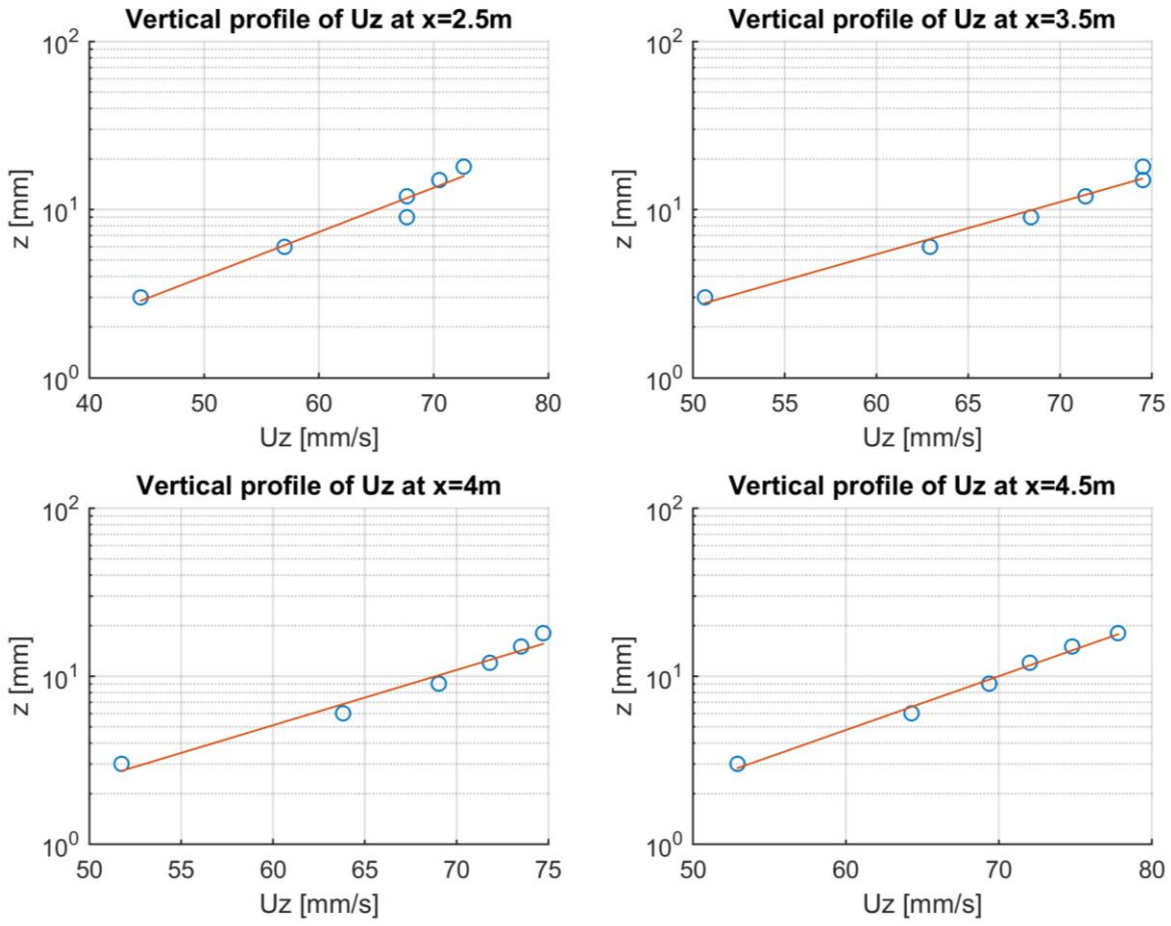

Figure 5.2 : Vertical profiles of horizontal velocities (time-averaged) at x=2.5m, 3.5m, 4m and 4.5m (x is measured from the inlet)

As it is evident from Figure 5.2, the gradual development of boundary layer is observed with the increasing distance from the inlet. In general, the development length of the

full boundary layer is 50 times the water depth in an open channel flow. Since the water depth at steady state in the above simulation is approximately 0.09m, this development length of boundary layer is at x=4.5m. A well-fitting logarithmic profile is obtained at x=4.5m verifying this fact.

As a whole, it is evident that the horizontal velocities follow a logarithmic profile validating OpenFOAM model for the open channel flow.

5.1.2 Determination of free surface slope

From the logarithmic velocity profiles, number of parameters such as shear velocity (U_*), bed roughness (z_0), bed shear stress (τ_b) and free-surface slope can be determined. The determination of these parameters are explained below.

Calculation of viscous sub-layer thickness (δ)

The viscous sub-layer thickness limit for *hydraulically smooth* conditions is given by,

$$viscous\ sub-layer\ thickness\ (\delta_{smooth}) = \frac{5 * \nu}{U_*} \tag{5.3}$$

(Uijttewaal, Turbulence in hydraulics CT5312: Lecture notes)

The viscous sub-layer thickness limit for *hydraulically rough* conditions is given by,

$$viscous\ sub-layer\ thickness\ (\delta_{rough}) = \frac{70 * \nu}{U_*} \tag{5.4}$$

(Uijttewaal, Turbulence in hydraulics CT5312: Lecture notes)

In order to determine the whether the wall is hydraulically smooth or rough, the viscous sub-layer thickness needs to be compared with roughness element height (k_s) which is equal to 30 times z_0.

The results are summarized in Table 5.1.

Table 5.1 : Summary of results of roughness lengths and viscous sub-layer thicknesses for simulation results obtained at x=2.5m, 3.5m, 4m and 4.5m

$x\ (m)$	$k_s\ (mm)$	δ_{smooth} (mm)	$\delta_{rough}(mm)$
2.5	2.76	0.33	4.62
3.5	2.22	0.39	5.43
4	1.62	0.41	5.77
4.5	0.17	0.39	5.46

For $x = 2.5\ m, 3.5m\ and\ 4m$,

$$\delta_{smooth} < k_s < \delta_{rough}$$

Hence, it can be established that the channel bed is *hydraulically intermediate* in terms of roughness.

For x=4.5m,

$$\delta_{smooth} > k_s$$

Thus, when the boundary layer is fully developed, the channel bed act as a *hydraulically smooth* bed. This factor suggests that the model fulfils the initially set boundary condition of hydraulically smooth channel bed.

Calculation of bed shear stress (τ_b)

Bed shear stress (τ_b) is given by,

$$\tau_b = \rho(U_*)^2 \tag{5.5}$$

The free-surface slope can determined from the analytical method (theory) and from the OpenFOAM model results. A comparison of results are performed later.

I. Analytical method

In order to calculate the free surface slope of the open channel flow, the following relationship between the shear stress and the pressure can be established.

$$\tau = \rho g h \frac{d\eta}{dx} \tag{5.6}$$

Where τ is the shear stress, h is the water depth, η is the water surface elevation and x is the horizontal coordinate.

As $= \tau_b$, the free surface slope is given by,

$$\frac{d\eta}{dx} = \frac{\tau_b}{h\rho g} \tag{5.8}$$

II. From OpenFOAM model results

In order to find the free surface angle, it is required to find the free surface position at different x (horizontal distance) values. Based on the nature of the VOF method used in OpenFOAM, the interface is not generally sharply defined, but rather arises as a result of the input phase fraction field (Greenshields, 2016). Therefore, in order to find the air-water interface at required locations, the phase fraction (α) computed for each cell near the interface is used.

The alpha (α) values obtained after the steady state are used for this purpose. Firstly, the time-average α values (from 80s to 90s with 0.1 seconds time step) at different z values are obtained. The interface is assumed to be at α =0.8 line. In order to consider spatial variations, several locations (x=2.5 m, 3.5m, 4m and 4.5m) along the flume bottom are taken into account.

The results are summarized in Table 5.2.

Table 5.2 : Comparison of analytical and model results for free-surface slope (slope is given in radians)

x(m)	τ_b (Pa)	Analytical free-surface slope [radians]	Model free-surface slope [radians]	Difference (%)
2.5	0.23	2.50 E-4	8.07 E-4	68.98
3.5	0.17	1.81 E-4	5.70 E-4	68.35
4	0.15	1.61 E-4	2.36 E-4	31.72
4.5	0.16	1.70 E-4	1.74 E-4	2.62

The comparison between the analytically calculated free-surface angle and the model free-surface slope shows a decreasing error percentage along the flume. When x=4.5m, two values for free-surface slope are almost in agreement with each other, implying that the boundary layer is fully developed near the region of x=4.5m. When the boundary layer is fully developed the, pressure gradient is essentially balanced by the shear stress. This fact is proved by the results obtained in Table 5.2.

Also, it is important to understand the reasons for the difference in compared values. One important factor is taking interface to lie at the phase fraction (α)=0.8 line. In addition, assuming an average bed shear stress value (τ_b) for the considered horizontal stretch also contains some error.

5.2 Simulation of caisson overflowing experiment using OpenFOAM

Due to the existing limitations that are encountered in scaling up the physical models to the field scale, the effectiveness of the numerical models can be highlighted. As the main attention of this study is focussed on the nappe's trajectory, in OpenFOAM simulation it is very important to get the turbulence at the air-water interface correct. This will help in getting the accurate nappe trajectory which leads to the proper estimation of the additional horizontal force on the caisson. In fact, many previous studies have done OpenFOAM simulations on breakwater overtopping as described in Chapter 2.

As part of this study, a CFD simulation of the physical model is run using OpenFOAM. Test_10 is selected and used for the simulation throughout this analysis.

5.2.1 Model set-up

The standard k-ε turbulence model in InterFOAM is used for simulation. The governing equations are the Navier-Stokes equations for continuity and momentum conservation as shown in equations (5.9) and (5.10).

Mass conservation (Continuity)

$$\frac{\partial \rho}{\partial t} + \nabla(\rho U) = 0 \qquad (5.9)$$

Momentum conservation

$$\frac{\partial U}{\partial t} + \nabla.(UU) = -\frac{1}{\rho}.\nabla P + \vartheta\nabla^2.U + K \tag{5.10}$$

Where ρ is the density, ϑ is the kinematic viscosity and K is the source. Under the assumption of incompressible fluids, equation (5.9) can be re-written as,

$$\nabla.U = 0 \tag{5.11}$$

Equation (5.10) can be re-written as,

$$\frac{\partial \rho U}{\partial t} + \nabla.(\rho UU) = -\nabla P + \eta_0\nabla^2.U + K \tag{5.12}$$

Where η_0 is the dynamic viscosity . In equation (5.12), $\nabla.(\rho UU)$ is the convective term while $(-\nabla P + \eta\nabla^2.U)$ forms the diffusive part.

These VOF-based Navier-Stokes models can be introduced as useful tools for numerical predictions for physical models related to wave interactions with coastal structures (Vanneste & Troch, 2015).

InterFoam Volume of Fluid (VOF) method

In order to model the air-water interface of the overflow nappe, InterFoam will be utilized. The Volume of Fluid (VOF) method facilitates the two-phase algorithm in InterFoam in which a specific equation is used to determine the volume fraction of each phase (i.e air or water fraction in this case) (Greenshields, 2016). This phase fraction, α is computed for each computational cell in the model(Greenshields, 2016).

The scalar function α can be computed from a separate transport equation that takes the form of,

$$\frac{\partial \alpha}{\partial t} + \nabla.(\alpha U) = 0 \tag{5.13}$$

In OpenFOAM, the required compression of the surface is obtained by an additional compression term into the VOF equation (5.13) as shown in equation (5.14).

$$\frac{\partial \alpha}{\partial t} + \nabla.(\alpha U) + \nabla.(\alpha(1-\alpha)U_r) = 0 \tag{5.14}$$

Where U_r is a velocity field suitable to compress the interface.

The physical properties are basically determined as weighted averages based on this volume fraction (Greenshields, 2016). For an instance, the density (ρ') for each cell is calculated using the phase fraction (α) assigned to that cell as show in equation (5.15).

$$\rho' = \alpha\rho + (1-\alpha)\rho_{air} \tag{5.15}$$

Based on the nature of the VOF method the interface is not generally sharply defined, but rather arises as a result of the input phase fraction field. (Greenshields, 2016)

OpenFOAM uses a tracking approach to determine the free surface instead of reconstructing the free surface in each successive time step which helps to reduce the computational cost (Higuera et al., 2014). Hence, it does not require to input a pressure

boundary condition on the free surface, but tends to diffuse the interface over some cells (Higuera et al., 2014).

5.2.2 Description of the model runs

The model domain and the boundary conditions are set-up to reproduce the same experimental conditions(eg : smooth wall boundaries) that were prevailed. The model domain is depicted in Figure 5.3 below.

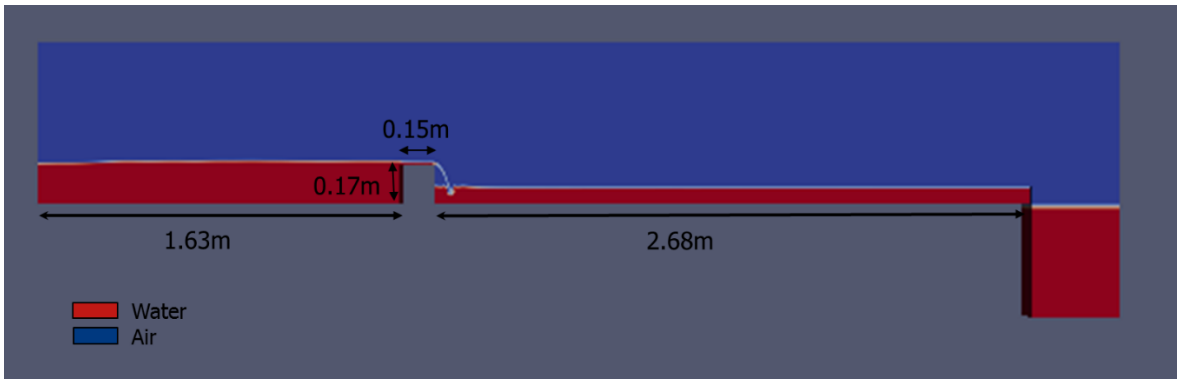

Figure 5.3 : Model domain used in OpenFOAM simulation of the physical model (the water is shown in red and the air is shown in blue)

More attention is focused on modelling the simulation run with the same experimental conditions. At the furthermost downstream end of the model domain, a sharp-crested weir is modelled allowing a free overflow. A detailed description of the input structure and boundary conditions used in OpenFOAM simulation is included in Appendix I.

5.2.3 Results and analysis

The caisson overflowing situation is a complex process for simulation consisting a number of sub-processes such as air entrainment, flow over the caisson being moving from sub-critical to super-critical region, formation of air-water interface on either side of the overflow jet, pressure drop behind the nappe, and the resultant water level increase behind the nappe. Therefore, it is more effective to consider each of these sub-processes separately and ensure they are simulated properly.

5.2.3.1 Validation of the OpenFOAM simulation of the physical model results

The validity of the CFD simulation is done under two criteria. For both the criteria, the steady state results are considered.

1. The free-surface on top of the caisson: In the physical model, the flow regime changes from sub-critical to super-critical as described in section 3.1.5. This transition leads to smooth change of free-surface on top of the caisson and the critical depth occurs on top of the caisson.

2. Air phase fraction behind the overflow nappe: As both the physical model and CFD model deals with two phases, for a selected domain area, the fraction of air can be compared between the physical model and the CFD model.

1.The free-surface on top of the caisson

The free-surface over the caisson that is modelled can be compared against the experimental results (for steady state). This is illustrated in Figure 5.4 below.

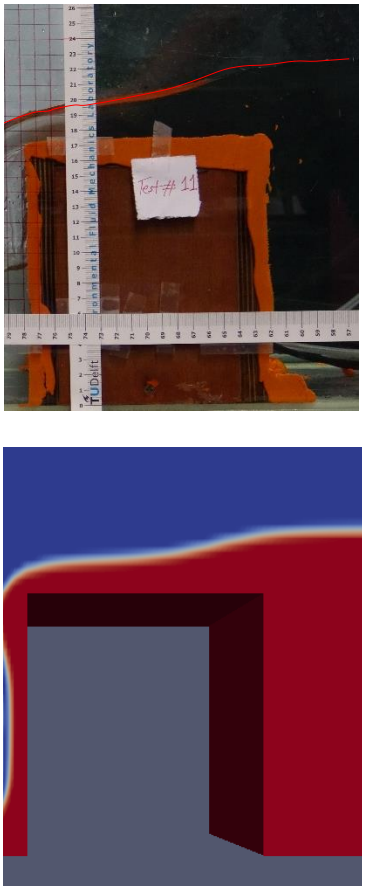

Figure 5.4 : Visual comparison of the free-surface over the caisson between the physical model and OpenFOAM simulation

In addition, the comparison for the validation of the simulation results can be done quantitatively as shown in Table 5.3.

Table 5.3: Comparison of experiment results with model results with respect to the free-surface on top of the caisson

Parameter	Laboratory experiment	OpenFOAM simulation	% Error
Water level above upstream end of caisson	0.048m	0.0456m	5.0
Water level above downstream end of caisson	0.020m	0.021m	5.0
Distance from upstream end to the point of critical depth ($d_{critcal}$=0.0252m)	0.103m	0.106m	2.9

The comparison on Table 5.3 suggests that the OpenFOAM model has effectively simulated the free-surface over the caisson during the steady state. The error percentages of the free-surface elevations can be attributed to the fact that certain boundary layer characteristics are not properly resolved due to the insufficient grid spacing of the model domain. For instance, the viscous sub-layer is not resolved in the simulation as the grid resolution used in the model (3mm) is inadequate.

2.Air phase fraction behind the overflow nappe

One of the main attributes of the study is the nappe behaviour during the caisson overflowing. Thus, the CFD model can be validated based on the area of the void of air behind the nappe. For this, a particular area of the domain is selected and the air fraction is compared for a specific time period after the steady state is achieved.

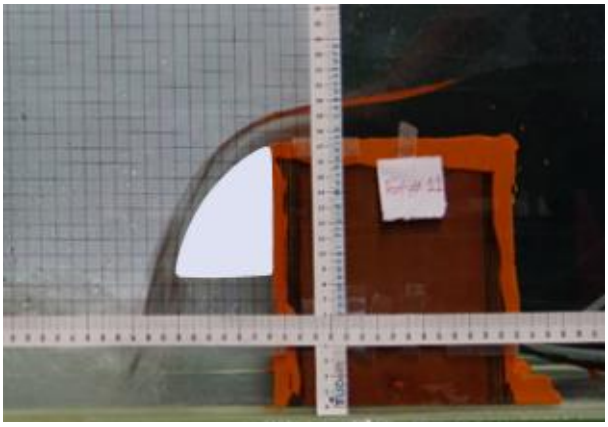

Figure 5.5 : Area behind the nappe which is 100% air during the laboratory experiment (The white area of 23.6 cm^2 is always filled with air during the non-aerated nappe)

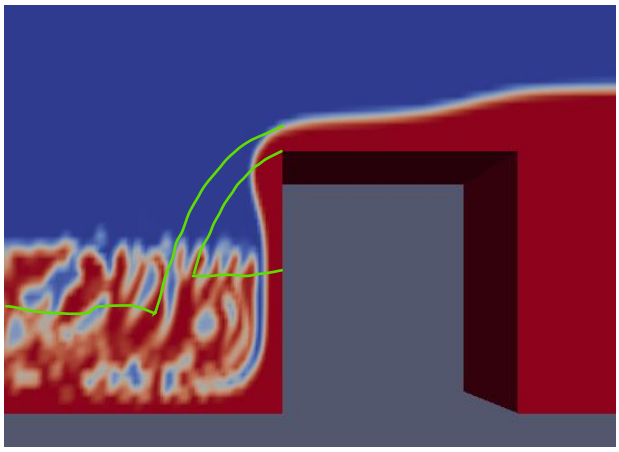

Figure 5.6: OpenFOAM simulation nappe behavior (The green lines indicate both the upper and lower nappe envelopes during the laboratory experiment)

For the physical model, the time-averaged area of the air void behind the nappe is 23.6 cm^2. This air fraction within this area can be compared between the physical model and the OpenFOAM model. In the physical model this area is 100% filled with air whereas in the OpenFOAM model only 50%(11.8 cm^2) is filled with air. However, in the simulation no air is behind the nappe.

The overflow nappe behaviour is not correctly simulated in OpenFOAM as depicted in Figure 5.6. The major disparity is that the model simulates the nappe as a 'clinging nappe' whereas the actual nappe behaviour is a 'depressed nappe' having air behind the nappe. This can be attributed to be several reasons which are discussed below in detail.

Firstly, the simulation being run as a 2D case might have contributed to the number of inadequacies in correctly simulating the experimental conditions. After the nappe clings on to the caisson surface there is no way for the air to get back into the space behind the nappe as the model is run as a 2D case. A 3D simulation provides more opportunities for instabilities in the nappe which can act as pathways for air to get in. Therefore, modelling the physical model as a 3D case is promising.

Furthermore, using Large Eddy Simulation(LES) instead of k-epsilon enables turbulent fluctuations to be resolved. Hence, it can contribute to formation of instabilities in and under the nappe, which could allow air in. In LES, it is necessary to model as a 3D case so that the turbulence cascade can be obtained correctly. This is due to the fact that, in three-dimensional LES models, the turbulence starts at larger scale and large vortices loose their energy to smaller vortices and eventually the energy will be lost through viscosity.

In general, a fully turbulent flow exhibits a wide range of spatial and temporal scales. Another limitation related to simulation of turbulent flows is that the practical inadequacy of CFD models to resolve smaller spatial scales like Kolmogorov scales due to high computational cost.

6 Conclusions

This chapter focuses on the research questions.

A. What is the relative magnitude of the additional horizontal force (ΔF) when compared to the total horizontal force? Is the magnitude significant enough to impose considerable impact on the stability of the breakwater?

Quantitatively, this additional horizontal force acting on the caisson is of considerable magnitude compared to the total horizontal force according to the results obtained for Kamaishi breakwater scenario that is analysed by Bricker et al(2013). According to Bricker et al(2013), this additional horizontal force contributes to 14%-19% of the total horizontal force acted on Kamaishi breakwater during the Great East Japan tsunami.

In the physical model (scale of 1:150) conducted in the Water Lab, this additional horizontal force is calculated to be in the range of 15%-30% of the total horizontal force acting on the caisson. This is closer to the results obtained for Kamaishi case.

Therefore, the experimental results are in agreement with the field results which validates the physical model used in terms of force proportioning. Furthermore, these results imply that the additional horizontal force due to non-aeration of the overflow jet is significant in terms of stability of a caisson breakwater during a tsunami overtopping scenario.

B. What is the extent of applicability of the small-scale physical model results (eg : forces, flow characteristics) to the reality?

The additional horizontal forces calculated for the physical model (Table 4.1)can be directly scaled up using a factor of the geometric scale to the third power according to the Froude scaling. The scaled up additional horizontal forces (Table 4.2) are of same proportion to their corresponding hydrostatic components as in the physical model. It can be expected that the additional horizontal forces will be in the order of magnitudes shown in Table 4.2 for the corresponding water levels and flows values during a tsunami.

The scaling up effect on the flow characteristics can be attributed to the similarities and disparities with regards to Re, Fr and We numbers. There is a large disparity in Re numbers for the two cases. This factor suggests the difference in inertia forces for the two cases relative to the similar viscous forces. However, in both cases the flow is fully turbulent indicating a similarity in flow behaviour. The Fr numbers are in agreement for both cases. Therefore, in both cases, the caisson is expected to behave as a perfectly operating broad-crested weir (The critical depth occurs on top of the caisson). During the tsunami overtopping the inertia forces are quite large leading a smaller We number. Hence, it can be inferred that the surface tension effects for field scale is negligible unlike in the scaled-down physical model where the surface tension plays a vital role in the overflow jet behaviour.

C. What is the validity of the ballistic model (theoretical) in deriving the overflow nappe's trajectory for the aerated and non-aerated cases? What conclusive remarks can be made on the physical processes involved?

The aerated nappe can be derived using the general projectile motion theory as suggested by the comparatively low root mean square error(RMSE) of 0.19cm. The non-aerated nappe is not satisfactorily derived from theory as suggested by the RMSE value of 0.51cm. In relation to non-aerated nappe, the contributing factors for the relatively high error are identified. The pressure drop (ΔP) behind the nappe is identified as the most influential factor. Based on the sensitivity analysis on the pressure drop, it was found a 33% reduced pressure drop yields a better-fitting nappe with a reduced RMSE of 0.15cm. These results lead to the conclusion that the ΔP might be time-varying parameter. The magnitude of ΔP is dependent upon the likelihood of aeration from outside in addition to the air entrainment from the cavity.

Secondly, the effect of surface tension on the nappe trajectory is analysed. The theoretical nappe trajectory derivation does not include surface tension. The surface tension tends to depress the nappe, and higher the radius of curvature lower the effects from surface tension. When analysing the results, it can be concluded that the influence of ΔP is more pronounced than that of surface tension.

The governing physical processes related to caisson breakwater overflowing are analysed. The flow conditions below the overflow nappe are hydrostatic, which is implied by a time-averaged stationary water level below the nappe. The dynamic pressure arising from the stagnation pressure at the jet impingement on the flume bed is estimated and is compared with the pressure drop behind the nappe. The results suggest the above-mentioned dynamic pressure is negligible with respect to the pressure drop. Thus, it is concluded that the governing mechanism responsible for the pressure reduction is the air entrainment process during jet impingement. The air entrainment rate from the cavity behind the nappe is compared against the impinging velocity of the overflow jet. The results suggest that air entrainment rate increases with increasing jet impingement velocity, establishing the fact that higher inertia forces leads to rapid air entrainment.

D. How to estimate the additional horizontal force on the caisson breakwater when the nappe's trajectory is established during tsunami?

The answer to particular question is based on the relationship between kinematics (ballistics) and dynamics (forces). During a tsunami or in any other breakwater overtopping scenario, it is impossible to measure the pressure drop behind the nappe (ΔP). However, by setting a video camera the overflow jet can be recorded and based on that, the overflow nappe's trajectory can be developed. The following parameters are required in developing the nappe's trajectory.

I. The drop length of overflow jet (L_d)
II. The nappe thickness (d)
III. An average flow rate over the caisson (Q)

With the development of the nappe trajectory, it is possible to determine the pressure drop behind the nappe by back calculating the values. With the derived pressure drop (ΔP), the additional horizontal force that is acting on the caisson (ΔF) can be calculated.

For this purpose, the Figure 6.1 can be used. Figure 6.1 is obtained by scaling up each experimental run values of ΔP and ΔF. According to Froude number criteria, ΔP is scaled up to the field scale using a factor of 150(=geometric scale). The ΔF is scaled up to the field scale using a factor of 150^3(=geometric scale^3).

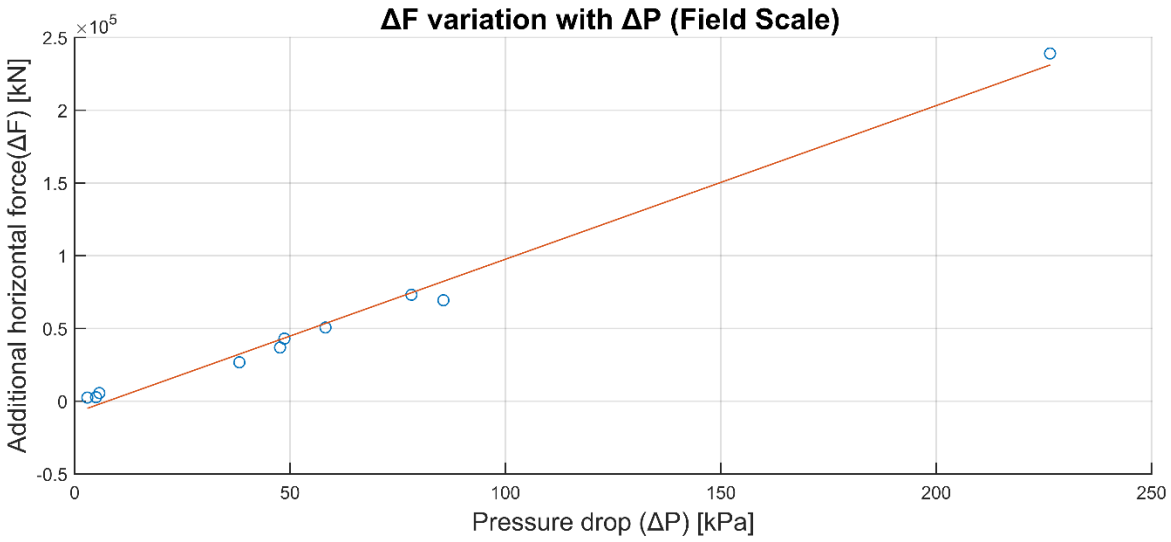

Figure 6.1 : Additional horizontal force (ΔF) variation with pressure drop (ΔP) (The points represent the scaled-up values for each experimental run and best fit curve is from least square criterion)

Figure 6.1 yields the relationship of; $\Delta F = 1056(\Delta P) - 8034$ with a R^2 value of 0.9898. It should be noted that this relationship is not generic but only valid for the limited set of physical model runs conducted. However, it provides an implication on the additional force (ΔF) for a given ΔP value. Thus, it is evident that an explicit relationship can be developed between kinematics(ballistics) and dynamics(forces).

E. What conclusions can be drawn regarding the simulation of the physical model results of a breakwater overtopping using OpenFOAM including all the physical processes involved?

As surface tension effects may affect the direct scaling up of model tests to field scale, the requirement of numerical model simulations can be highlighted. In OpenFOAM, the k-epsilon turbulence model with the InterFoam solver is used for this purpose. Prior to investigating the validity of OpenFOAM to simulate the caisson overflowing scenario, the model is validated for open channel flow. The results suggest that OpenFOAM correctly simulates the open channel flow with respect to the logarithmic profile and the free-surface slope.

OpenFOAM simulation of the caisson overflowing provides matching free-surface on top of the caisson with maximum of 5% error. The overflow nappe is not correctly simulated as observed in the laboratory experiment. It is simulated as a clinging nappe instead of a detached one, as the 2D model does not allow air to get into the cavity behind the

nappe. The evident inaccuracies of the overflow nappe simulation can be attributed to the overestimated momentum exchange at the air-water interface of the nappe as speculated by Bricker et al, (2013). As a solution, recommended solution with a mechanism facilitating air insertion into the void is recommended in Chapter 6.

In addition, using Large Eddy Simulation (LES) model in 3D form can be promising, as it can contribute to the formation of instabilities in and under the nappe, which could allow air into the cavity.

F. What is the role of the nappe's behaviour during a tsunami overtopping? What are the relevant factors that need to be considered when comparing it with the nappe behaviour in the physical model?

This question stresses the applicability of this study. The overflow nappe goes through different stages during a steady overflow of a caisson breakwater. When the nappe moves from a clinging nappe to a free nappe due to the pulling away of the nappe, the radius of curvature of the nappe increases and the curvature decreases. With time it becomes a depressed nappe increasing the curvature of the nappe. A depressed nappe is formed by the pressure reduction that occurs behind the nappe due to the air entrainment in the mixing layer of the nappe. The pressure reduction results in a pressure difference across the caisson in addition to the hydrostatic pressure. This additional pressure difference leads to an additional force component affecting the stability of the caisson breakwater.

High energy waves are associated with tsunami conditions and the overtopping of a caisson breakwater during a tsunami will result in accelerated flows with detached nappes. During a tsunami, due to the very high heads and lack of ventilation a 'drowned' nappe (Figure 2.1) can be developed. However, for the physical model conducted, such massive heads are not witnessed, leading to transition of nappes from 'clinging' to 'free'(aerated) and ultimately to a 'depressed'(non-aerated) nappe. Hence, these factors need to be considered in comparing the physical model behaviour to the tsunami situations.

7 Recommendations

In this study, analytical model solutions (in the form of a ballistic model) and a CFD model (using OpenFOAM) have been used to correctly reproduce the results gained from the physical model. In addition, the understanding of the governing physical processes is incorporated to interpret the results of physical model results.

Only a limited set of data is analysed using the ballistic model. Therefore, more in-depth analysis incorporating surface tension effects and other overflow parameters can be recommended. Also, a detailed analysis on the estimation of relevant parameters that drives the recirculation, water depth rising below the nappe and pressure drop can be recommended. As the maximum air entrainment occurs at the jet impinging point into the pool of water which primarily affect the pressure drop (ΔP), it can be recommended to look more into the dynamics of jet impinging and resulting air entrainment.

The OpenFOAM simulations are not reasonably reproducing the correct physical processes that were observed from the laboratory experiment. Number of reasons could be identified for this inability of OpenFOAM to simulate the results accurately.

The majority of numerical simulations are modelled as 2D simulations due to the computational cost. As discussed in Section 5.2, this might have contributed to erroneous results as there might be no possible opportunities to develop instabilities in the nappe, preventing the air to get back. An alternative mechanism to facilitate air supplement using 'atmosphere' boundary condition is depicted in Figure 7.1. The 'atmosphere' boundary in InterFoam allow free air movement into the area.

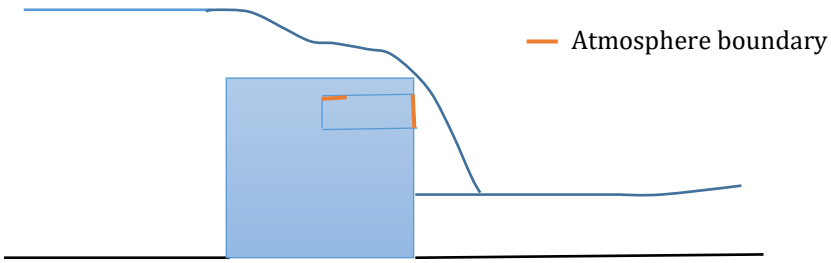

Figure 7.1 : Addition of atmosphere boundaies to allow air into the void behind the nappe

Furthermore, it can be recommended to re-do the OpenFOAM simulation of the experiment as 3D LES model using a finer grid size for the reasons discussed in part 2 of section 5.2.3.1. The turbulent model used (k-epsilon) might not correctly model the turbulent charracteristics at the air-water interface. For an instance, the turbulent diffusivity might not be simulated at the interface. Further, the modelling of the surface tension in the model equations need to be analysed. So it can be recommended to study other factors that leads to instabilities and modify the k-epsilon model to ensure correct turbulent characteristics.OpenFOAM does not correctly simulate small air bubbles which can be a contributing factor for the wrong simulation results. Hence, it can be recommended to investigate on that issue to achieve correct behaviour/movement of the air bubbles under the overflow nappe.

References

Abdalla, M. G., & Shamaa, M. T. (2016). Experimental Investigations of Nappe Profile and Pool Depth for Broad Crested Weirs, *4*(1), 593–610.

Arikawa, T., Sato, M., Shimosako, K., Tomita, T., Tatsumi, D., Yeom, G. S., & Takahashi, K. (2012). Investigation of the failure mechanism of Kamaishi breakwaters due to tsunami, Initial report focusing on hydraulic characteristics. *Technical Note of the Port and Airport Research Institute*, *1251*, 2012.

Bricker, J. D.,Takagi H.,Mitsui J. (2013). Turbulence Model Effects on VOF Analysis of Breakwater Overtopping during the 2011 Great East Japan Tsunami. *35th IAHR World Congress*, 10.

Chanson, H., ENSHMG M.E. (1994). Hydraulics of Nappe Flow Regime Above Stepped Chutes and Spillways. *Australian Civil Engineering Transactions*, *36*, 69–76.

Chow, V. Te. (1959). *Open-Channel Hydraulics*. The Estate of Ven Te Chow.

Fischer, H. B., List, E. J., Koh, R. C. Y., Imberger, J., & Brooks, N. H. (1979). *Mixing in Inland and Coastal Waters*. Academic Press, Inc (London) Ltd.

Gonzalez, C. A., & Chanson, H. (2007). Experimental measurements of velocity and pressure distributions on a large broad-crested weir. *Flow Measurement and Instrumentation*, *18*(3–4), 107–113. https://doi.org/10.1016/j.flowmeasinst.2007.05.005

Greenshields, C. J. (2016). OpenFOAM, (June).

Higuera, P., Lara, J. L., & Losada, I. J. (2014). Three-dimensional interaction of waves and porous coastal structures using OpenFOAM??. Part I: Formulation and validation. *Coastal Engineering*, *83*, 243–258. https://doi.org/10.1016/j.coastaleng.2013.08.010

Hong, Y.-M., Huang, H.-S., & Wan, S. (2010). Drop characteristics of free-falling nappe for aerated straight-drop spillway. *Journal of Hydraulic Research*, *48*(1), 125–129. https://doi.org/10.1080/00221680903568683

Hydraulics, O. C. (2000). CIVE2400 Fluid Mechanics Section 2 : Open Channel Hydraulics, 1–39.

Lalli, F., Bruschi, A., Lama, R., Liberti, L., Mandrone, S., & Pesarino, V. (2010). Coanda effect in coastal flows. *Coastal Engineering*, *57*(3), 278–289. https://doi.org/10.1016/j.coastaleng.2009.10.015

Lara, J. L., Higuera, P., Maza, M., del Jesus, M., Losada, I. J., & Barajas, G. (2012). Forces induced on a vertical breakwater by incident oblique waves. *International Conference on Coastal Engineering*, 1–10.

Mitsui, J., Matsumoto, A., Hanzawa, M., & Nadaoka, K. (2016). Estimation Method of Armor Stability Against Tsunami Overtopping Caisson Breakwater Based on Overflow Depth. *Coastal Engineering Journal*. https://doi.org/10.1142/S0578563416400192

Nakayama, A., Yokojima, S. (2003). Modeling free-surface fluctuation effects for

calculation of turbulent open-channel flows. *Environmental Fluid Mechanics. 3*, *3*, 1–21.

Peakall, J., & Warburton, J. (1996). Surface tension in small hydraulic river models-the significance of the Weber number. *Journal of Hydrology New Zealand*, *35*, 199–212.

Pringle, W. J., Yoneyama, N., & Mori, N. (2011). Multiscale Coupled Three-dimensional Numerical Analysis of the 2011 Tohoku-oki Earthquake Tsunami around the Kamaishi Bay Offshore Breakwater (Submitted to journal Coastal Engineering).

Sarginson, E. J. (2017). The influence of surface tension on weir flow, *1686*(June). https://doi.org/10.1080/00221687209500034

Suppasri, A., Shuto, N., Imamura, F., Koshimura, S., Mas, E., & Yalciner, A. C. (2013). Lessons Learned from the 2011 Great East Japan Tsunami: Performance of Tsunami Countermeasures, Coastal Buildings, and Tsunami Evacuation in Japan. *Pure and Applied Geophysics*, *170*(6–8), 993–1018. https://doi.org/10.1007/s00024-012-0511-7

Tanimoto, K., & Takahashi, S. (1994). Design and construction of caisson breakwaters — the Japanese experience. *Coastal Engineering*, *22*(1), 57–77. https://doi.org/http://dx.doi.org/10.1016/0378-3839(94)90048-5

TOMITA, T., YEOM, G.-S., AYUGAI, M., & NIWA, T. (2012). Breakwater Effects on Tsunami Inundation Reduction in the 2011 off the Pacific Coast of Tohoku Earthquake. *Journal of Japan Society of Civil Engineers, Ser. B 2(Coastal Engineering)*, *68*(2).

Uijttewaal, W. (n.d.). *Turbulence in hydraulics CT5312 (Lecture Notes)*.

Vanneste, D., & Troch, P. (2015). 2D numerical simulation of large-scale physical model tests of wave interaction with a rubble-mound breakwater. *Coastal Engineering*, *103*, 22–41. https://doi.org/10.1016/j.coastaleng.2015.05.008

APPENDIX

A Dimensions of caisson used in the physical model

Table A.1 : Dimensions associated with the laboratory experiment

Dimension of caisson	Actual	Model
Height	26 m	0.173 m
Length	23 m	0.153 m
Width	30 m	0.2 m (fixed)
Flume Dimensions		
Height	0.37 m	
Length	4.5 m	
Width	0.2 m	

*Geometric scale used = 1 : 150

B Determination of parameters related to scaling

In order to find Reynolds number, Froude number and Weber number as summarized in section 3.1.2.1 the following values are used for the two cases of Kamaishi breakwater overtopping during the tsunami and the physical model of caisson overflowing.

For Kamaishi overtopping: Q=40.8m^3/s and water depth(L)=7m (The highest water level above the caisson is found to be 7m)

For physical model overflowing of caisson: Considering the upstream end of the caisson, Q=0.003m^3/s, U=0.5m/s and a water depth(L)=0.03m

For both the cases, a surface tension (water-air) value of 72.86mNm^{-1} is used.

C Calculation of flow rates

Once the flow becomes steady and the flow rate is calculated based on the flow over a sharp-crested weir at the downstream end of the flume as shown in Figure 3.2. The calculation of the inflow rate (Q) using the Volgens (Rehbock stuw) weir equation as follows;

$$de = do + 0.0012 \quad \text{(C.1)}$$

$$Ce = 0.602 + 0.083 * do/Hc \quad \text{(C.2)}$$

$$Q = 1000Ce\frac{2}{3}\sqrt{2g}Bde^{1.5} \quad \text{(C.3)}$$

Where; d_o is overflow depth (m), Hc is weir height (m),B is width of flume (m),Q is inflow rate (litre/s)

D Influence of 'Coanda' effect

In a clinging nappe, the 'coanda' effect comes into play. Due to the low momentum of the inflow in Test_8 (Q=1.22 litre/sec and tail water depth=12.59 cm), a clear overflow jet was not observed even after the steady state is achieved as shown in Figure D.1.

A. 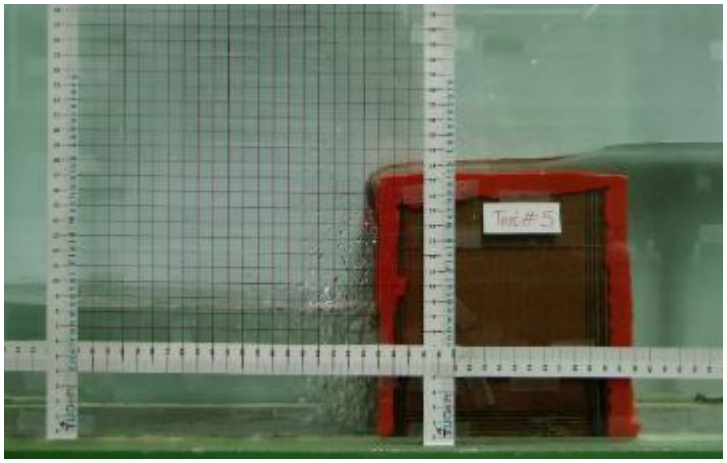

Figure D.1 : Overflow jet along the caisson surface in Test run 5 after achieving the steady state

This particular behaviour was also observed during the initial stage of some of the experimental runs where the momentum of the oncoming flow is not high enough to push it further away from the downstream end of the caisson. This can be attributed to the phenomenon of 'Coanda' effect. Coanda effect can be generally described as the tendency of a fluid jet to adhere to closeby solid surfaces. Most notably, Coanda effect takes place as a moving stream of fluid when in contact with a curved surface tends to follow the curvature of the curved surface.

However, the caisson crest end in the experimental set-up is not exactly a curved surface but a sharp-edged end so that the influence of the Coanda effect is relatively less. This is further illustrated by Figure D.2.

B.

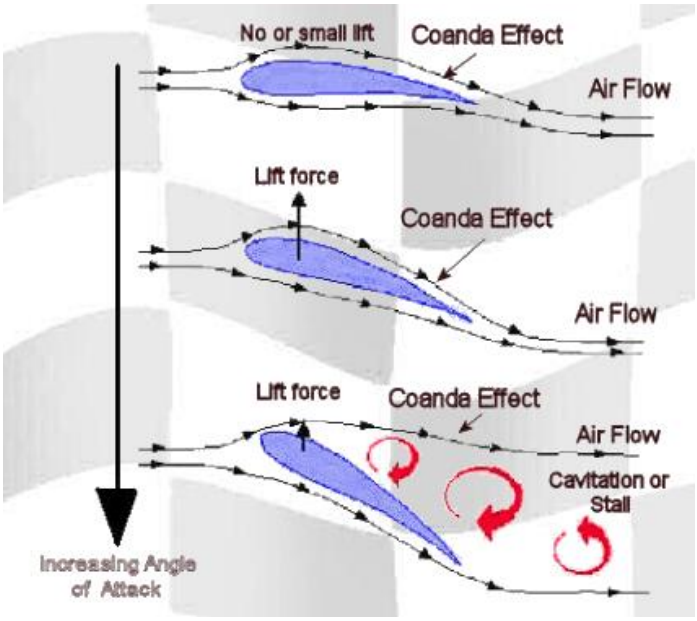

Figure D.2 : Influence of Coanda effect depending on the angle of attack (Coanda effect.html)

Figure D.2 indicates how the Coanda effect is affected during an air flow over the wing when the angle of interaction between fluid flow and the solid wing varies. When the angle of attack is too high, the fluid flow is only marginally following the curved surface as shown in the bottom of Figure D.2. In the case of the lab experiment, the angle of attack is closer to 90^0, so that the influence of the Coanda effect will be less. However, when the flow speed is very low, it might contribute to a more pronounced Coanda effect.

E Description of the pressure sensors used

The pressure sensors used in the experiment are 'differential' pressure sensors which provide the difference of two independent pressure sources. For the experiment conducted one end is always opened to atmosphere. Hence the subsequent output pressure readings are measured relative to the atmospheric pressure.

The differential pressure sensor used is depicted in Figure E.0.1 below. The underlying principle of the pressure sensor is explained below using Figure E.0.2.

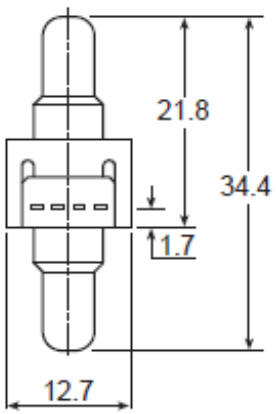

Figure E.0.1 : Differential pressure sensor (dimensions in mm) [Honeywell pressure sensors brochuer]

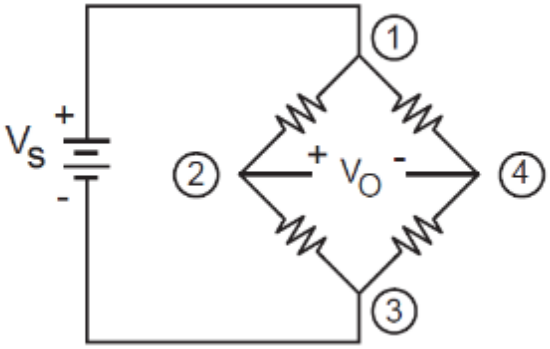

Figure E.0.2 : Underlying principle of the pressure sensor based on resistivity [Honeywell pressure sensors brochuer]

A schematic diagram of the arrangement of resistors used within the pressure sensor is illustrated in Figure E.0.2. The two opposing ports are connected to two pressures separately (one at the place where pressure need to be measured and the other to the atmosphere). Based on the exposed pressures the resistance at points 2 and 4 varies and hence the difference of pressures is proportional to the difference of resistance. A voltage value is given as the output depending on the resulting resistance.

F Calibration of pressure sensors

A pressure sensor can be introduced as a device that modifies a pressure signal into an electrical signal. Therefore, the measured electrical signals are only useful only if they correctly represent the corresponding pressure signal experienced by the pressure sensor. In order to develop this relationship, the process of 'calibration' is used by which the electrical signal is modified accordingly so that the applied pressure can be calculated.

A schematic diagram of the calibration set-up for the pressure sensor is shown in Figure F.0.1 below.

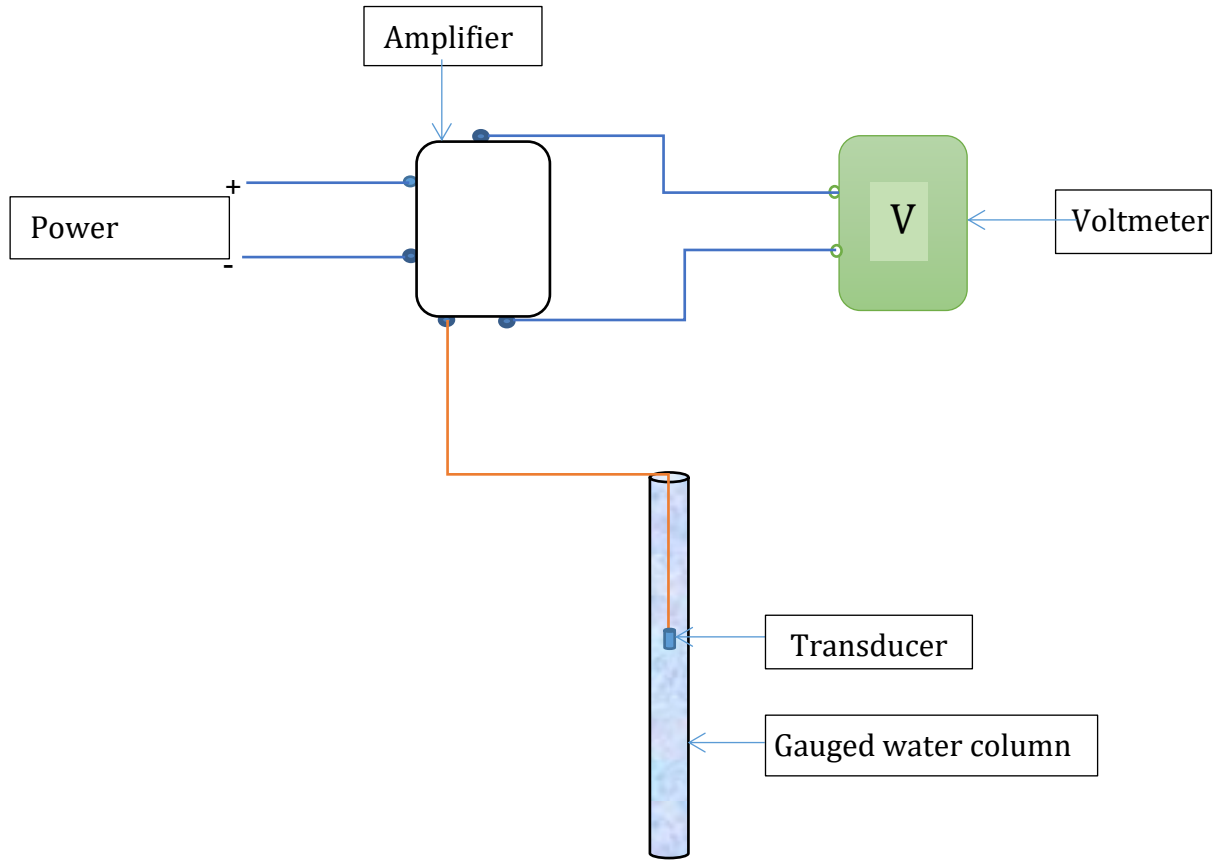

Figure F.0.1 : Schematic diagram of the calibration set-up of the pressure sensor

The range for the voltmeter readings are +10Vdc to -10Vdc.

The calibration is done using a system consisting of a transducer, electronics, and cables. When the set-up is arranged as in Figure F.0.1 above and once calibrated, it provides a DC signal that will be proportional to the respective pressure difference as illustrated by equation (F.1) below.

$$[P] = gain * [V] + offset \qquad \text{(F.1)}$$

Each pressure sensor is calibrated separately. The calibration graphs obtained for the three pressure sensors (P1, P2 and P3) are depicted below.

The respective gain and offset for each pressure sensor is found in the calibration process. Based on the measurements the calibration graphs was obtained for each pressure sensor in Figure F.2, Figure F.3 and Figure F.4.

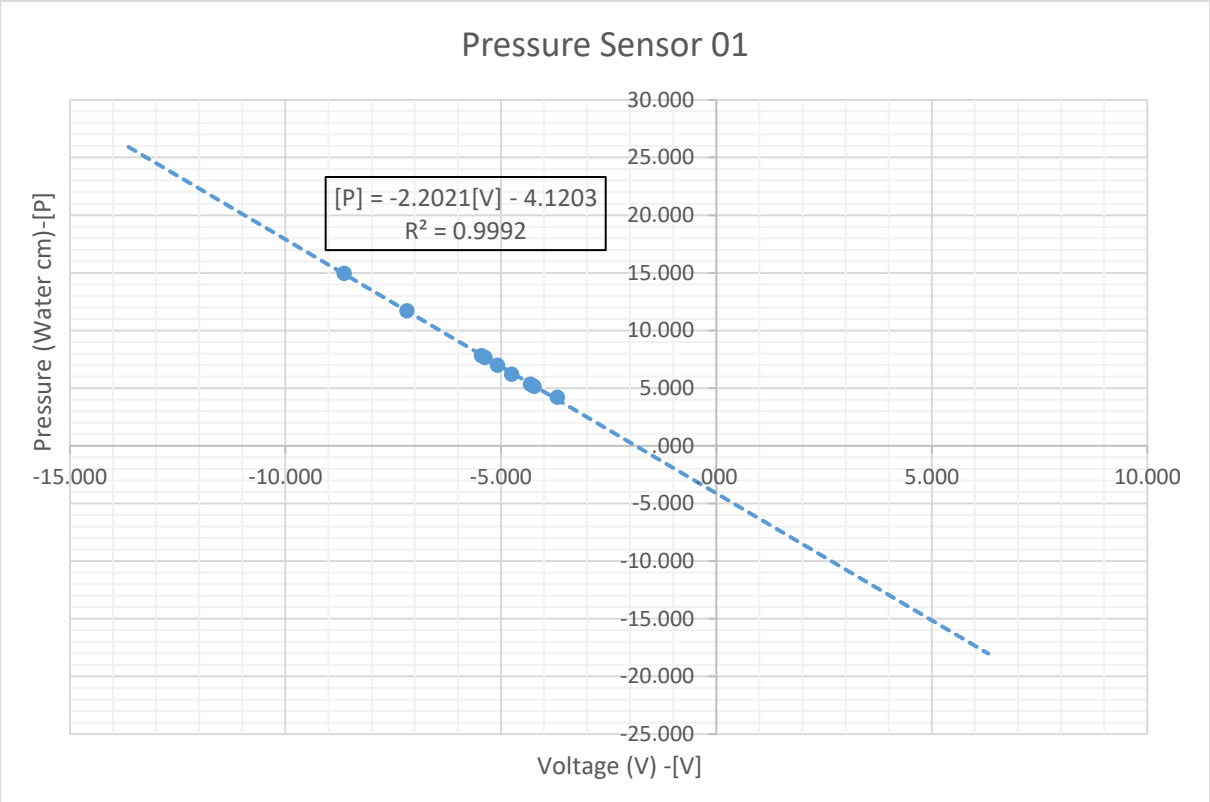

Figure F.2 : Calibration graph for pressure sensor 01 (P1)

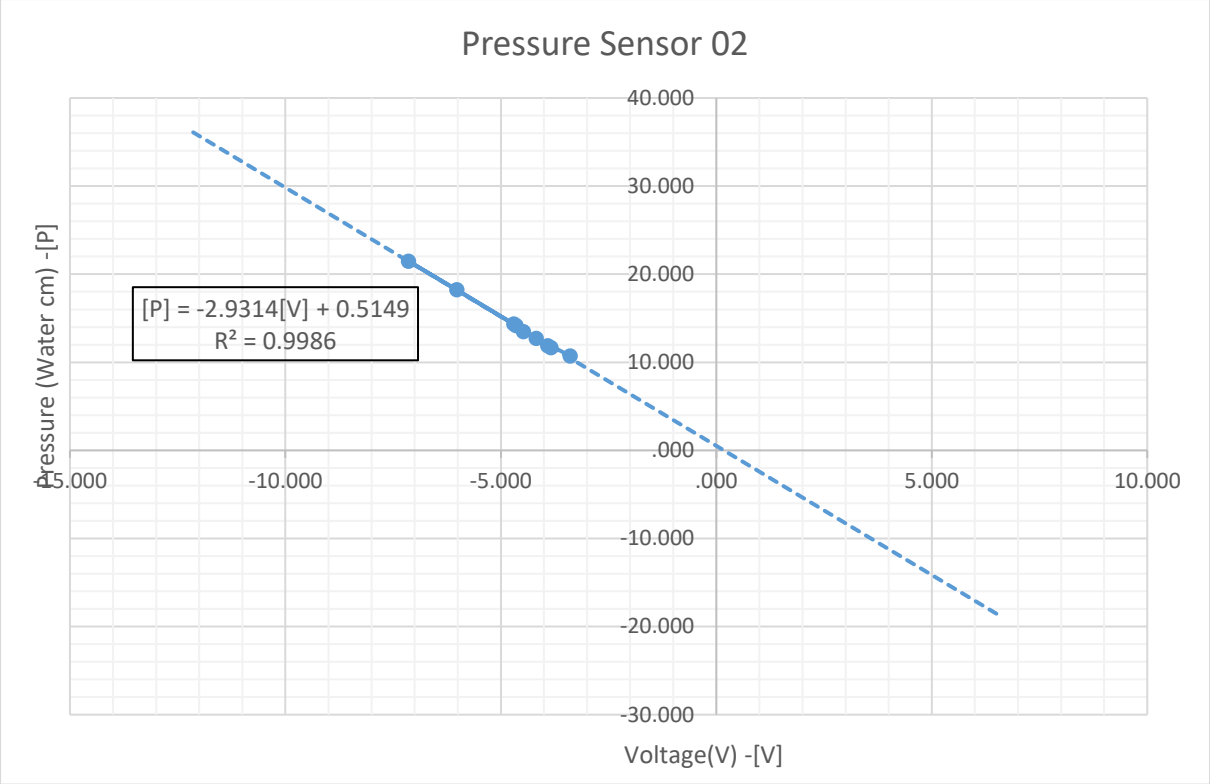

Figure F.3 : Calibration graph for pressure sensor 02 (P2)

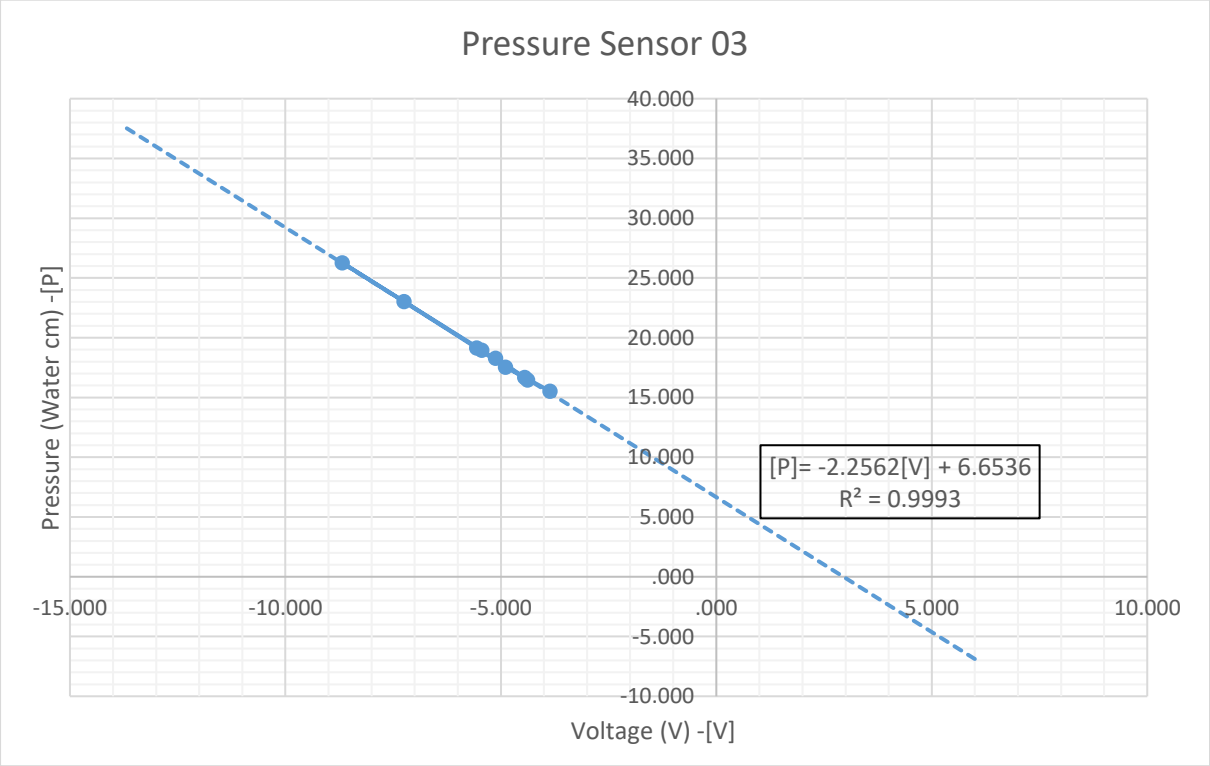

Figure F.4 : Calibration graph for pressure sensor 03 (P3)

Based on this calibration graph, the corresponding pressure related to measured electrical signal is calculated for each pressure sensor.

G Non-hydrostatic calculation of ΔP

An estimate for ΔP using a non-hydrostatic method is discussed below.

Consider a water particle moving from P to Q as depicted in Figure G.1.

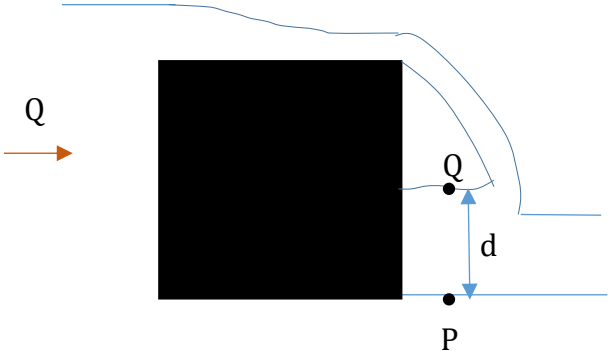

Figure G.1 : Movement of water particle from P to Q

Along z direction, applying Navier-Stokes equation for the momentum balance,

$$\frac{\partial w}{\partial t} + u\frac{\partial w}{\partial x} + v\frac{\partial w}{\partial y} + w\frac{\partial w}{\partial z} = \frac{-1}{\rho}\frac{\partial P}{\partial z} - g \qquad \text{(G.1)}$$

Neglecting the non-vertical advective terms yields,

$$\rho w\frac{dw}{dz} - \rho g = \frac{dP}{dz} \qquad \text{(G.2)}$$

where w= vertical velocity

$$P = \int \left\{\rho w\frac{dw}{dt} - \rho g\right\} dz \qquad \text{(G.3)}$$

At free water surface (Q) and bottom (P), the vertical velocity (w) equals to zero. As a basic hypothesis, the vertical velocity(w) can be assumed to follow a parabolic function as illustrated in Figure G.2.

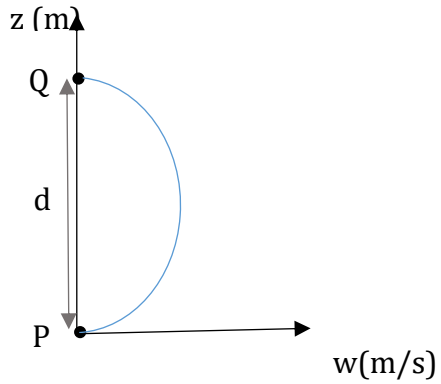

Figure G.2 : Vertical velocity (w) variation along vertical direction from point P to point Q

Thus, a general solution for 'w' can be written as,

$$w = a_0 z^2 + b_0 z + c_0 \tag{G.4}$$

Where a_0, b_0 and c_0 are constants that need to be determined.

By substitution of 'w' value at top and bottom points,

$$w = a_0 z^2 + (a_0 d)$$

$$w\frac{dw}{dt} = ({a_0}^2)z^3 + (2{a_0}^2 d)z^2 + ({a_0}^2 d^2)z \tag{G.5}$$

By equations (G.3) and (G.5),

$$P = \rho\left\{\frac{a_0 z^4}{4} + \frac{2{a_0}^2 d' z^3}{3} + \frac{{a_0}^2 d'^2 z^2}{2} - gz\right\} \tag{G.6}$$

The value of constant 'a_0' can be found using the 'least square curve fitting' method as there are two known measurements and one unknown in equation (G.6). (i.e time average of P2 and P3 are known for respective z values, so that the only unknown is the constant 'a_0').

From the 'least square curve fitting' method, the coefficients of z^4, z^3 and z^2 in equation G.6 are found to be zero.

This indeed proves the recirculation process and dynamics behind the nappe is not non-hydrostatic but governed by hydrostatic conditions.

Therefore, no further analysis is carried out on this.

H Determination of the air entrainment rate

Considering Test_10, a linear variation of pressure reduction experienced by bottom pressure sensor (P3) occurs between 265s and 365s. (See Figure H.1)

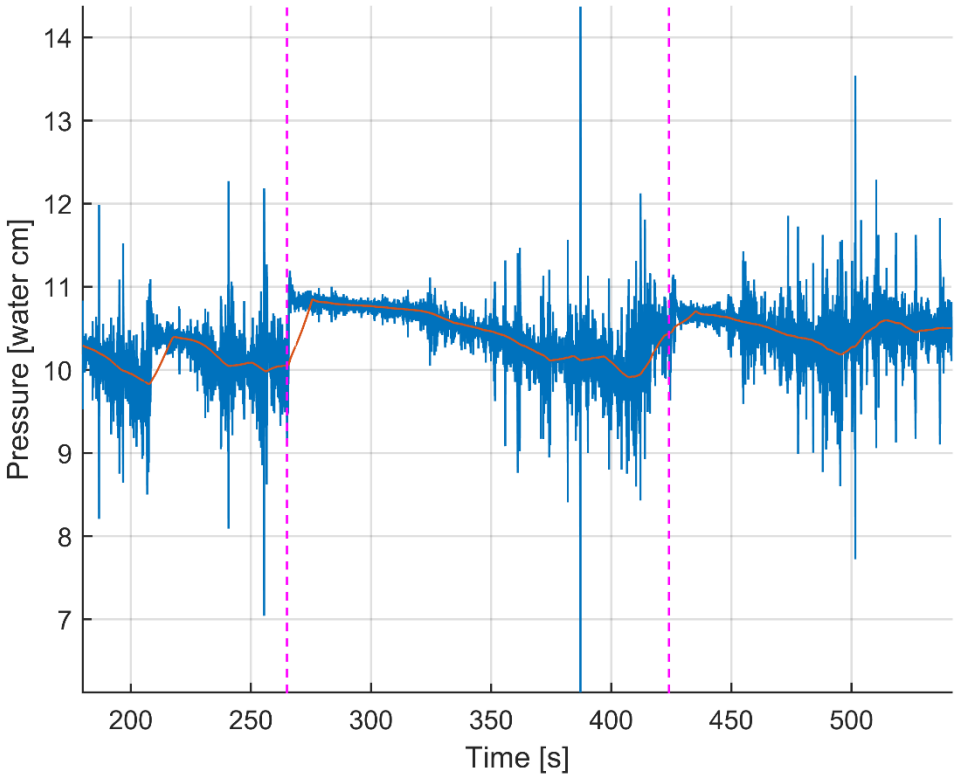

Figure H.0.1 : Pressure time series of the bottom pressure sensor (P3). The red dotted vertical lines depict the two aerated points. The orange line is the moving average using 10s time period

The nappe trajectories for both the aerated and non-aerated cases as well as the water level rise due to the pressure drop can be used to find the water volume/unit area that is occupied due to air entrainment. (See Figure H.2)

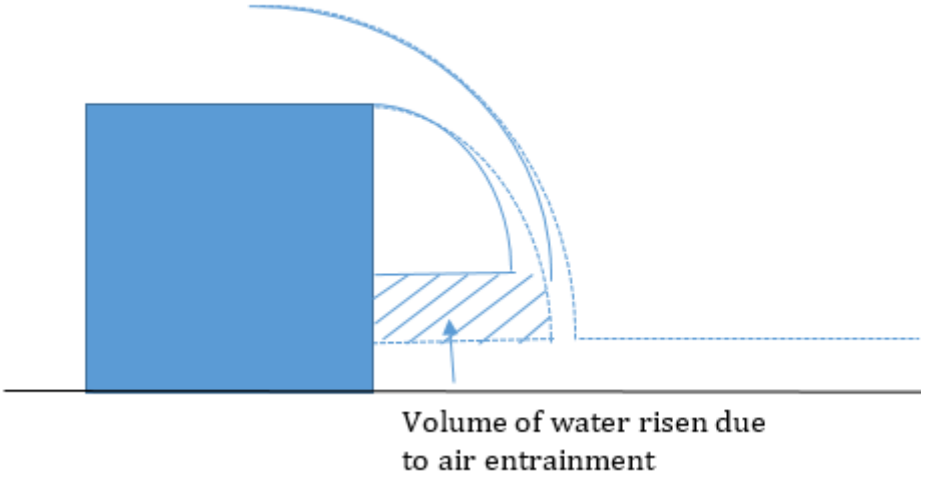

Figure H.2 : Volume of water risen due to air entrainment

It can be assumed that the volume of water risen equals to the air volume lost in the cavity below the nappe(assuming air is entrained only from the cavity). Therefore,

Volume of air lost/unit length=0.00106875m^3/m

Rate of air entrainment = $1.06875E-05\ m^3/m/sec$

I Input structure of InterFoam

The *weirOverFlow* application in the InterFoam solver is used in this study as it represents the most closely resembling situation to the scenario in concern. The input structure of InterFoam consists of three main directories as depicted in Figure I.1 in which the parameters, initial conditions and boundary conditions are assigned accordingly.

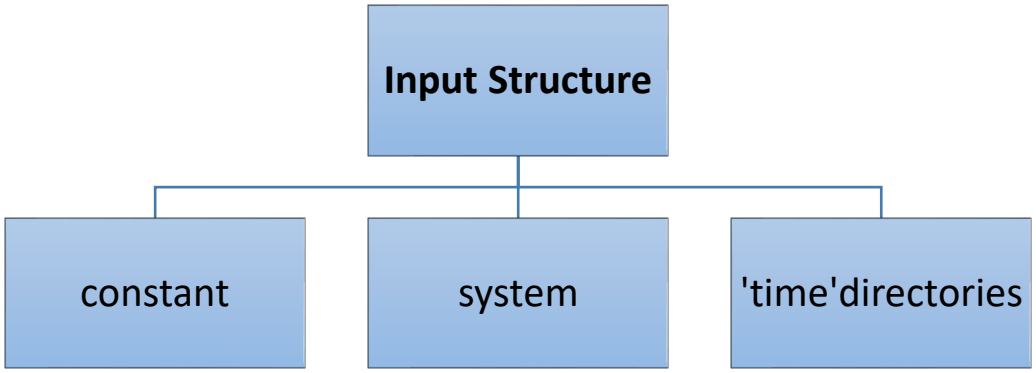

Figure I.1 : Input structure of InterFoam

These three directories are then sub-divided into number of files accordingly. Some of the important files are explained in sections below together with the input values.

I.1 Constant directory

In this directory, the transport properties (including physical properties) as well as turbulence properties are assigned. Both water and air are considered as Newtonian fluids with kinematic viscosities of 1e-06 and 1.48e-05 respectively. Further, a surface tension value of 0.07 is set.

Under turbulence properties, initially the simulation is carried out using the 'laminar' case applying a coarser grid spacing. Next, the RAS k-ε turbulence model is used with the emphasis on the associated turbulence phenomenon evident in the breakwater overflowing.

I.2 System directory

The 'system' directory includes the parameters associated with the solution procedure (Greenshields, 2016). In *blockMeshDisct* file, the dimensions and the physical boundaries of the domain are specified.

The front and back faces of the domain are specified as empty.

In *ControlDict* file, the time related parameters are set. The simulation is carried out for a time period that is similar to the laboratory experiment and the delta T (initial time step used for solving the equations) is set to be 0.05 seconds. Further, a maximum Courant number of 0.02 was set. The Courant number (Co) is defined as shown in equation (G.1).

$$Co = \frac{U\Delta t}{\Delta x} \tag{I.1}$$

Where, U =velocity (m/s)

Δt =time step for each calculation(s)

Δx =grid spacing (m)

The Courant number is typically calculated for each cell during the model simulation. Physically, the Courant number acts as an indicator of how the fluid is moving through the computational mesh. If C_0<=1, a fluid particle moves only from one cell to the other in a single time step. If C_0 >1, the fluid particles may move several cells during a single time step.

As the model in this study uses a static mesh, to satisfy the Courant number criteria, the option of automatic adjustment of the time step is turned on.

I.3 'Time' directories

This consists of individual files of data for each of the fields including alpha.water(α), pressure(p_rgh), velocity(U), kinetic energy(k), dissipation rate(epsilon) and kinematic viscosity(nut). The initial conditions as well as the boundary types are defined for each physical boundary (eg : For inlet, outlet, lowerWall etc) in each field. The key initial conditions and boundary conditions that are used in the simulation are briefly explained in the next section.

Initial conditions used for the simulations

In order to simulate the laboratory experiment properly, the boundary conditions are required to be assigned in proper manner similar to the experimental conditions. For the InterFoam simulation, the boundary conditions are set to reproduce the exact experimental scenario of the test conducted in the laboratory flume in Water Lab.

Inflow rate

A constant inflow rate is set as an initial condition from time=0 till the end of the simulation run. The value of the inflow rate is 2.5 litre/s since it is the steady flow rate for Test_10. Based on the set inflow rate, it is observed that the time required to achieve the steady state is 30s. (The water levels on both the upstream and downstream remain at the same position after the steady state is reached).

Outflow rate

At the actual physical model a free outflow is set and a similar free outflow condition is simulated in the OpenFOAM simulation by modelling downstream weir.

J Analysis of pressure results and calculation for ρeffective

In order to analyse the pressure results more effectively, the pressure time series only after the steady flow is taken into account.

For an instance, the pressure time series of P2 (mid pressure sensor) and P3 (bottom pressure sensor) for Test_7 (Q=5.78 litre/s and tail water depth=2.87 cm) is shown in Figure J.1.

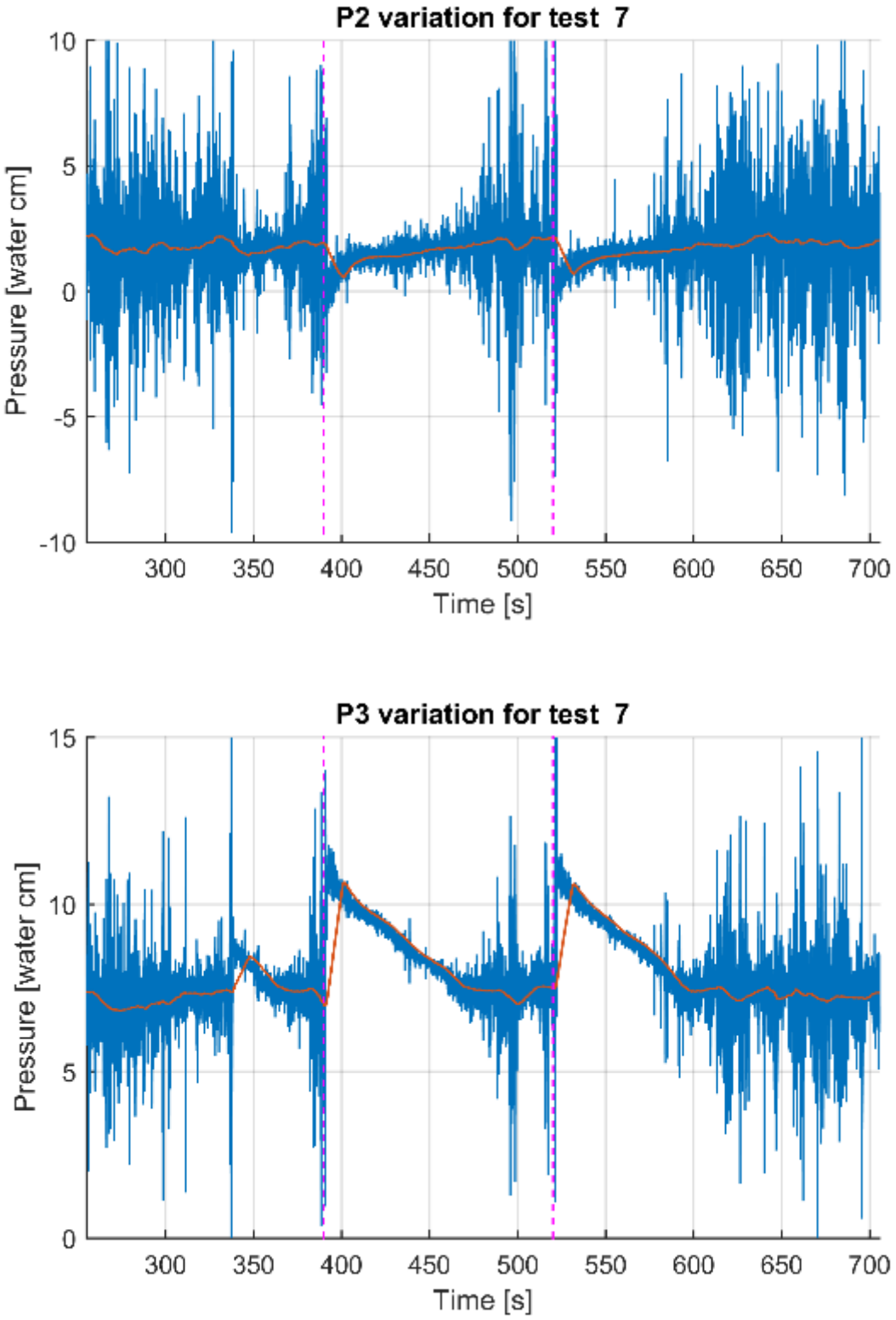

Figure J.1 : Pressure time series for Test_7 for mid(P2) and bottom(P3) pressure sensors

The two vertical red dotted lines represent the two aeration points (At t=390s and t=520s) during the experiment. The orange-coloured line indicate the moving average using a 10-seconds period in each case of P2(mid) and P3(bottom).

The pressure observations can be interpreted based on the effective density as follows.

As it is evident from Figure J.1, the pressure in P2 (mid) drops by an approximate amount of 150Pa as a result of aeration. In contrast to that, a drastic increase of P3 closer to 400Pa is evident when the aeration is applied. This can be explained by the fact that with aeration, the pressure below nappe becomes atmospheric due to the aeration process. This leads to an increase of pressure from the sub-atmospheric pressure that was prevailing under the nappe before aeration. This sudden increase of pressure results in a drastic upward movement of pressure experienced by the bottom pressure sensor (P3). A similar behaviour of P2 and P3 can be seen in all the experimental runs conducted.

These contradictory variations of P2 and P3 can be explained by the reduction of density of water due to the presence of high percentage of air bubbles. From experiment, it was observed that high amount of air bubbles are recirculating under the nappe during the non-aerated case. Using the pressure data obtained, the effective density value (ρ_{eff}) is found to be 988 kgm^{-3} for the non-aerated nappe scenario. This ρ_{eff} value of 988 kgm^{-3} is used for the non-aerated case in further analyses.

The determination of ρ_{eff} is explained below. (For Test_10, the pressure readings for mid pressure sensor is erroneous due to the exposure to air. Thus, based on the similar air bubble movement in Test_10 and Test _7, Test_7 is used to find the ρ_{eff} as a reasonable approximation).

It is observed during non-aeration nappe, a large number of air bubbles are recirculating within the recirculation region. Therefore, it suggests that the time-averaged density of water within the recirculation region is less than 1000 kg/m^3. It can be introduced as an effective density of water (ρ_{eff}), which takes the presence of air bubbles within water into account. This can be checked by considering the time-averaged pressures from mid (P2) and bottom (P3) pressure sensors.

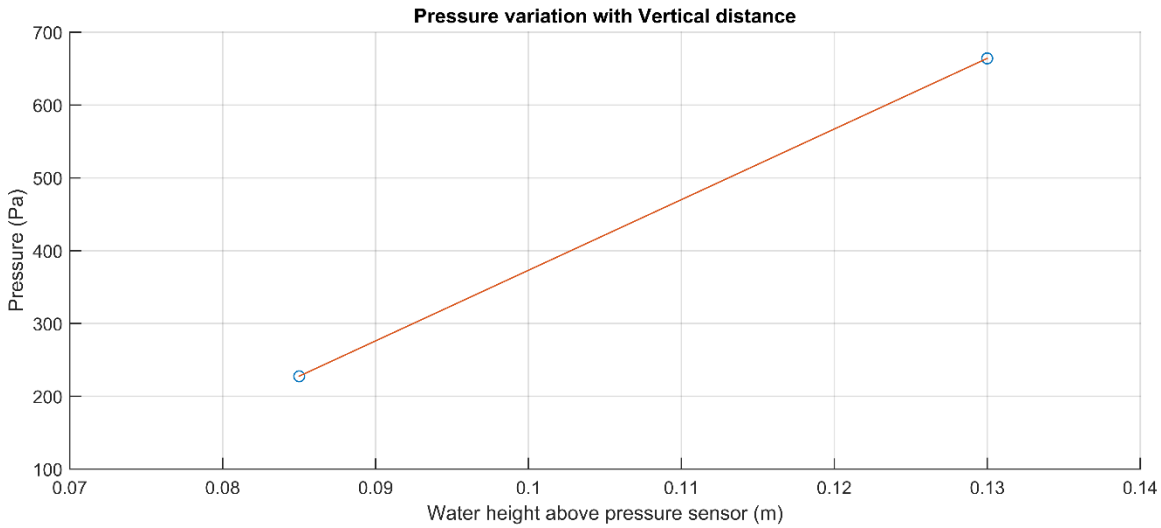

Figure J.2 : Pressure variation with vertical distance(Time averaged pressure for non-aerated nappe is considered. The lower point corresponds to P2 and the upper one to P3)

The time-averaged values for the non-aerated nappe that are used in the above analysis is depicted in Figure J.2.

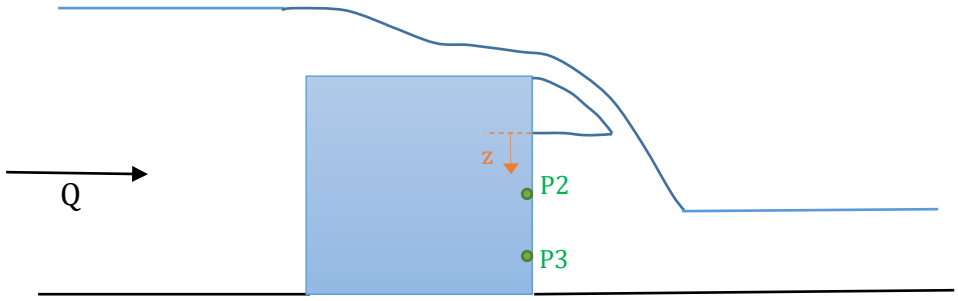

Figure J.3 : Time-averaged values used to plot graph in Figure J.1 (For non-aerated nappe case)

From Figure J.3,

$$P_3 - P_2 = (\Delta z)\rho_{eff} g \tag{J.1}$$

$$\rho_{eff} = \frac{P_3 - P_2}{(\Delta z) g} \tag{J.2}$$

$$\rho_{eff} = 988\ kgm^{-3}$$

For Test_10, ΔP calculations are based on ρ_{eff} value of 988 kgm^{-3}.